

AD A 036653

RADC-TR-76-330  
Interim Report  
January 1977

12

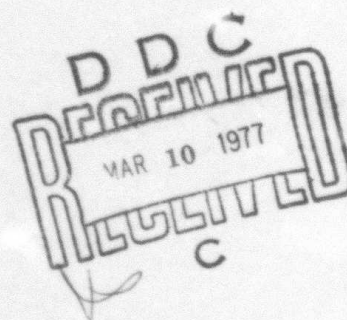


# LASER ATMOSPHERIC ABSORPTION STUDIES

The Ohio State University

Sponsored by  
Defense Advanced Research Projects Agency (DoD)  
ARPA Order No. 1279

Approved for public release;  
distribution unlimited.

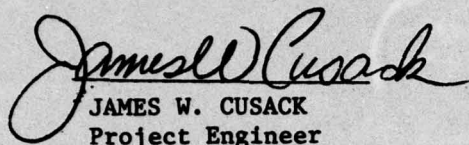


The views and conclusions contained in this document are those of the authors and should not be interpreted as necessarily representing the official policies, either expressed or implied, of the Defense Advanced Research Projects Agency or the U. S. Government.

**ROME AIR DEVELOPMENT CENTER  
AIR FORCE SYSTEMS COMMAND  
GRIFFISS AIR FORCE BASE, NEW YORK 13441**

This report has been reviewed by the RADC Information Office (OI) and is releasable to the National Technical Information Service (NTIS). At NTIS it will be releasable to the general public including foreign nations.

This report has been reviewed and is approved for publication.

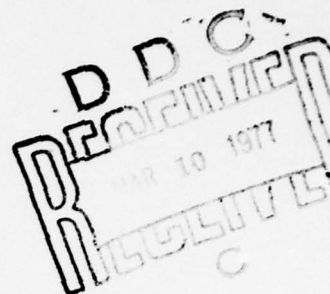
  
JAMES W. CUSACK  
Project Engineer

Do not return this copy. Retain or destroy.



LASER ATMOSPHERIC ABSORPTION STUDIES

R. K. Long  
E. K. Damon  
J. C. Peterson  
M. E. Thomas



Contractor: The Ohio State University  
Contract Number: F30602-76-C-0058  
Effective Date of Contract: 1 July 1975  
Contract Expiration Date: 3 September 1977  
Short Title of Work: Laser Atmospheric  
Absorption Studies  
Program Code Number: 5E20  
Period of Work Covered: Jul 75 - Jan 76

Principal Investigator: Dr. R. K. Long  
Phone: 614 422-6077  
Project Engineer: James W. Cusack  
Phone: 315 330-3145

Approved for public release;  
distribution unlimited.

This research was supported by the Defense Advanced Research Projects Agency of the Department of Defense and was monitored by James W. Cusack (OCSE), Griffiss AFB NY 13441 under Contract F30602-76-C-0058.

UNCLASSIFIED

SECURITY CLASSIFICATION OF THIS PAGE (When Data Entered)

REPORT DOCUMENTATION PAGE		READ INSTRUCTIONS BEFORE COMPLETING FORM
1. REPORT NUMBER RADC-TR-76-330	2. GOVT ACCESSION NO.	3. RECIPIENT'S CATALOG NUMBER
4. TITLE (and Subtitle) LASER ATMOSPHERIC ABSORPTION STUDIES	5. TYPE OF REPORT & PERIOD COVERED Interim Report 1 Jul 75 - 31 Jan 76	6. PERFORMING ORG. REPORT NUMBER ESL-4232-1
7. AUTHOR(s) R. K. Long, J. C. Peterson E. K. Damon, M. E. Thomas	8. CONTRACT OR GRANT NUMBER(s) F30602-76-C-0058	9. PROGRAM ELEMENT, PROJECT, TASK AREA & WORK UNIT NUMBERS 62301E 12790508
10. PERFORMING ORGANIZATION NAME AND ADDRESS The Ohio State University/ElectroScience Laboratory Dept of Electrical Engineering Columbus OH 43212	11. CONTROLLING OFFICE NAME AND ADDRESS Defense Advanced Research Projects Agency 1400 Wilson Blvd Arlington VA 22209	12. REPORT DATE January 1977
13. MONITORING AGENCY NAME & ADDRESS (if different from Controlling Office) Rome Air Development Center (OCSE) Griffiss AFB NY 13441	14. NUMBER OF PAGES 159	15. SECURITY CLASS. (of this report) UNCLASSIFIED
16. DISTRIBUTION STATEMENT (of this Report) Approved for public release; distribution unlimited.		15a. DECLASSIFICATION/DOWNGRADING SCHEDULE N/A
17. DISTRIBUTION STATEMENT (of the abstract entered in Block 20, if different from Report) Same		
18. SUPPLEMENTARY NOTES RADC Project Engineer: James W. Cusack (OCSE)		
19. KEY WORDS (Continue on reverse side if necessary and identify by block number) Molecular Absorption CO <sub>2</sub> N <sub>2</sub> O Laser Spectrophone H <sub>2</sub> O Laser Diode White Cell Laser Propagation Long-path Cell CO <sub>2</sub> Laser Multi-pass Cell		
20. ABSTRACT (Continue on reverse side if necessary and identify by block number) This report describes progress on the various tasks which comprise the research program. The three major components are Part B: Initial Design Studies For a Cooled Long-Path Absorption Cell, Part C: A Differential Spectrophone of Unique Design, and Part D: Tunable Semiconductor Laser Spectroscopy of CO <sub>2</sub> , N <sub>2</sub> O, and H <sub>2</sub> O in the 5-Micron Region.		

DD FORM 1 JAN 73 1473

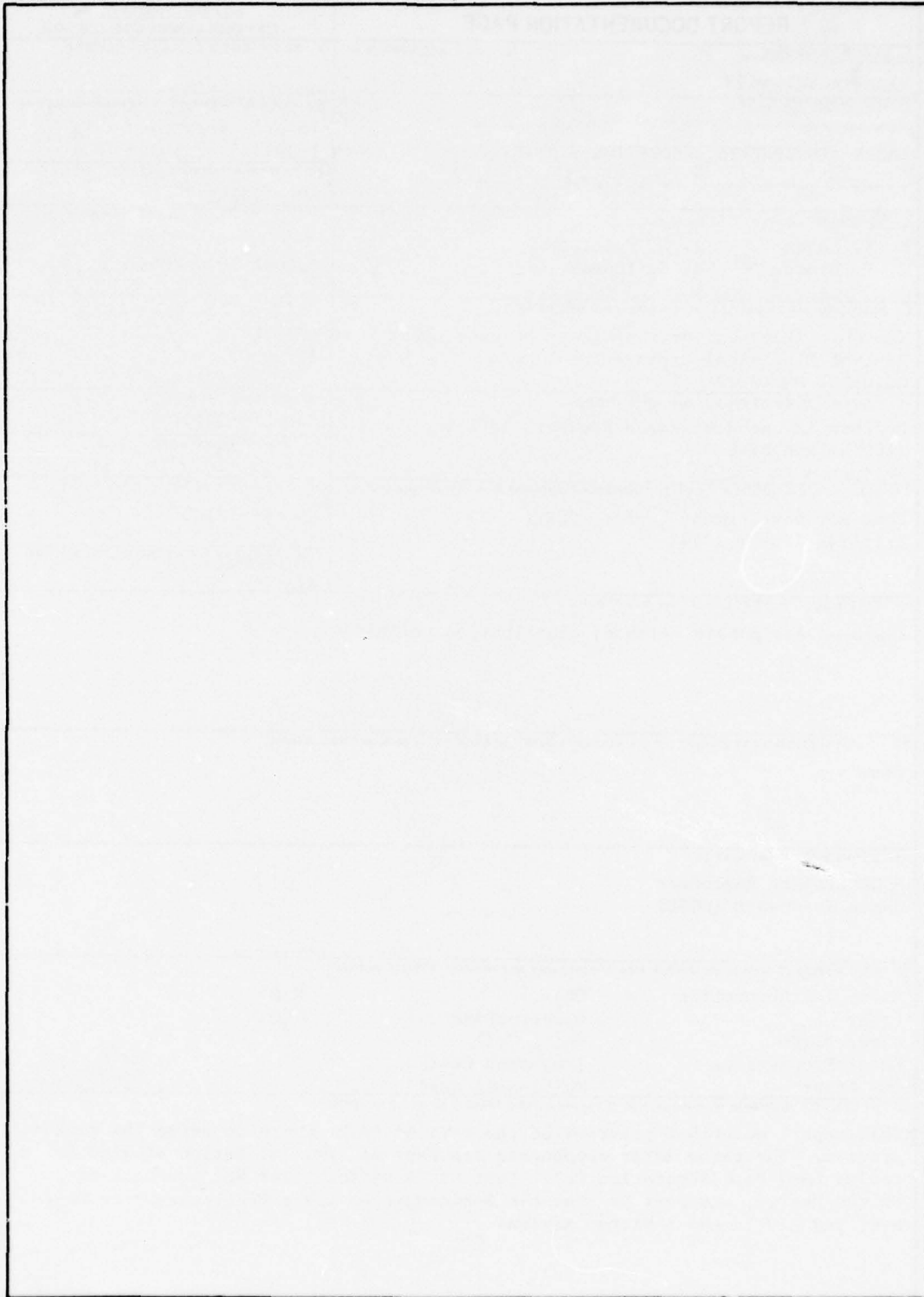
EDITION OF 1 NOV 65 IS OBSOLETE

UNCLASSIFIED

SECURITY CLASSIFICATION OF THIS PAGE (When Data Entered)

UNCLASSIFIED

SECURITY CLASSIFICATION OF THIS PAGE(When Data Entered)



UNCLASSIFIED

SECURITY CLASSIFICATION OF THIS PAGE(When Data Entered)



## PREFACE

This report, Ohio State University Research Foundation Report Number 4232-1 (First Interim Report), was prepared by The Ohio State University ElectroScience Laboratory, Department of Electrical Engineering at Columbus, Ohio. Research was conducted under Contract F30602-76-C-0058. Mr. James W. Cusack, RADC(OCSE), of Rome Air Development Center, Griffiss Air Force Base, New York, is the Project Engineer.

## TABLE OF CONTENTS

Part A: Introduction . . . . .	A-1
Part B: Initial Design Studies For a Cooled Long-Path Absorption Cell by E.K. Damon . . . . .	B-i
Part C: Tunable Semiconductor Laser Spectroscopy of CO <sub>2</sub> N <sub>2</sub> O, and H <sub>2</sub> O in the 5-Micron Region by Michael E. Thomas . . . . .	C-i
Part D: A Differential Spectrophone of Unique Design by John C. Peterson . . . . .	D-i

PART A  
INTRODUCTION

This is the first semi-annual report on Contract F30602-76-C-0058.

Three of the major activities are reported in detail in Parts B, C, and D.

Several other efforts are underway which are briefly mentioned below and will be reported fully in the second semi-annual report.

They are:

1. Further studies of water vapor absorption at 10.6  $\mu\text{m}$  using the differential spectrophone.
2. Design and construction of a second model of the differential spectrophone employing stainless steel high vacuum techniques, ZnSe windows, and temperature control capability.
3. Design of a resonant-type spectrophone.
4. Construction of a cw DF laser of the United Technology Corporation type.
5. Construction of a cw CO laser with output on 10-vibrational bands.
6. White cell water vapor absorption studies with the above CO laser.
7. Modification of a commercial CO<sub>2</sub> laser for single line operation and design of an improved "home-made" frequency stabilized CO<sub>2</sub> laser.
8. White cell water vapor absorption studies with the above CO<sub>2</sub> lasers.
9. Ozone spectroscopy of 2  $\nu_3$  band including the design of a special 2 meter per pass stainless steel White cell with 77°K cooling capability.
10. Refurbishment of a DoD surplus computer system, SEL Model 810B, for use in laser transmittance data acquisition and Fourier Transform Spectroscopy.
11. Continued development of computer programs using the AFCRL data tape.

Preliminary results on a number of these efforts have been given in the monthly management reports.



PART B

INITIAL DESIGN STUDIES FOR A COOLED-LONG PATH  
ABSORPTION CELL

Contents

	Page
INTRODUCTION	B-1
THE VACUUM CHAMBER	B-1
OPTICAL SYSTEM	B-6
ACCESSORY CONSIDERATIONS	B-12
CURRENT STATUS	B-13
REFERENCES	B-17

## INTRODUCTION

The multi-pass absorption cell has been, for some years, a basic tool for the study of optical transmission in gases. It has been used by molecular spectroscopists, where the absorption of the gases of interest is frequently relatively high, as well as for atmospheric transmittance studies. Studies of atmospheric transmittance for high energy lasers is a particularly difficult regime since very low absorption coefficients are of concern, with a consequent requirement for very long path lengths.

This report will document the initial design philosophy of a multi-pass absorption cell of the White cell type which is now under construction at this laboratory. It is meant to supplement a long path White cell that has been in continuous use for laser measurements for the past fifteen years, but which is inadequate for many of the measurements essential to current needs. The necessary design changes are both mechanical and optical. Some are required for new requirements such as wide temperature capability; some are the result of inadequacies in previous design techniques.

The basic requirements of the absorption cell are: that it be of stainless steel, for low contamination and for work with gases such as ozone; that it be capable of temperatures from 20°C to -58°C (temperatures to 60°C desirable); have a temperature uniformity of  $\pm 0.2^\circ\text{C}$  along its length, to minimize turbulence effects; that it be capable of at least a one km path length.

From experience with our present cell, the design concept must allow ready adaptability and upgrading for future programs, offer high mechanical stability and minimize vibration problems, and be capable of rapid, accurate adjustment of the main optical system.

The major components will be treated in three sections: the vacuum chamber and its supports, the main optical system and its controls, and the accessories including windows, gas handling, vacuum, and refrigeration systems.

A plan view of the overall system is shown in Fig. 1. Mirror spacing is to be 10.785 meters (35.4 feet), and the main optical system is composed of three identical spherical mirrors of 10 inch diameter. A pair of these are side by side, setting the vacuum chamber diameter at 24 inches.

## THE VACUUM CHAMBER

The vacuum chamber for the absorption cell is 40 feet long and 24 inches in diameter (OD). To reduce contamination problems and to

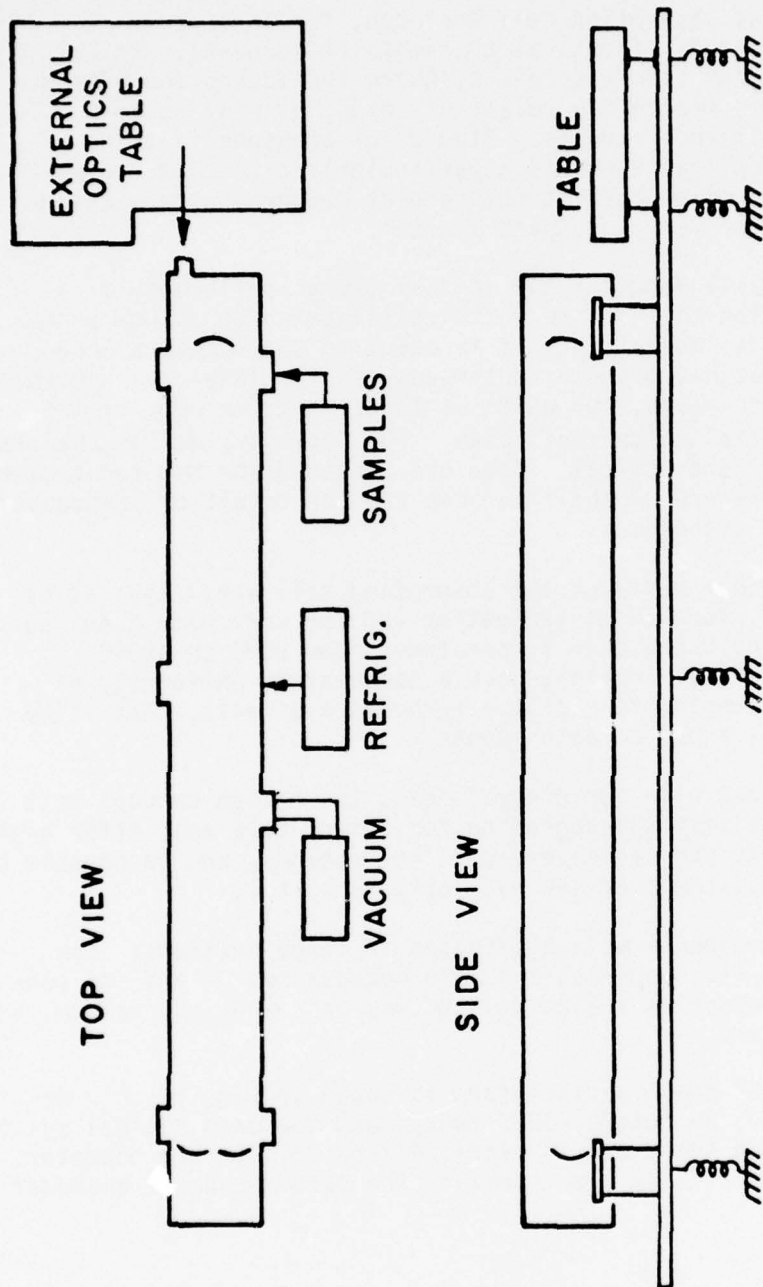


Fig. 1. General System Concept.



allow the use of such gases as ozone, it is fabricated from welded rolled sheets of 304 stainless steel with a good (2B) interior finish. Contamination of an atmospheric sample by a residual previous sample has been a problem in previous experiments, and considerable care has therefore been taken to minimize the virtual leaks, or internal gas pockets, in this design. Minimal wall thickness for crush strength under vacuum conditions is 3/16 inch; 1/4 inch was selected to provide a safety factor. Other similar facilities have been successful. Cell mass is approximately 2600 pounds for this vacuum chamber; the completed system chamber and optics can be expected to be about twice this.

The constraints in mounting the vacuum chamber include thermal effects. Cooling the cell to  $-60^{\circ}\text{C}$  will result in a length change of -0.52 inches between the mirrors, and a diameter change of 0.03 inches. At  $100^{\circ}\text{C}$ , one would have a similar expansion. The length change would seriously defocus the optics if they were attached to the cell. This problem can be countered by utilizing a bellows in the vacuum chamber or by translating the optics. In the design to be adopted, the bellows would be difficult to cool uniformly, and furthermore would produce a 7200 pound longitudinal force upon chamber evacuation which would necessitate a very stiff mechanical mount. The diameter change, although not large, would result in difficulties in mechanically mounting the optics, and some lateral displacements would appear inevitable.

The decision was therefore made to mount the optics from a stable external platform and allow the vacuum chamber to be mechanically decoupled. Implementation of this is shown in Fig. 2. The plate upon which the optics are to be mounted is supported by three legs, each 1.75 inch diameter. A 3 inch ID bellows (Pathway 0301A) connects the legs to the vacuum chamber. The bellows is quite flexible, and horizontal forces on the legs due to chamber expansion should be less than 10 pounds. Chamber evacuation will create a 130 pound longitudinal force which will not cause any problems if suitable mechanical constraint is used, and if the chamber and legs have a common mounting platform. This will be considered later.

The chamber ends are flanged, and will be O-ring sealed to end caps which will contain the main optical ports. These, and all other O-rings, will be of Teflon with internal spring loading to maintain sealing pressures over the operating temperature range.

Six ports of eight inch diameter are available, as indicated in Fig. 1. Four of these allow access near the main optics for assembly and adjustment procedures, but will also be used for sample handling and instrumentation feedthroughs as required. The other two are near the center of the chamber and are to be used as vacuum ports and access. Those near the optics offer a 24 inch cross-chamber path, those near the center a diagonal 48 inch path for optical monitoring purposes. For

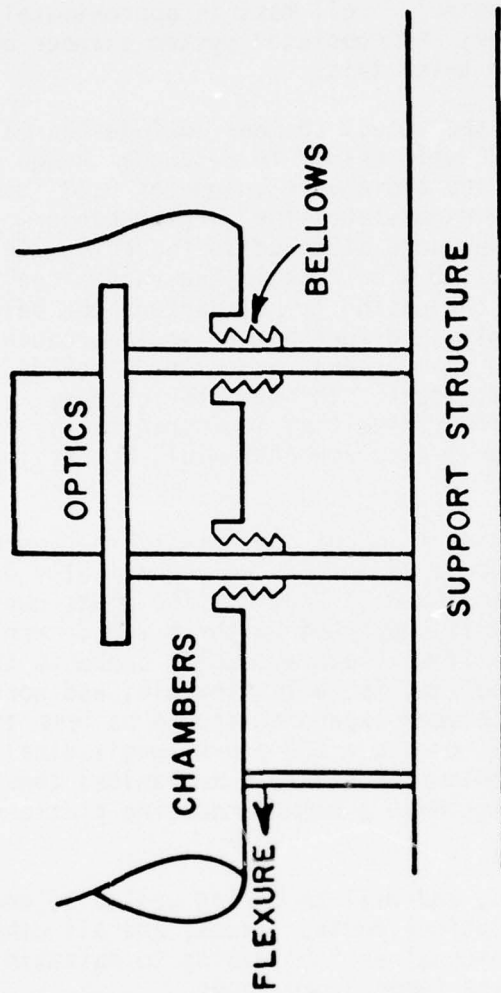


Fig. 2. Decoupling Optics from Chamber.

mounting monitoring apparatus or light baffles, there are also ten internal brackets available. The primary feedthroughs for electrical connections or coolant are six "ultra-torr" couplings for 1/2 inch tubing near each end of the chamber. The tubing will serve as conduit for the wiring, eliminating contamination problems from connections to the internal motors.

Thermal control of the chamber is accomplished by circulating liquid through a manifold welded to the outside chamber wall. There are eight sections to the manifold, each consisting of four 1/2 inch copper tubes 20 feet long. The division is in half lengthwise, so that coolant enters near the center of the chamber and leaves near each end. Each half is then manifolded in quadrants to get even distribution. The circulating coolant will heat exchange against a two-stage cascaded refrigeration system with fine temperature control achieved by electrical heaters in the lines. A separate coolant circuit will cool the chamber ends, supports, and other loads.

The major heat load will be the ambient surroundings, although care will be needed in thermally baffling the diffusion pump. The surface area of the chamber is approximately 260 square feet. A 5 inch polyurethane foam covering will have a thermal loss of approximately 5.4 BTU/square foot at the lowest operating temperature, or 1400 BTU/hour total, while 6 inch glass wool would be close to 2000 BTU/hour. There will be additional losses through the supports and optical ports, although these should be small. For purposes of these calculations, 1600 BTU/hour will be assumed, or 50 BTU/hour for each 20 foot copper tube. This is the steady-state, not cool-down value. Initial cool-down may require some 60,000 BTU including the coolant supply.

The coolant tubes, then, will be separated by 4.7 inches and have a thermal load of 2.5 BTU per linear foot. If the heat flow is purely radial, the thermal conductivity of the 1/4 inch stainless chamber is low enough that there would be approximately 0.7°C temperature differential between the coolant tube and the point midway between coolant tubes. This differential is reduced by any circumferential heat flow, and should be brought within limits by the mechanical jacket to be used to prevent damage to the insulation. A metallic wrap around the cell below the insulation would also be very effective.

The circulation system must be considered next. If the coolant rise is limited to 0.2°C through the tube, this will set the required flow rate. Assuming a specific heat for the coolant of 0.5 and a specific gravity of 0.8, we need 1.5 gallons of coolant per BTU of heat load, or 37.5 gallons per hour to each tube. A 20 GPM pump will therefore be required for the system.



The 1/2 inch tubing (0.4 inch ID) carrying 37.5 GPH will have a flow velocity of 1.67 ft/sec. With a viscosity that of water, the Reynolds number is 5100, or the flow is turbulent. The resulting pressure drop in the 20 foot section is 0.4 psi and work done is only 0.4 BTU/hr on each tube. Note however that if 1/4 inch tubing is used, the pressure drop is 13 psi and the work done is 12 BTU/hr, comparable to our cooling load. In particular, we would expect definite temperature problems at the manifold bends. The 1/2 inch tubing should allow a reasonable choice of coolants, perhaps with viscosities up to 10 centipoise. F-11 is one coolant under consideration. The necessary pumping pressure will be set more by the heat exchanger pressure drop and control valves than the chamber tubes, but will be in the range of a simple centrifugal pump.

Refrigeration system requirements are complicated by several factors. Some absorption cells are designed to be always operated at maximum temperature depression, for such studies as chemical kinetics. The system under consideration should be continuously variable. Cycling the refrigeration system would normally produce pronounced stability problems unless an intermediate thermal inertia stage, such as a large coolant tank, was provided. Alternatively, the refrigeration could work against its capacity, with a supplementary electrical heat load, or against its efficiency at lower temperatures. In each case, an intermediate liquid interchange appears desirable. That is, the cell coolant is not cooled directly by the refrigerator evaporator, but by an intermediate liquid cooled by the evaporator. Such a system will also simplify the above ambient cell heating system. The final engineering choice has not yet been made, but will be of the form shown in Fig. 3.

For efficiency and control, the refrigeration system should be sized to run against the operating load. This means that it would approach its final operating temperature exponentially in time. Additional cooling from an auxiliary system should be used for the thermal mass. The economics of liquid nitrogen, dry ice, or a second refrigeration system are being examined. The intermediate heat exchange system proposed will allow such flexibility. The rate of cool down must be limited to avoid large temperature differentials and consequent stresses.

#### OPTICAL SYSTEM

Optical design of a multi-pass absorption cell has shown considerable innovation, and several unique concepts [1-11] have appeared. The basic configuration of J. U. White [1] has been used at this laboratory [13] for 15 years, and elsewhere at this university longer. Two recent improvements make the system more attractive [8,12]. In addition, the environmental requirements and desired stability have prompted many

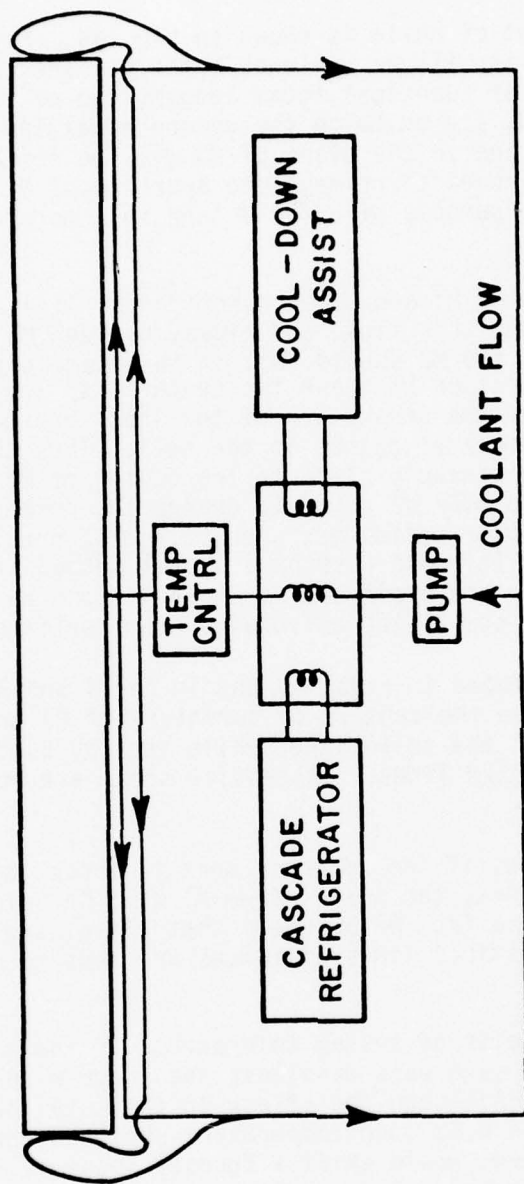


Fig. 3. Temperature Control System.

mechanical design changes which should result in substantial operational improvements. Future adaptability to Fourier transform spectroscopy is also a consideration.

The basic arrangement of White is shown in Fig. 4a. For those unfamiliar with the system, it will be reviewed briefly. The optical train consists of three mirrors of identical focal length, two of them, M1 and M2, adjacent and the third, M3, placed twice the common focal length (the radius of curvature) away. An image in the plane of M3 will be reimaged by M1 or M2 to the same plane; M3 serves to reimage the aperture of M1 onto M2, or vice versa, and serves the purpose of a field lens in a more conventional optical system.

Consider the centers of M1 and M2 on a horizontal line. The center of curvature of M3 should be on this line, and midway between M1 and M2. The centers of curvature of M1 and M2 should fall in this same plane, and somewhere on M3. The separation of these two centers, so long as all reflections fall on M3, and the separation of the input and output coupling determines the number of passes in the cell. Thus the center of M1 can be left fixed, preferably close to the center of M3 for a large number of passes, and only M2 moved to change the number of passes. This is of particular usefulness when path differencing techniques [14] are employed. It could also be a useful method if active stabilization of the optics are employed, as M1 and M3 can be stabilized to fixed positions, and M2 stabilized on total system performance.

Two cases are illustrated in Figs. 4b and 4c for 4 and 8 passes, respectively. C1 and C2 are the centers of curvature of M1 and M2. The central ray is shown as the solid line, while the ray bundle is shown in Fig. 4b by the dashed lines. Successive spots are numbered in 4c.

In the vertical plane, if the entrance port is above the plane containing the mirror centers, the images from M1 will be below that plane and consequently those from M2 be above that plane, and in line with the entrance. Two distinct lines of images are thus formed, which simplifies alignment.

Now consider the effects of system tolerance. If the mirrors are placed 8 cm too far apart, each pass displaces the image plane 8 cm towards the dual mirrors. Although the effect on the total path length may not be significant, the 0.52 inch temperature shrinkage previously discussed, if not controlled, would shift a focused image by 52 inches after 100 passes (1.08 km path). This shift would create problems with the exit optics, particularly if the exit beam were to be focused on a detector. The mirror separation should therefore be adjustable.

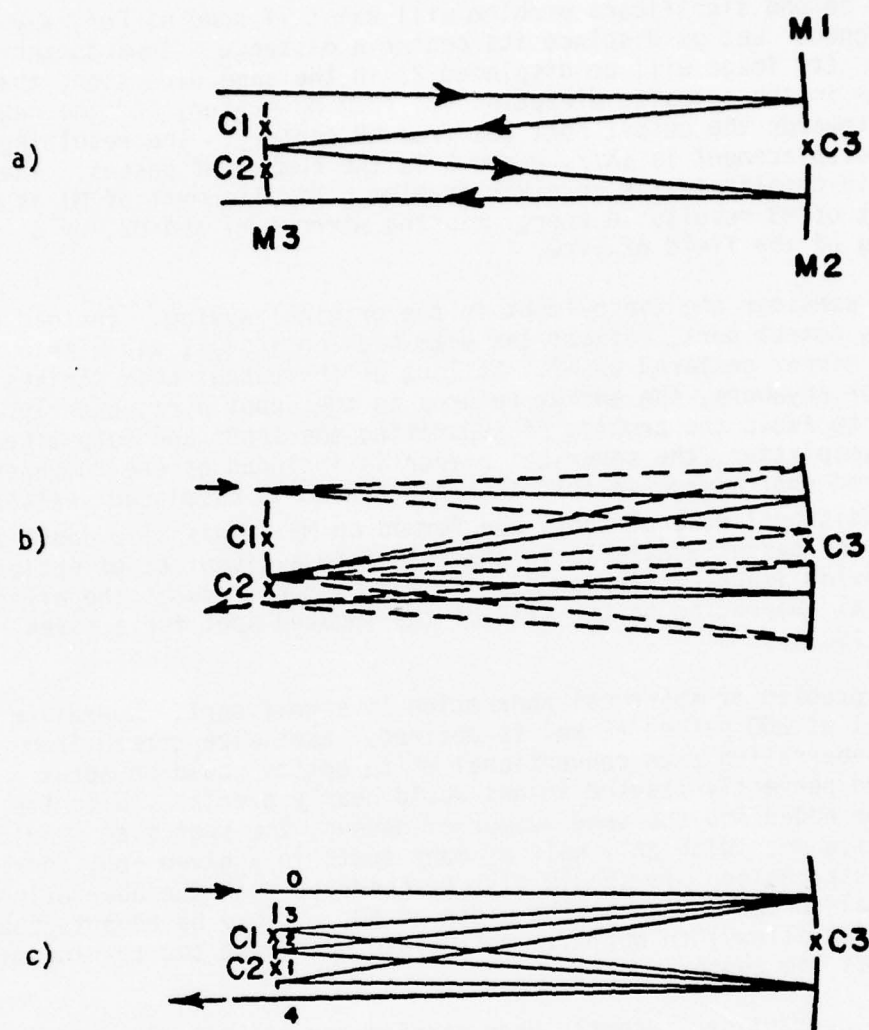


Fig. 4. White Cell Optics.



The second significant problem will exist if some mirror, say M2, is misaligned. Let us displace its center a distance  $\delta$  towards the output port. Its image will be displaced  $2\delta$  in the same direction, that from M1  $2\delta$  in the opposite direction ( $3\delta$  from M2 center) and the next M2 image  $4\delta$  towards the output port ( $3\delta$  from M2 center). The resulting output spot displacement is  $\delta N/2$ , where N is the number of passes. The effect is to again complicate the receiver problem. Misalignment of M1 is similar, that of M3 results in energy missing mirrors M1 and M2, or a vignetting of the field of view.

Now consider one improvement in the original system. Instead of using this output port, reflect the beam back on itself, say with a spherical mirror centered on M2. So long as the output beam strikes this mirror anywhere, the energy returns to the input port, exactly. In practice, to avoid the problem of separating the input and output beams with a beamsplitter, the spherical mirror is included as one component of a decentered roof mirror so that the return beam is displaced vertically and two additional rows of spots are formed on M3. This also doubles the number of passes available in the cell from a given set of optics without having image overlap on M3. It furthermore reduces the effects of spherical aberration on the size of the focused spot for a given number of passes.

The problem of spherical aberration is significant. Operation of the cell at 200 passes (2 km) is desired. Spot size growth from spherical aberration with conventional White optics would be about 3.2 mm, and perfectly focused images would nearly overlap. With the roof mirror added and the same number of passes, the spot size should grow only 1.6 mm. With only half as many spots in a given row, there is very good separation. It should also be observed that the aberration is proportional to the square of the width of M3. It may be advantageous (if stability allows) to optimize this width by moving the turning mirrors towards the center.

This concept has recently been carried one additional step by White where a lateral displacement is produced by an identical (rotated) combination of mirrors. Path length adjustments are now made in steps of 16 passes, rather than 4 or 8 as in the original and first modified forms.

It should be observed that the position of the exit beam is now fixed. As M2 is moved to change the number of passes the exit beam is stationary, dimming as one of the spots misses one of the components of M3, but reappearing at the same position for the new number of passes. Note that no changes are required in the main, expensive, optics of the system and that the modifications can be readily removed and the output port repositioned.

White has also stated [12] that the symmetry of the system is such that the effects of turbulence on spot size is considerably reduced. Although no analysis was presented, one would expect that the folding of the rays about the central ray would produce such an improvement, as it does for the cats-eye interferometer as compared to the plane mirror interferometer.

The second roof does not add to the number of rows of images, but adds new images between the first set. It may, therefore, limit the number originally used and in practice not necessarily increase the available path length because of difficulties resulting from the small required size of the second roof mirror.

A multi-pass system of the White type was therefore selected, with provisions for adding both roofs if desired, although it is believed one will be sufficient. To retain flexibility, and also avoid the mechanical stresses of cutting a finished mirror, the usual notches in M3 will be replaced by two small turning mirrors, which form a periscope to displace the beam laterally.

Other specific details of the optics and their mounting will now be discussed.

White cell optics are frequently fabricated as a single large mirror, to assure a common radius of curvature, and then cut into three smaller mirrors for use. This produces two problems we wished to avoid. One is the release of internal local strain on cutting, allowing some distortion of the surface. On a well annealed blank this may not be serious. The second problem is mirror thickness, which for proper stability in grinding and handling is usually  $1/6$  the mirror diameter. The mirrors resulting from cutting are thus at least twice as heavy, and the greater thickness increases their adaptation time to a new temperature.

The radius of curvature of the mirrors themselves will change with temperature, and for a 10 meter radius, a pyrex mirror would be expected to change 2 mm. As explained previously, this effect is magnified by the number of passes, resulting in a significant change in the output beam. Although correctable, it is preferable to avoid the difficulty and use Cervit, with a temperature coefficient nearly negligible over most of the range, but about 0.03 that of Pyrex at the minimum temperature planned. Three 10 inch diameter mirrors of fine annealed Cervit were therefore specified, with radius of curvature of 424.62 inches to match an existing test plate. The radii will be matched to within 1 mm. As a point of information, fabrication from a single large blank would have been approximately three times as expensive.

The thermal expansion of stainless steel is 200 times that of Cervit; even Invar is 16 times greater. The mounts must therefore allow for differential expansion, and must also be capable of smooth adjustment over a wide range of temperature and pressure. Either a flexure mount or a three-ball kinematic system would appear satisfactory, and the kinematic technique was chosen in this case.

Each mirror with its mount will weigh approximately 20 pounds. As shown in Fig. 5, this mass is supported by a ball and cone arrangement under the mirror, and on its vertical center line. This constrains the mirror against translation. The constraint against motion of the vertical axis is a ball in a vertical V-groove, which still allows thermal expansion along this line, as well as any reasonable machining tolerance. Motion of the ball normal to the mirror plane allows adjusting vertical tilt. The third constraint is a ball and flat, for adjusting horizontal tilt. The adjustments are orthogonal to avoid coupling of the adjustments.

To allow rapid alignment and adjustment of the number of passes, possibly under automatic control in the future, all fine adjustment of the mirrors is performed by stepper motors. These assemblies, shown in Fig. 6, mounted on the mirror support structures, drive the two movable balls of the kinematic mirror mount. They are enclosed in a sealed stainless housing and consist of a 200 step per revolution stepper motor driving a non-backlash gear mounted on a heavy duty micrometer spindle. The resulting change in image position at the other mirror plane is approximately 15 microns. This motion is cumulative with repeated passes, and for very long paths may be considered to be of the order of a diffraction-limited spot diameter or of the aberration limited spot.

To adjust the mirror spacing, the mount for M3 is on a sliding table driven by an identical stepper drive. The table rolls upon three balls, two in collinear V-grooves and one on a flat.

The mirror support structures are mounted on the three legs brought through the bellows joints of the vacuum chamber as previously described. Connections to the stepper drives are enclosed in stainless conduit, which can also serve to evacuate the drives if desired.

#### ACCESSORY CONSIDERATIONS

The space for the new absorption cell is quite good. The floor (6 inch concrete) will support the required loads, and computer room raised flooring is already in place so that piping and electrical service can be placed out of the way. Although there are no manufacturing operations in the building or nearby heavy traffic, the usual vibrations from air conditioning and ventilation systems exist. The general physical site is shown in Fig. 7. In addition to the absorption cell and its associated equipment, a computer system consisting of two SEL 810B main frames with associated discs, tape drives, and communication interfaces will occupy most of the 33 x 66 room. The computer system can be time-shared with the existing White cell, spectrophone laboratory, and laser diode laboratory which are nearby.

A support structure, now being designed, is indicated in the figure. The absorption cell and the optical tables will be on a single air-supported mount. A pair of I-beams will support the absorption cell and connect rigidly with the optical table support, a pair of I-beams making an asymmetrical T. For a static three-point mount, the air supports are



interconnected in groups, each with its own air reservoir to lower the natural frequency. Valving can produce viscous forces and damping, optimized to the particular site by accelerometer measurements of the system. The groupings will be: the large side table; the end table and cell input; the dual-mirror end of the cell and the center cell support.

The static deflection of the mount by the system is not a problem, since the optics will be adjusted in this condition. Forces created at the bellows by evacuation appear to create negligible deflection if proper support points are used. Vibration-creating apparatus on the mount should be avoided, including entrained bubbles in the coolant and other pressure surges. The mount allows for additional inertial mass loading, if required.

Thermal loss through the vacuum chamber support structure is approximately 10 BTU for a 1/2 square inch support six inches long. Although not a problem insofar as refrigeration capacity is concerned, the supports must be thermally insulated or separately cooled if pronounced temperature nonuniformities are to be avoided. The thinner sections possible for vacuum and sample lines will make these connections less of a problem. Optical ports will have dewared windows.

The optical tables for mounting the lasers, spectrometers, and detectors will be a 6 x 8 and a 6 x 10 foot slab of limestone. This material is inexpensive and has proved to be an excellent support for permanent installations. Provision will be made for preserving a dry nitrogen atmosphere in this area. The supports will allow a large vacuum tank if this is needed later.

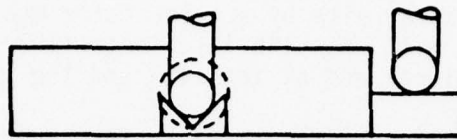
#### CURRENT STATUS

As of this writing, detailed design of the main vacuum chamber and the main optical mounts, supports, and adjusting mechanisms has been completed. The long leadtime items, the main optics and vacuum chamber, are on order. Quotations are being sought for machining the mounts, although some of this will be done in our own shops. A design has been established for the support structure, and it is now being detailed. The new space is being prepared for the installation of the equipment.

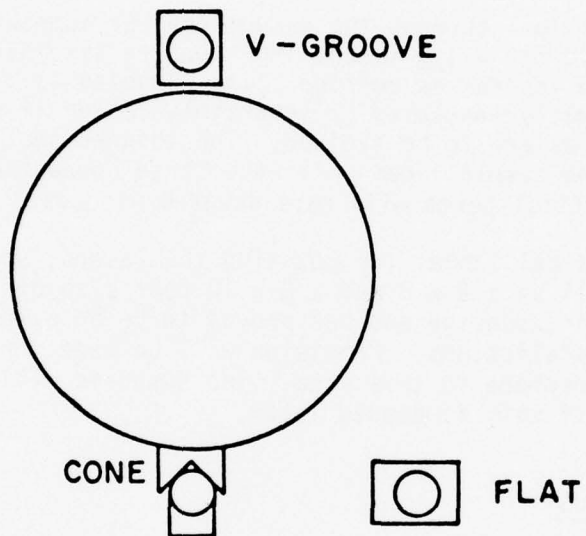
With general specifications now established, design work will proceed on the refrigeration and vacuum systems, sample manifolding, and the auxiliary coupling optics. No untoward difficulties are currently foreseen in having the cell operational by mid-year, although some subsequent shakedown period and learning curve will undoubtedly occur, in particular with the data processing interface.

The resulting system is expected to be a significant addition to existing facilities and offer unique capabilities over the next decade.





TOP VIEW



FRONT VIEW

Fig. 5. Kinematic Mirror Mount.

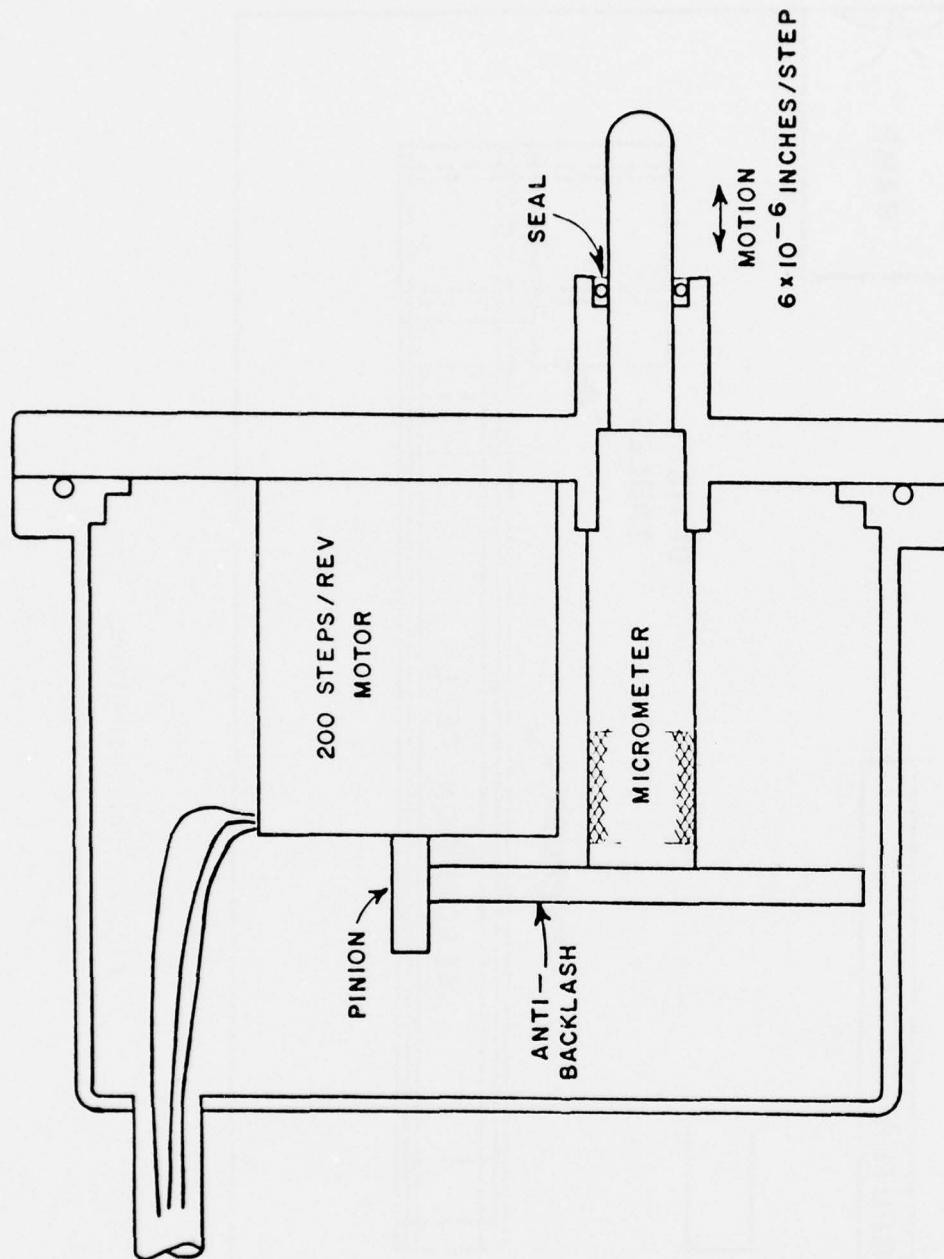


Fig. 6. Stepper Drive.

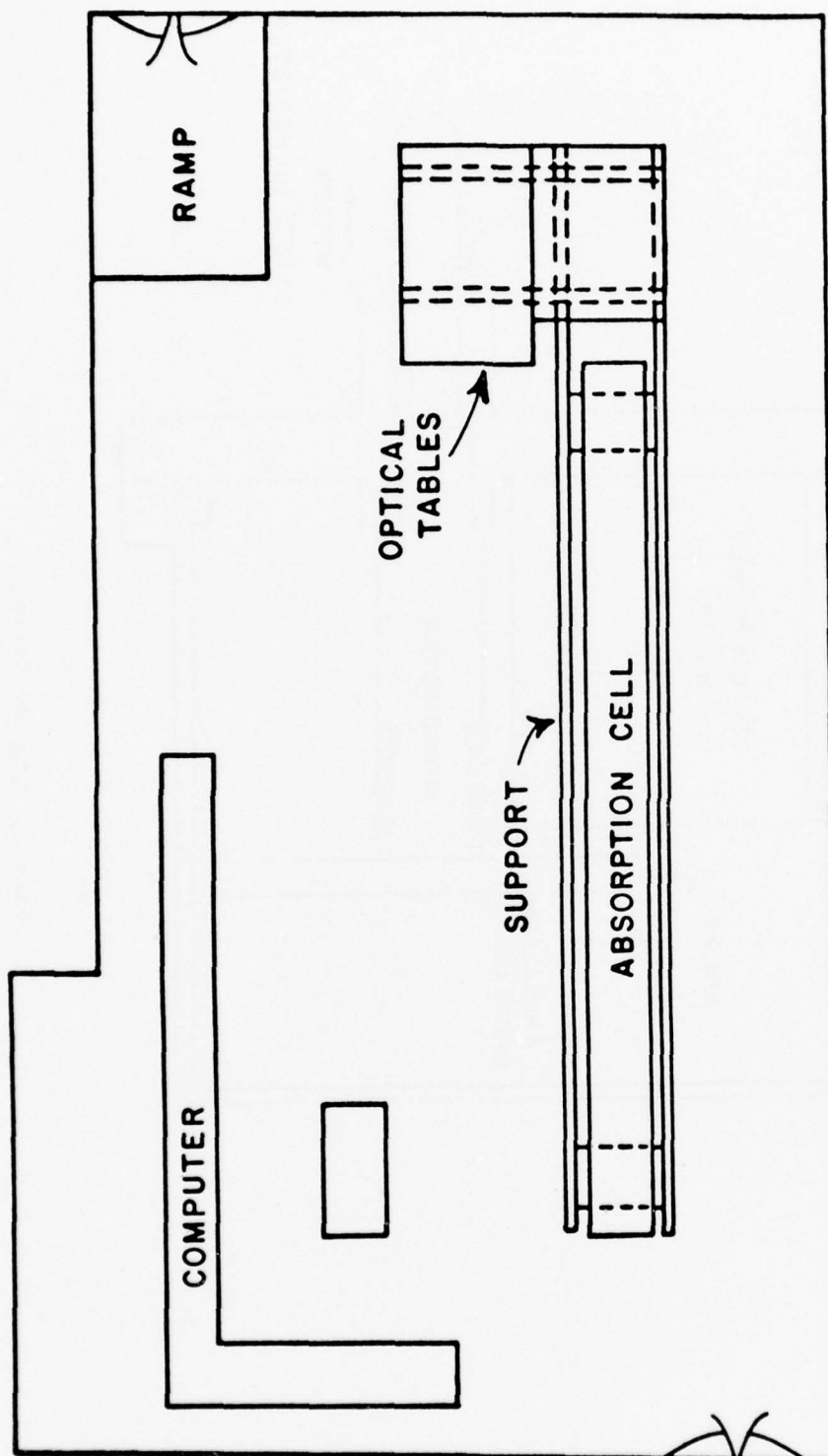


Fig. 7. Physical Sitting.

## REFERENCES

1. J. U. White, J. Opt. Soc. Amer. 32, 285(1942).
2. H. L. Welsh, C. Cuming and E. J. Stansbury, J. Opt. Soc. Amer. 41, 712(1951).
3. G. Herzberg, Astrophys. J. 115, 337(1952).
4. A. Watanabe and H. L. Welsh, Can. J. Phys. 43, 818(1965).
5. D. R. Herriott and H. J. Schulte, Appl. Opt. 4, 883(1965).
6. R. P. Blickensderfer, G. E. Ewing, and R. Leonard, Appl. Opt. 7, 2214(1968).
7. A. R. W. McKellar, N. Rich, and V. Soots, Appl. Opt. 9, 222(1970).
8. D. Horn and J. C. Pimentel, Appl. Opt. 10, 1892(1971).
9. E. O. Schulz-DuBois, Appl. Opt. 12, 1391(1973).
10. P. L. Hanst, A. S. Lefohn, and B. W. Gay, Jr., Appl. Spec. 27, 188(1973).
11. P. L. Hanst, in Advances in Environmental Science and Technology, Vol. 2, Edited by Pitts and Metcalf, Wiley, 1971.
12. J. U. White, "Very Long Optical Paths in a Near-Confocal System" presented at 1975 Annual Meeting, Optical Society of America.
13. R. K. Long, "The Ohio State University Optical Frequency Space Propagation Simulator", Report 1083-11, ElectroScience Laboratory, Ohio State University, 15 October 1961.
14. W. R. Watkins, Appl. Opt. 15, 16(1976).



PART C  
TUNABLE SEMICONDUCTOR LASER SPECTROSCOPY OF CO<sub>2</sub>,  
N<sub>2</sub>O, AND H<sub>2</sub>O IN THE 5-MICRON REGION

Contents

	Page
INTRODUCTION	C-1
EQUIPMENT DESCRIPTION	C-3
A. Laser Diode	C-3
B. Liquid Helium Dewar	C-9
C. Vacuum System	C-10
D. Optics	C-12
E. Electronic Instrumentation	C-14
EXPERIMENTAL PROCEDURE AND RESULTS	C-17
A. Simulated CO Laser Transmission	C-17
B. CO <sub>2</sub> and N <sub>2</sub> O Absorption Line Parameters	C-25
CONCLUSIONS	C-62
REFERENCES	C-63
APPENDIX	
A. LORENTZ LINE SHAPE DATA	C-65
B. VOIGT LINE SHAPE DATA	C-74
C. SPECTRAL LINE INTENSITY	C-82

## CHAPTER 1

### INTRODUCTION

Even though the laser is a relatively recent development its applications have extended to many fields. The reason for this growth is that the laser is a fundamental source of monochromatic, directional, and coherent infrared and optical radiation. In the field of spectroscopy the laser is revolutionizing the experimental techniques employed, so that measurements can now be made that were never before possible.

Infrared laser spectroscopy has evolved into two major areas, linear and nonlinear. Nonlinear laser spectroscopy covers absorption saturation, two-photon resonance, and trapped particle spectroscopy techniques [1]. Linear laser spectroscopy uses a tunable laser with narrow line width (about 1 MHz), a similar technique to the scanning spectrometer except with much greater resolution capabilities [2]. A variety of lasers are tunable but of particular interest to this report is the tunable semiconductor laser and its application to linear laser spectroscopy.

The use of laser diodes in spectroscopic experiments was first demonstrated by MIT Lincoln Laboratory [2]. The tunability of the laser allows the recording of the spectroscopic signature of particular gases. Although the tuning range is somewhat narrow (unless elaborate techniques are employed) enough lines can be observed to identify a known gas. This fact has applications in pollution monitoring of atmospheric gases as discussed by Hinkley and McNamara [3,4]. Also, measurements of the gain line shape of a CO laser with respect to frequency have been performed by Blum et al. [5]. Experiments examining spectral line shape parameters using laser diodes can accurately resolve Doppler lines and fine energy level splitting [2,6]. The major drawback that semiconductor laser diodes have is the requirement for liquid helium cooling. However, the new generation heterostructure laser diodes offer a wide tuning range, greater output power, and can be operated up to liquid nitrogen temperatures [7].

Most of the spectroscopic work with laser diodes has been above 6  $\mu\text{m}$  using PbSnTe; however, this study examines the 5  $\mu\text{m}$  region using a PbSSe laser. Previous work in the 5  $\mu\text{m}$  region includes studies of CO, NO, and H<sub>2</sub>O [2,6,8,9]. The analysis of H<sub>2</sub>O is the most extensive including measurements of line shape parameters and relative line positions. Much work can be done,

because the use of laser diodes is still in the beginning stages in this frequency region. It is the intention of this study to examine atmospheric spectroscopy and its related experimental techniques using a semiconductor laser. The need for measurements involving CO laser transmission in a H<sub>2</sub>O-N<sub>2</sub> mixture, at frequencies no available small laboratory CO laser could deliver, suggested the use of the laser diode to simulate the CO laser. CO<sub>2</sub> and N<sub>2</sub>O, both atmospheric absorbing gases, were examined in the tuning range of the laser 1945-1980 cm<sup>-1</sup>, and the results were compared with the AFCRL tabulation for these molecules.

## CHAPTER 2

### EQUIPMENT DESCRIPTION

This chapter discusses the experimental apparatus used. Five major areas will be covered: the laser diode, the liquid helium dewar, the vacuum system, the optics, and the necessary electronic equipment.

#### A. Laser Diode

We are grateful to Dr. Ken Hill of MIT Lincoln Laboratory<sup>1</sup> who supplied the laser diode used in these experiments and without whose cooperation the work would not have been possible.

Tunable semiconductor lasers are available in a variety of material compositions. Figure 1 illustrates not only the different compositions but also the frequency ranges of the devices. The laser diode used in this experiment is of  $\text{PbS}_{1-x}\text{Se}_x$  composition. The variable "x" in the chemical formula represents the doping concentration which controls the frequency output of the laser within bounds indicated in Fig. 1. A particular diode can cover

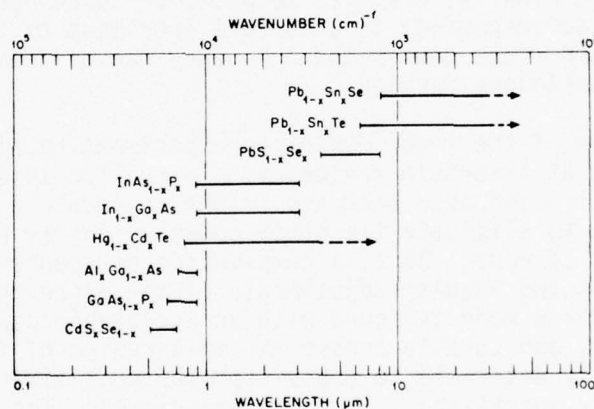


Fig. 1. Composition-tuned semiconductor lasers [4]

<sup>1</sup>Now with Laser Analytics, Inc., Lexington, Massachusetts.



a range of around 40 wavenumbers using current tuning. Current, i.e., temperature, tuning of the diode junction, varies the output frequency by linearly changing the bandgap energy. Temperature tuning provides a nearly linear frequency variation, which allows easy analysis of the data.

The properties of the output radiation from the laser are of special interest.<sup>1</sup> The most important property is that the radiation is monochromatic to a high degree. An estimated line width of 1 MHz at 8  $\mu$ w was reported by Dr. Nill's group [6]. The importance of this is illustrated in Fig. 2 which shows the improvement laser diode spectroscopy can achieve over conventional techniques. This property plus the diode's capability to be tuned make it a very powerful device. The laser will oscillate at several different frequencies simultaneously. A single tunable laser line is termed a mode. Figure 3 shows a spectrometer scan of the laser at two fixed currents. This gives an indication of the number of modes available simultaneously, and the increased number of modes and intensity of modes as the current is raised above threshold ( $\sim 200$  ma). Because of the tunability property of the laser diode, if the mode spacing is small an overlapping of modes can result. This is illustrated in the wavenumber versus current plot of Fig. 4. Different resonant cavity configurations can result in multiple output beams. This is illustrated for one of our diodes by the output radiation pattern of Fig. 5, where three beams are evident. The output power for a mode is not uniform, tending to drop to lower values near the current limits for the mode. Finally, a single mode can be tuned normally between  $0.7$ - $1.0$   $\text{cm}^{-1}$  corresponding to a current increment of 50 ma. In this manner our diode covers the frequency region from  $1945$ - $1980$   $\text{cm}^{-1}$  in a quasi-continuous fashion.

Operation of the laser during an experiment requires attaining a single mode at a certain frequency. To realize this, a grating spectrometer is used as a bandpass filter to locate a particular frequency and to eliminate the other modes which may be generated at the chosen current. Next, a combination of scanning the power supply current and angular adjustments of the diode mount are performed until a mode is found with an acceptable power level, stable output, and tunable across the full region of interest. It is generally desirable to use a test for mode mixing (i.e., dual frequency operation). In these experiments, the tunable radiation was passed through a  $1.876$  cm long germanium Fabry-Perot etalon. An examination of the quality of the recorded fringe pattern reveals the presence or absence of a second frequency. Figure 6 gives an example of a pure mode pattern and a mixed mode pattern. The curve for the mixed mode shows different fringe spacings on each half of the scan. The observed dip in the middle of the signal intensity marks the end and beginning of the different

---

<sup>1</sup>For details on Pb-salt diode properties, reference is made to Butler [10].

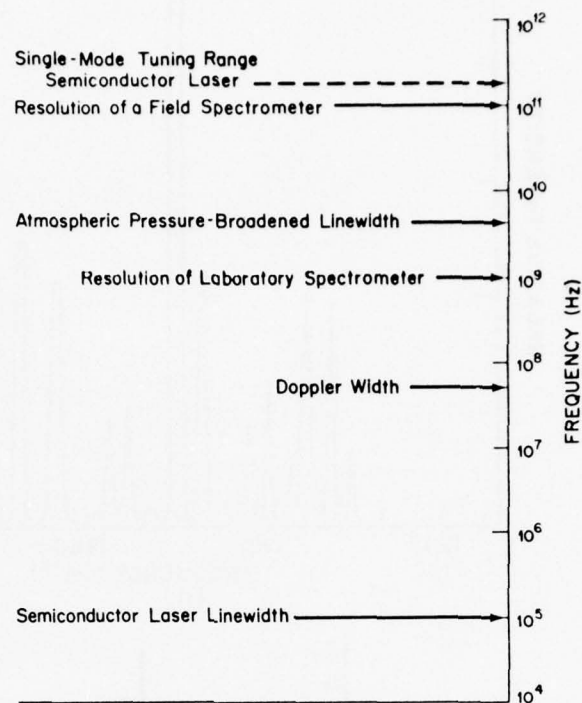


Fig. 2. Semiconductor laser resolution [4].

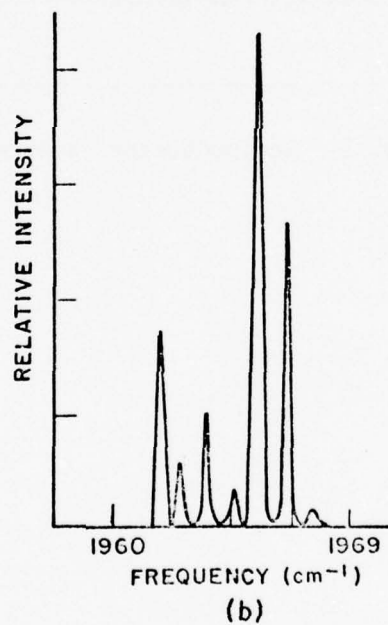
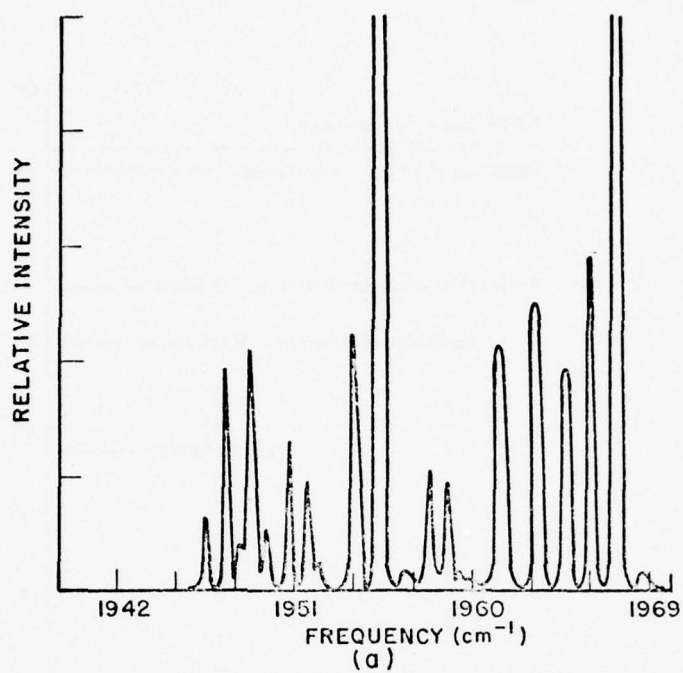


Fig. 3. Spectrometer scan of laser at fixed currents: (a) 600 ma, (b) 260 ma.

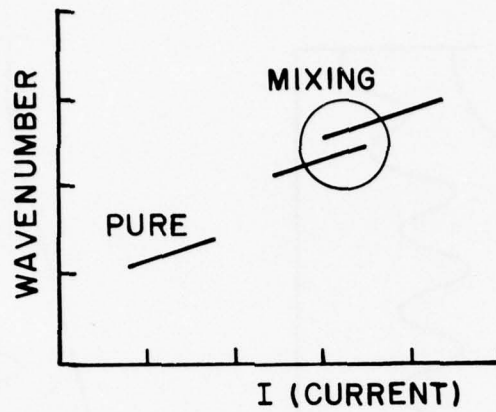


Fig. 4. Pure and mixed laser modes.

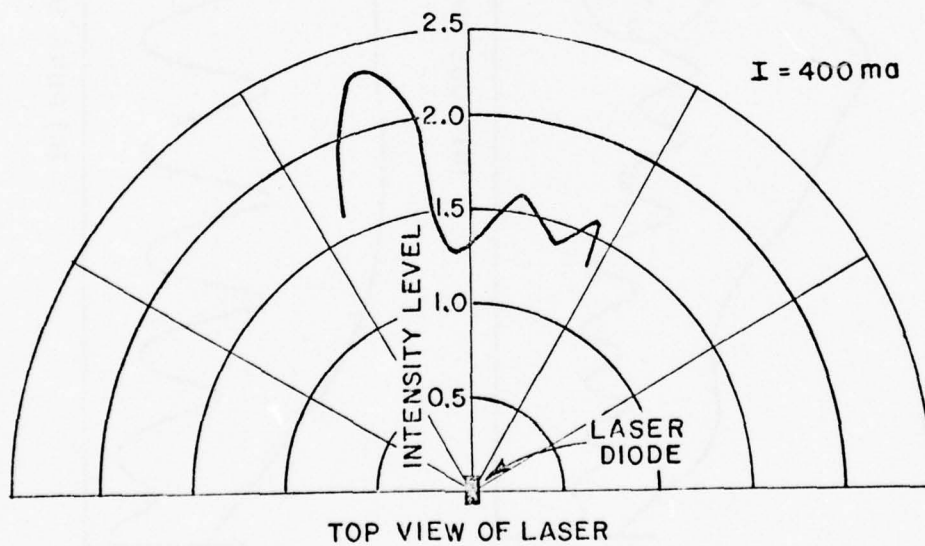
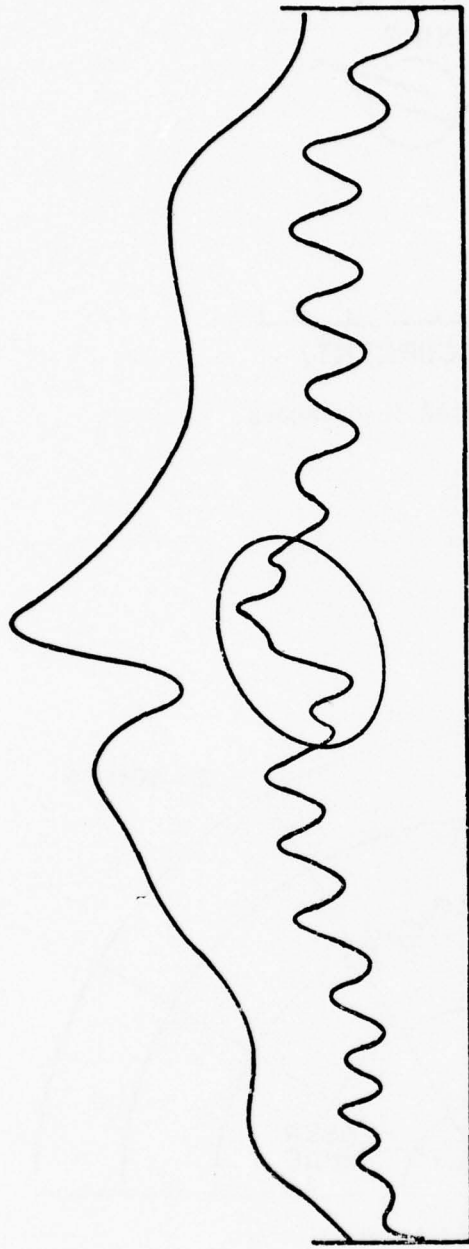


Fig. 5. Radiation pattern of laser.





(a) MODE INTERSECTION



(b) PURE MODE

Fig. 6. Fringe pattern of (a) pure and (b) mixed laser modes.

modes. Once a pure mode is found, the current limits are set for a scan and the experiment proceeds.

The  $\text{PbS}_{1-x}\text{Se}_x$  diodes must be operated at liquid helium temperatures (10 K or below). The laser action begins at a certain threshold current, typically 0.2 amperes, and continues to an upper limit of approximately 1.2 amperes (corresponding to the highest frequency). The upper limit of current is determined by thermal considerations which are related to diode construction, mounting, etc. In this case, diodes were operated within specifications supplied by Dr. Nill.

#### B. Liquid Helium Dewar

A Janis Research Model 6 DT research dewar and optical tail was used to house the diode. The dewar has three main sections: a liquid nitrogen container, a liquid helium container, and a high vacuum jacket. At the base of the liquid helium container is a cold finger containing a mount for the laser diode and an optical window. The dewar, which holds five liters of liquid helium, maintains cooled temperatures at the tail for about eight hours under normal operating conditions.

Because of the importance of maintaining a low temperature environment about the laser, two auxiliary devices have been constructed. The first is a liquid helium level sensor which contains a buzzer to provide a warning when a low helium level is attained. A six-light display gives a continuous reading of the level in the dewar. The second device consists of a  $180\ \Omega$  carbon resistor attached to the diode mount and is used to measure the temperature. Because of the large variation of resistance at low temperatures a carbon resistor is an excellent sensor [11]. The value of resistance is determined by measuring the voltage across and current through the resistor, which must be done at very low power ( $\sim 1 \times 10^{-6}$  watts). With the laser diode off, the measured temperature at the tail is between 10 to 11 K. The temperature is above liquid helium due to radiation received from the external environment through the optical window.

A cool-down procedure for the Janis dewar was developed to eliminate moisture collection inside the cryogenic sections, in particular on the container in thermal contact with the diode. This is important because moisture in the tail could result in thermal insulation of the laser diode from the cryogenic temperatures.

To increase the lifetime of the laser, it was stored at liquid nitrogen temperatures continuously. The cold temperatures retarded the diffusion of the indium and gold coatings which form

the electrodes. The indium-gold mixture forms a resistive deposit, which heats the junction during operation, a very undesirable situation. Continuous storage of up to a month was achieved.

### C. Vacuum System

The holding time of the liquid helium depends greatly on the vacuum obtained in the dewar. Vacuums of  $10^{-8}$  torr were attained in the jacket of the dewar while it contained the cryogenic liquids.

To achieve these vacuums, an 8 liter/second Varian Vac Ion pump, model number 911-5000, was installed directly on the dewar. Thus the dewar could be continuously pumped while the cryogenic liquids were introduced, without contamination from the pumping system. This allowed the liquid nitrogen storage of the dewar over long periods of time as previously mentioned. Because the Vac Ion does not pump helium efficiently, liquid helium storage of the dewar was limited to about one week. At this time, the dewar vacuum was unacceptable for laser diode operation.

A two-inch oil diffusion pump, CVC VMF-10, is used to start the Vac Ion pump at  $5 \times 10^{-5}$  torr. The diffusion pump itself is capable of  $1.2 \times 10^{-6}$  torr. A Granville-Phillips two-inch cryosorb liquid nitrogen cold trap is located above the diffusion pump to keep backstreaming of oil molecules to a minimum. The mechanical roughing pump that backs the oil diffusion pump is a Cenco Hyvac 14 capable of 5 microns. The mechanical pump is also used to evacuate the test cells employed in the experiment. Figure 7 is a diagram of the vacuum system.

To monitor the pressures obtained, several gauges were used. For general pressure measurements, a thermocouple gauge located above the mechanical roughing pump and a NRC type 530 alphasatron radium ionization gauge were used. For the high vacuum measurements, the Vac Ion power supply meter acts as a vacuum gauge. A CVC type VG-1A ionization gauge was also used. The pressure indicators for the sample cells were a U-shaped mercury manometer and a Wallace and Tiernan mechanical gauge. The mercury manometer had an accuracy of plus or minus one torr and the mechanical gauge was accurate to a few tenths of a torr. For lower pressures, the mechanical gauge was used. Since the mechanical gauge was only capable of reading up to 50 torr, the mercury manometer was used at higher pressures.

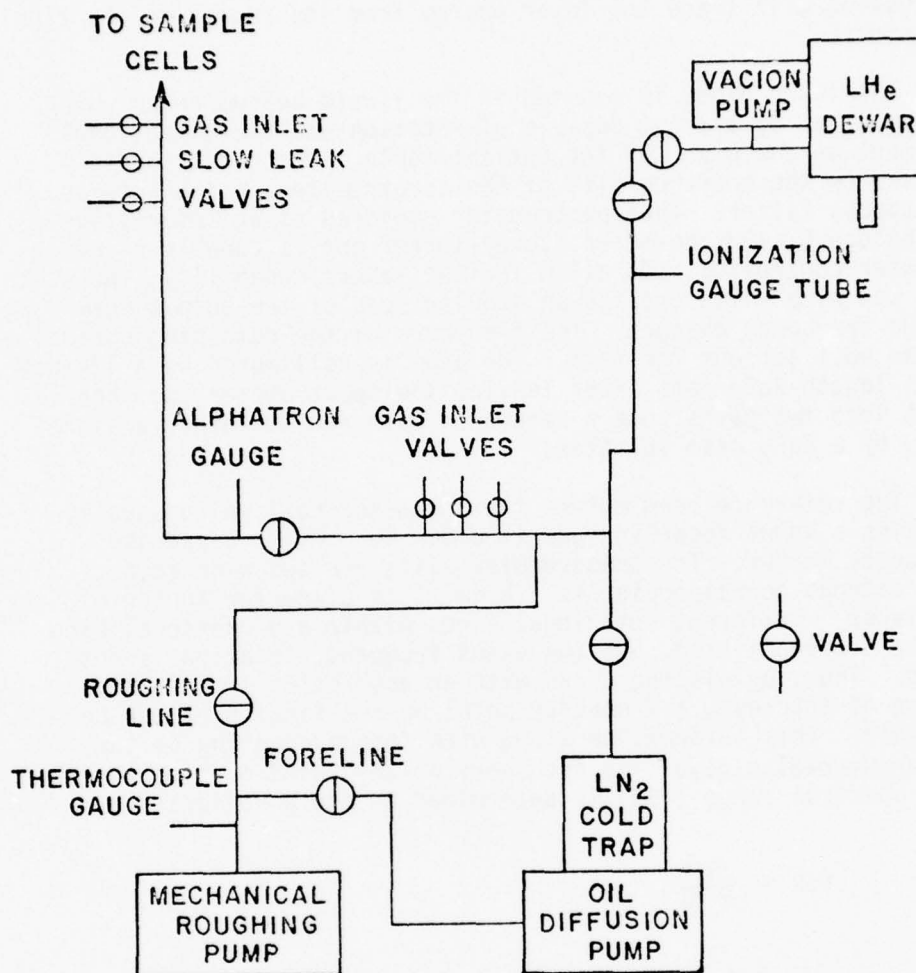


Fig. 7. The vacuum system.



#### D. Optics

The basic optical components are illustrated in Fig. 8. The discussion will trace the laser energy from its source to the final detectors.

The laser diode is mounted in the liquid helium dewar which is supported by a mount capable of rotation and two-dimensional movement on the plane of the optical table. The radiation is focused on the entrance slit of the spectrometer, which acts as a bandpass filter. The spectrometer employed is an Interactive Technology CT-103 one-meter Czerny-Turner and is capable of being computer controlled. To allow for the lasers tunability, the slits were set wide which creates an angular scan of the output beam as the frequency changes. The f-numbers of the remaining optical system must account for this. The beam is collimated by a 12-inch focal length BaF<sub>2</sub> lens after leaving the spectrometer and then is split into two paths, one a reference path and the other a signal path, by a CaF<sub>2</sub> beam splitter.

The reference beam enters the one-meter cell which usually contains a known absorbing gas in order to provide a precise frequency marker. The spectrometer slits are set wide (e.g., 1000 microns corresponding to 1.5 cm<sup>-1</sup>) to allow for tuning of the laser. Different rotational lines within a vibrational band can be differentiated, but the exact frequency location is not known. Thus, by placing a gas with an absorption line in the region of interest, a frequency point on the final plot can be obtained. This information along with fringe counting of the germanium etalon gives the frequency at any point on a plot. The free spectral range (FSR) is determined by the equation:

$$(1) \quad \text{FSR} = \frac{1}{2nL}$$

where  $n$  = index of refraction of etalon  
 $L$  = length of etalon.

The index of refraction as a function of frequency is given by [12]

$$(2) \quad n = 3.9832 + 1.6403 \times 10^{-5} \gamma$$

where  $\gamma$  = wavenumbers (cm<sup>-1</sup>).

The etalon length has been measured to be 1.876 cm. Thus, the FSR can be accurately obtained. A nominal value for the 5-micron region is 0.0664 cm<sup>-1</sup>. Although the FSR shows very little temperature

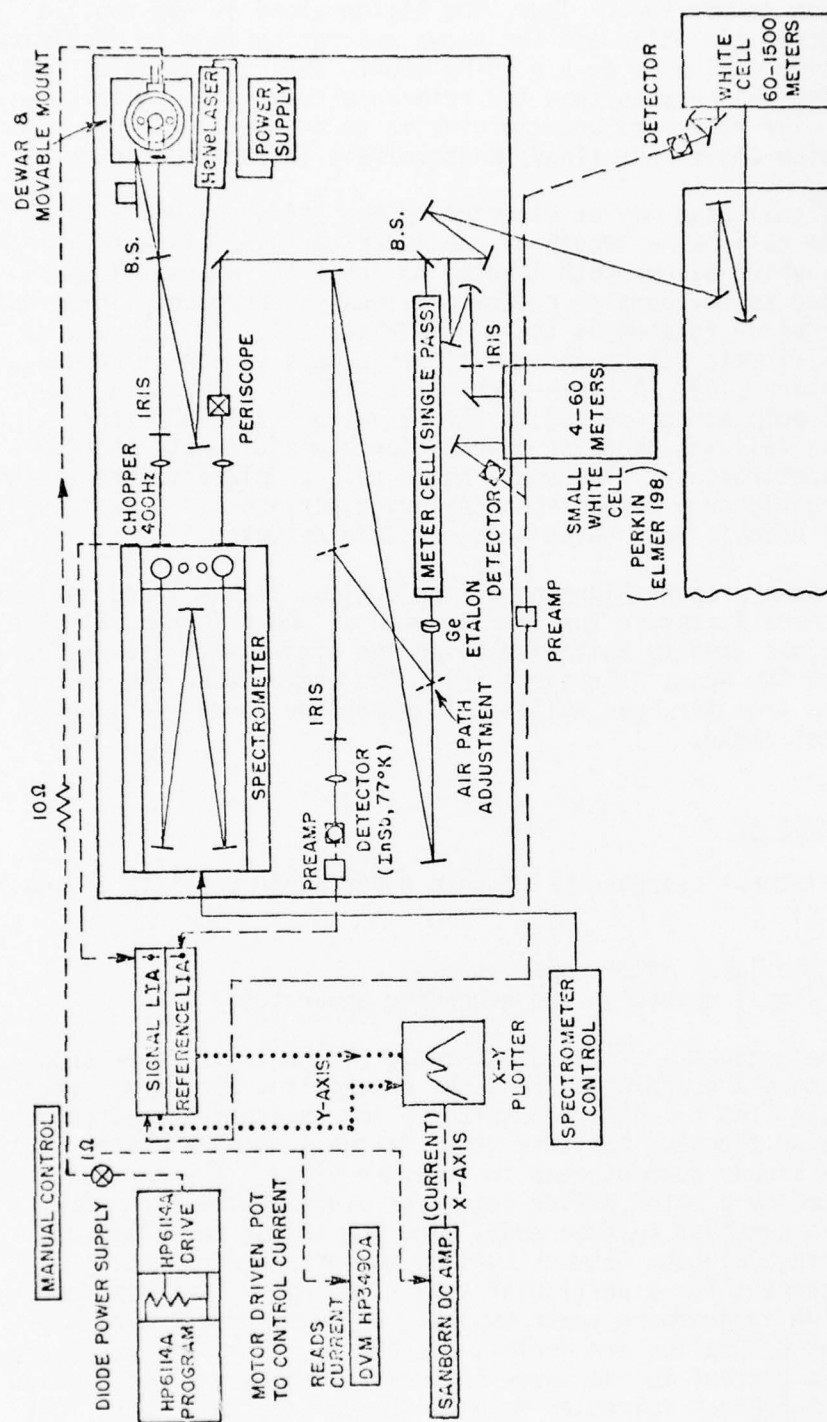


Fig. 8. Laser diode experimental apparatus.

sensitivity, the position of the fringes on a frequency axis is dependent on temperature. Thus, the etalon alone is not capable of frequency calibration and the known absorption line is necessary. The germanium etalon is on a sliding mount, thus it may be easily removed from the beam so that the reference curve can be directly recorded. The reference beam terminates on a liquid nitrogen cooled indium antimonide (InSb) photovoltaic infrared detector.

The signal beam may be directed to two different White-type cells. One cell has a length of one meter and a multiple traversal capability which allows path lengths to about 60 meters. The cell is connected to the pumping system previously described. This test cell shall be designated as the small White cell. The other test cell is 16.15 meters long and can attain a path length of around 1.5 kilometers [13]. A seven-inch oil diffusion pump and a 100-cfm mechanical pump are connected to give a vacuum of  $1 \times 10^{-5}$  torr. The large White cell was used for transmittance measurements and low pressure spectroscopy. The small White cell complements the system by allowing higher pressure spectroscopy experiments. From these cells, the beam is focused on a second InSb detector.

To insure proper alignment of the optics, it was found convenient to place three irises in the optical path as shown in Fig. 8. The HeNe laser was used to initially align the system with the irises centered on the beam. The first iris, the one between the laser and the spectrometer, was utilized to guarantee normal incidence at the spectrometer.

#### E. Electronics

The electronic apparatus of this experiment consists of two major parts:

- (1) the laser diode power supply
- (2) signal detection and recording apparatus.

Figure 9 gives a detailed schematic of the laser power supply. It can produce a scanning current for an oscilloscope curve-trace and also contains a modulation suitable for derivative spectroscopy. Of particular interest for this study is the scan mode which simply provides a linear current ramp to tune the diode. The current ramp is generated by a motor driven pot which programs the d.c. power supply in a constant voltage mode. The low adjust potentiometer, in the voltage divider network outside the programmer, sets the starting current for a particular scan. The upper limit is determined by the programming power supply. Both the programming and driving power supplies are Hewlett-Packard Model 6114A precision supplies. The current to the laser is monitored by a Hewlett-Packard 5-1/2 digit digital voltmeter Model 3490A, which facilitates the determination of the proper settings for the laser power supply scan.





From the detectors in the optical system, the electrical signal is sent to Princeton Applied Research lock-in-amplifiers (LIA), Model 128, one for the reference signal and one for the sample signal. Figure 8 illustrates the design of the signal detection and recording system. From the LIA's, the electrical information goes to the y-axis of a Hewlett-Packard Moseley 135M x-y recorder. The x-axis of the plotter represents the current of the laser diode, which directly corresponds to the output frequency. Thus, the x-y recorder displays the intensity versus the frequency of the laser beam at the detectors.

## CHAPTER 3

### EXPERIMENTAL PROCEDURE AND RESULTS

This chapter discusses the measurements made of simulated CO laser transmittance in  $\text{H}_2\text{O}-\text{N}_2$ , and  $\text{CO}_2$  and  $\text{N}_2\text{O}$  line shape parameters.

#### A. Simulated CO Laser Transmission

Two simulated CO laser line transmittance measurements in an  $\text{H}_2\text{O}-\text{N}_2$  mixture, with a total pressure of 760 torr, were made using the laser diode and large White cell. The purpose was to verify an experimental technique, described in the next paragraph, by comparing results with previous CO gas laser measurements. The CO lines are 6-5 P(10) line at 1973.299 and the 6-5 P(14) line at 1957.050.

During the experiment, the slit widths of the spectrometer were set at 1000  $\mu$  corresponding to a wavenumber difference of 1.5  $\text{cm}^{-1}$ . Thus, to locate the laser line frequency position within the passband of the spectrometer, a frequency marker is needed. As explained before, this is accomplished by introducing a suitable absorbing gas into the one-meter cell. For the 6-5 P(10) line, deuterium chloride ( $\text{DCI}^{35}$ ) was used which has an absorption line located at 1973.660  $\text{cm}^{-1}$ . For the 6-5 P(14) line,  $\text{H}_2\text{O}^{18}$  with an absorption line at 1957.010  $\text{cm}^{-1}$  was used, because of the strength of this line it could be observed at low pressures in the large White cell, i.e., the original sample was pumped down so that the line was observable but the wing effects were small.

Figures 10 and 11 are transmittance plots calculated from the AFCRL Line Compilation [18], which provides a good overview of the expected absorption characteristics. The 6-5 P(10) line is located in the wing region of many  $\text{H}_2\text{O}$  lines, thus, the absorption coefficient is not a rapid function of frequency. However, for the 6-5 P(14) line this is not the case, because it is located near the 752-643 010-000  $\text{H}_2\text{O}^{18}$  line. The position of this line must be accurately known, since it is also used as the frequency marker.

Eight separate measurements were made to secure one data point. Two separate plots were produced, each with four distinguishable curves: a signal curve, a reference curve, an etalon curve, and a

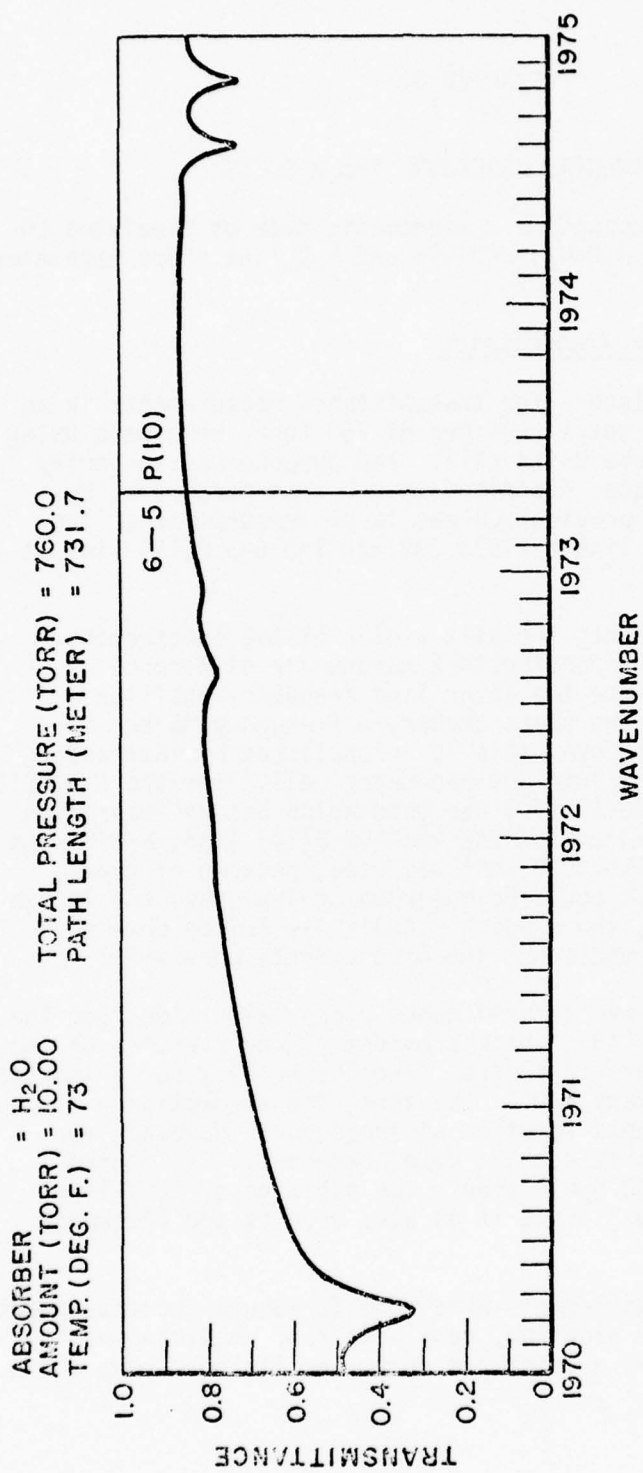


Fig. 10. Calculated transmission plot for 6-5 P(10) line.

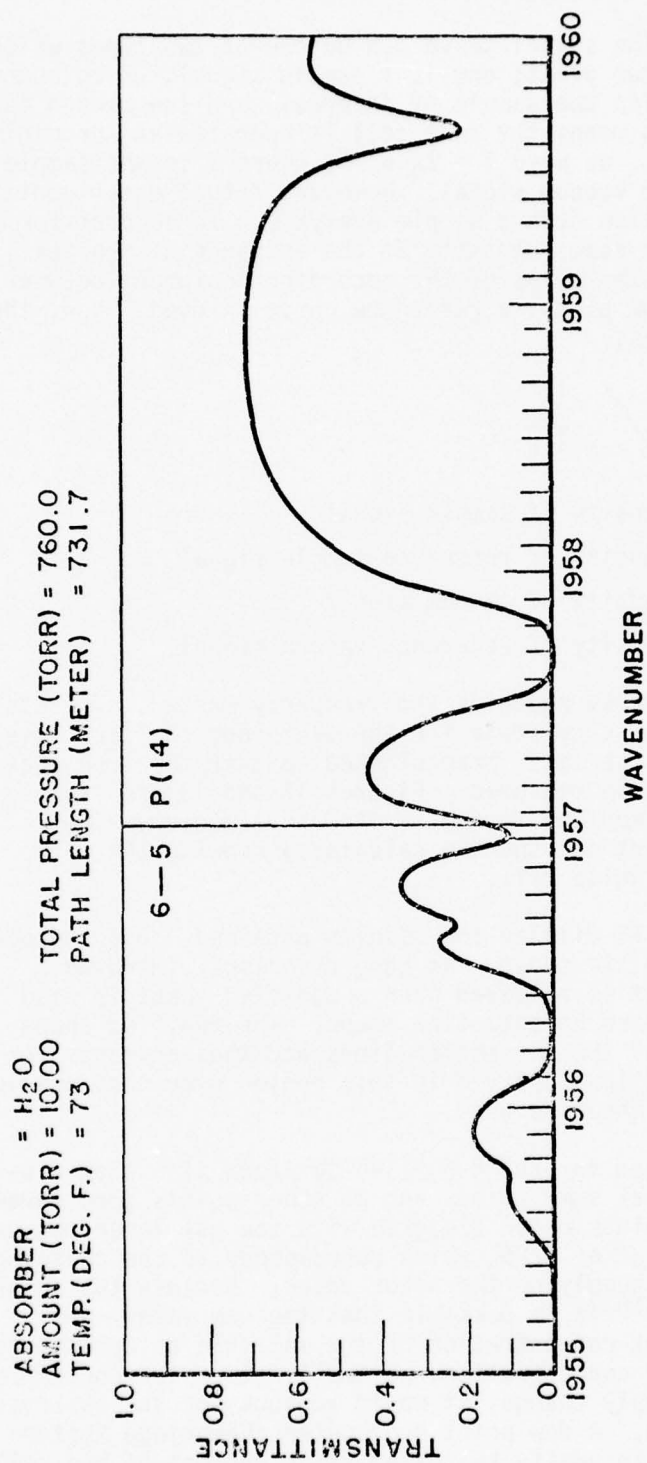


Fig. 11. Calculated transmission plot for 6-5 P(14) line.



zero level curve. The signal curve can be one of two types which differentiates the two plots; one is a sample signal, which means the test cell contains the sample of interest, and the second is a vacuum signal, which means the test cell is operated at the minimum obtainable pressure. We have  $I = I_0 e^{-kx}$ , where  $I$  is the sample signal and  $I_0$  is the vacuum signal. However, actual experimental conditions do not allow such a simple analysis. To account for changes in the laser beam intensity at the entrance of the test cell and changes in the gains of the recording equipment between the sample and vacuum plots, a reference curve is used. Now, the transmittance becomes,

$$(3) \quad T = \frac{I_S}{I_{RS}} \bigg/ \frac{I_V}{I_{RV}}$$

where  $I_S$  = intensity of sample signal  
 $I_{RS}$  = intensity of reference sample signal  
 $I_V$  = intensity of vacuum signal  
 $I_{RV}$  = intensity of reference vacuum signal.

The reference curve also contains the frequency marker. The etalon curve provides a frequency scale for the plots and the zero level curve is taken with the laser beam blocked so that the true background intensity can be measured. Figures 12 and 13 are examples of a typical measurement performed in the above manner. The absorption coefficient can then be calculated knowing the path length of the large White cell.

Figures 14 and 15 display the results obtained. Good agreement with Long et al. [14] is shown. As Long discusses, improved theoretical agreement is achieved when a modified shape is used instead of the standard Lorentz line shape. The modified shape enhances the wings of the absorption lines and thus accounts for the increased absorption observed in this region over that predicted when a Lorentz line shape is used.

The data obtained for the 6-5 P(14) CO laser line show disagreement with Long at some points and at other points good agreement. All of the points which disagree with the gas laser measurements were obtained after 9/20, which corresponds to the changing of the water bottle supplying the water vapor. Because the absorption line belonged to  $H_2O^{18}$  it is possible that the new water supply contained a different concentration of the molecule as opposed to  $H_2O^{16}$ . If the  $H_2O^{18}$  concentration was smaller than the concentration before the water supply change, it would account for the observed decreased absorption. A dew point hygrometer (Cambridge Systems Model 880) was used to verify the water vapor content of the cell with the measurement made during the initial evaporation of the

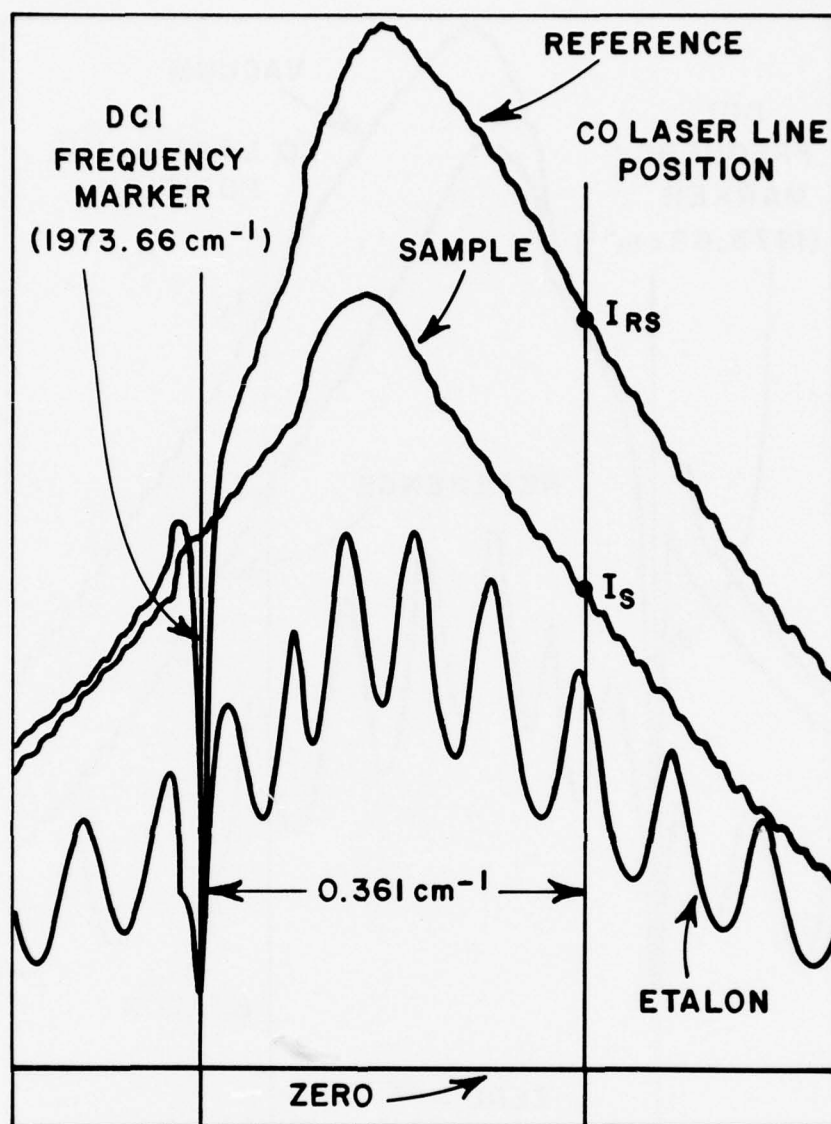


Fig. 12 Typical recorded data, sample plot.

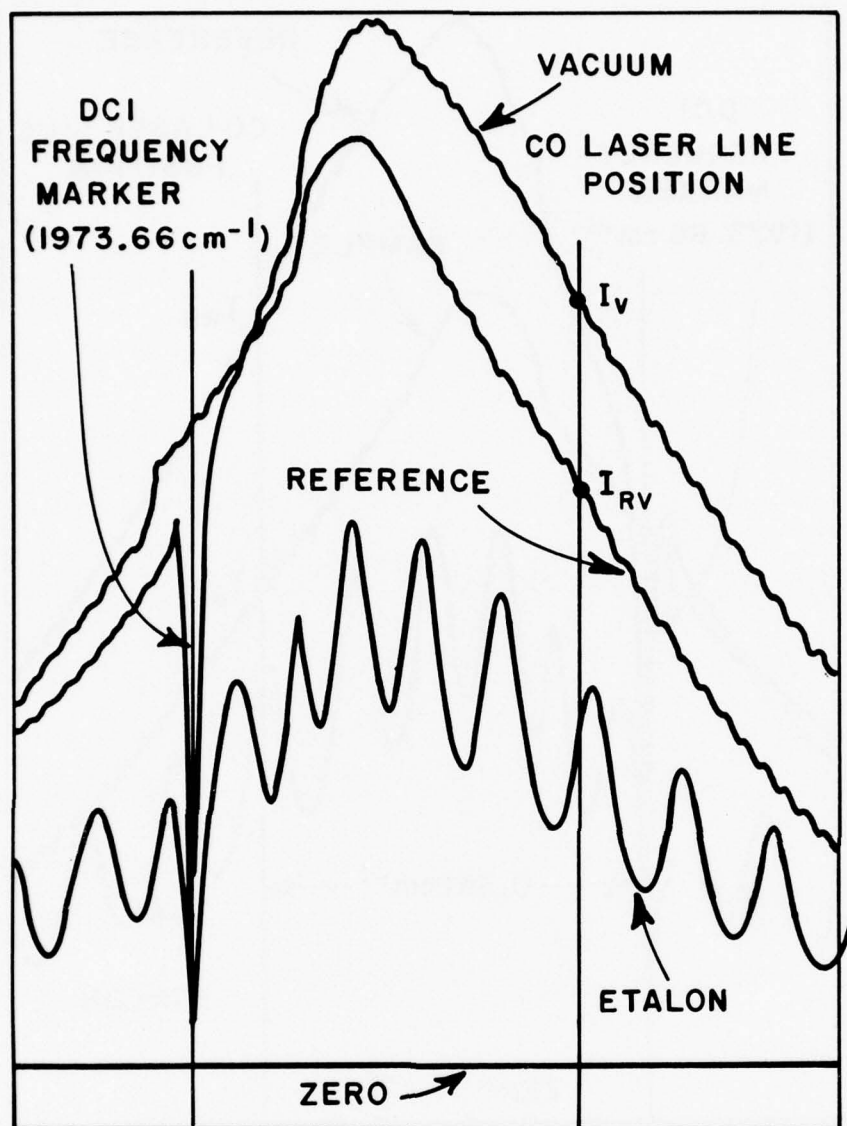


Fig. 13. Typical recorded data, vacuum plot.

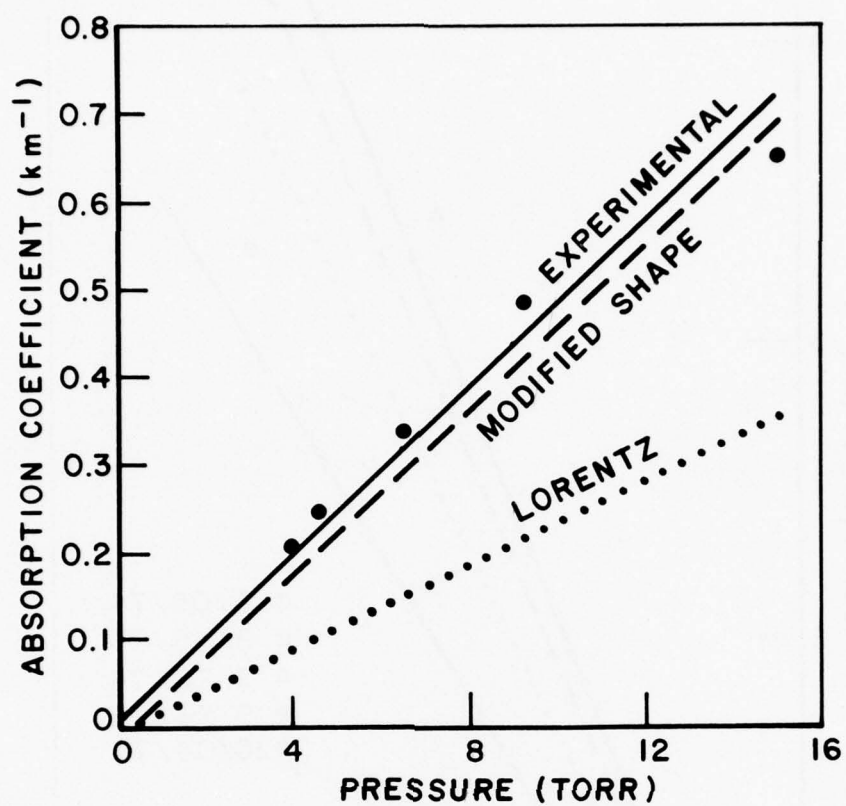


Fig. 14. Absorption coefficient versus water vapor-partial pressure, 6-5 P(10) line.



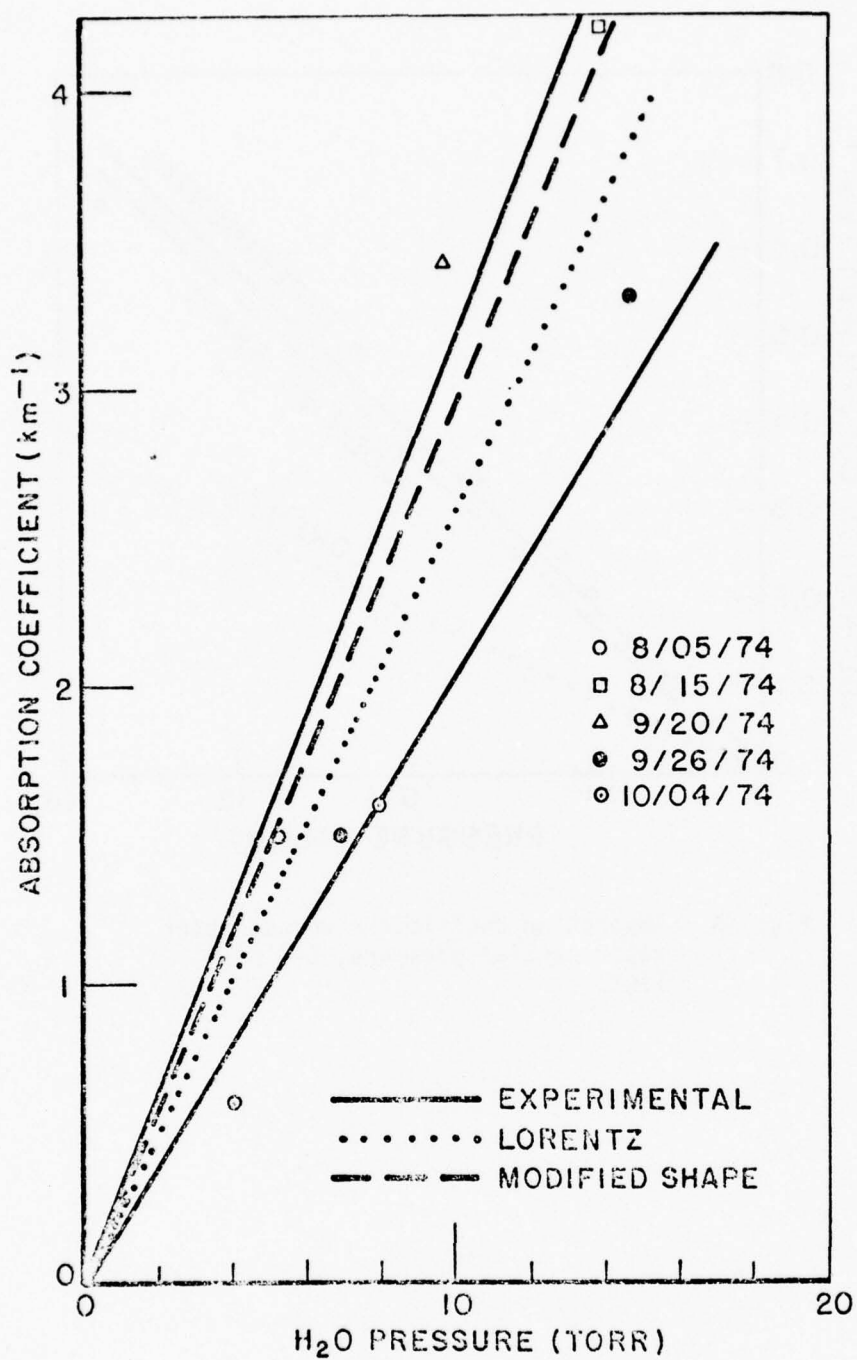


Fig. 15. Absorption coefficient versus water vapor-partial pressure, 6-5 P(14) line.

water vapor. The dew point measurements were consistent with the initial measurements which we take to indicate that there were no leaks in the filling system. Also, the laser diode could have been producing two separate tuning modes closely spaced in frequency. The vacuum signal curve shows two absorption lines about the distance of two peaks of the etalon curve apart. This could be due to contamination of the sample or a double mode from the laser. The exact problem is not known but the accuracy of the data obtained on 9/26 and 10/04 is in doubt.

#### B. $\text{CO}_2$ and $\text{N}_2\text{O}$ Absorption

##### Line Measurements

The true power in the tunable laser diode lies in its ability to enable the recording of spectra with high resolution. It is this facet of the laser diode that has been utilized in examining the absorption line parameters for  $\text{CO}_2$  and  $\text{N}_2\text{O}$ . The R-Branch of the  $11'0-00'0$  band of  $\text{CO}_2$  and the P-Branch of the  $20'0-01'0$  band of  $\text{N}_2\text{O}$  were examined. Values of halfwidths, absorption coefficients, line strengths, and broadening parameters were determined.

As with the CO laser line transmission measurements, eight curves were needed to obtain accurate line shape data. However, because the small White cell is fixed to the main optical table as shown in Fig. 9, it had good stability characteristics. This was not the case when the large White cell was used, because three separate structures supported the optical components in that system. Measurements taken using the small White cell did not require the set of reference plots. Therefore, a vacuum curve, a sample curve, an etalon curve, and the zero level curve were used to obtain the data. This greatly simplified the analysis because a single plot could contain several sample measurements, all at different pressures.

The nature of the samples placed in the test cells were either the pure absorber gas or a fixed absorber pressure and a foreign gas, either nitrogen or helium. Only  $\text{CO}_2$  was examined using the large White cell, where sample pressures between 0.1 and 3 torr were used because of the long path length. The small White cell provided path lengths which allowed observation of spectral lines over a wide variety of pressures.

Pure absorbing gas samples were examined at pressures from 15 torr to 480 torr, as shown in Fig. 16. It was assumed in the analysis of the data that 60 torr was a Lorentzian line shape. This assumption fixed the absorption at line center to a definite value. A transmittance plot of a single spectral line should show constant absorption at line center for a Lorentz line shape.

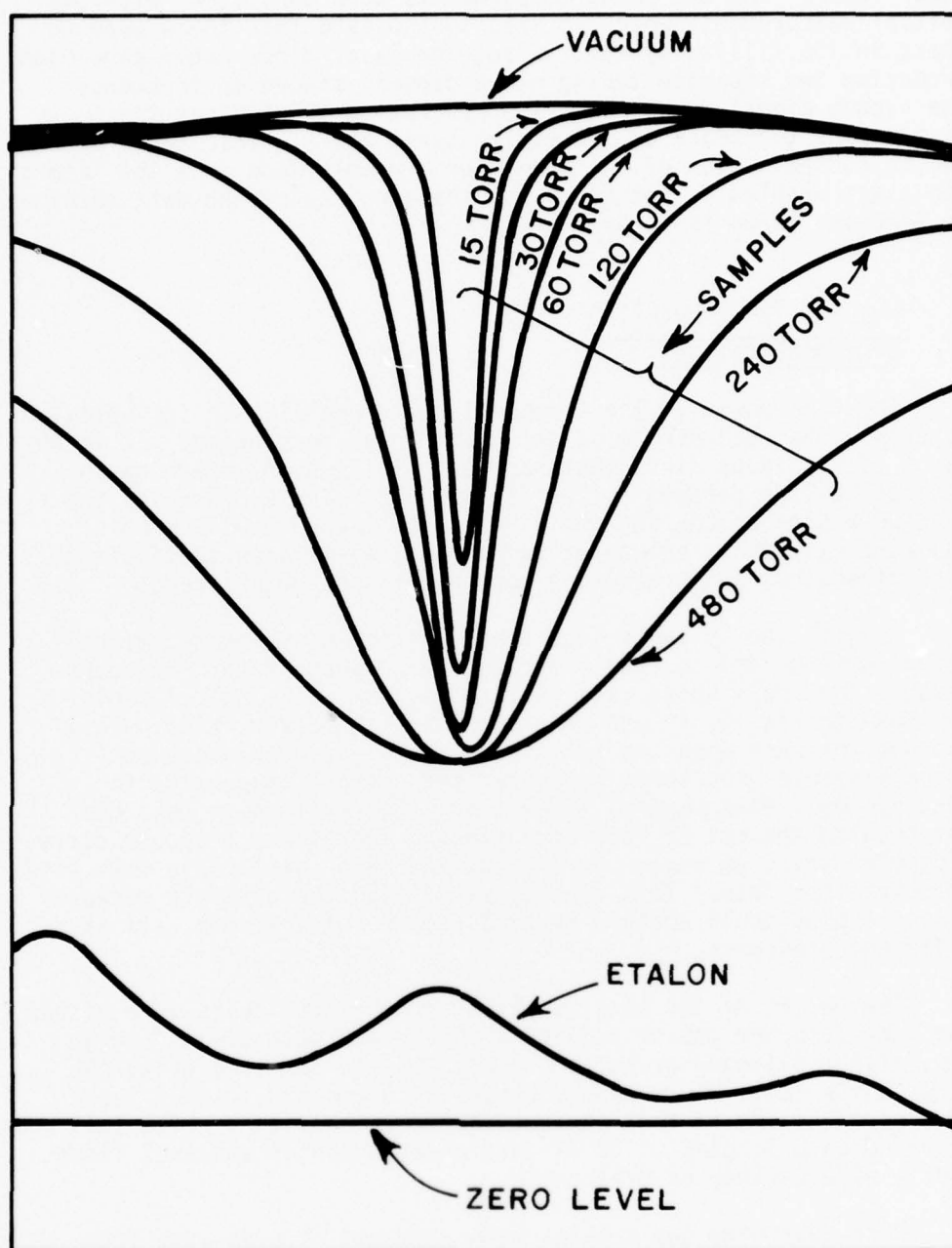


Fig. 16. Typical recorded data, pure absorber line shape.

The curves of Fig. 16 do not display this behavior due to wing effects from neighboring absorption lines. For  $(\gamma - \gamma_0) \gg \gamma_0$  and a Lorentz line shape, and differentiating  $j_L(\gamma - \gamma_0)$  (see Eq. (23)) with respect to  $\gamma$  one obtains:

$$(4) \quad \frac{dj_L(\gamma - \gamma_0)}{d\gamma} = - \frac{2\alpha_c}{\pi} \frac{1}{(\gamma - \gamma_0)^3} .$$

The change in the line shape for  $\gamma \gg \gamma_0$  over a neighboring spectral line is very small; basically, no distortion except for a uniform downward shift results from the wings. Thus, knowing where the pure Lorentz line shape begins and assuming that at this pressure the wing effects are negligible so that  $k(\gamma_0)$  can be determined, one is able to measure undistorted single line shape parameters. From Fig. 16 the 60 torr curve shows small wing absorption, supporting the above assumption.

Broadening effects were examined by choosing an absorber pressure, usually 60 torr, and then introducing the foreign gas, either nitrogen or helium. Figure 17 gives an example of such a plot. It is difficult to determine the wing effects of other lines in this case, however, because the wings did not exhibit large absorption for the pressures considered. The distortion was considered small and ignored.

The halfwidth of a spectral line is defined to be the half-width at half-intensity of the absorption coefficient. However, the analysis must be carried out on transmittance plots. The transmittance corresponding to one-half the absorption coefficient can be found from

$$(5) \quad T_{1/2} = e^{-\frac{1}{2} kx} = (e^{-kx})^{1/2} = \sqrt{T} .$$

Now the halfwidth can be measured from the transmittance plot.

The data taken from the transmittance plots include the partial pressures, the path length, the transmittance at line center, and the halfwidth of the spectral lines. Appendix A lists the essential data obtained from calculations involving the previously-mentioned quantities for Lorentz line shapes. The partial pressures of the absorbing and foreign gases are listed along with the corresponding halfwidths. The absorber amount and the line center absorption coefficient are also listed. For a Lorentz line, the line strength can be calculated from Eq. (42b)

$$(6) \quad S^{J'} = \pi k^2(\gamma_0) \alpha_c \cdot (\text{cm}^{-1}/\text{mol} (\text{cm}^{-2})) .$$



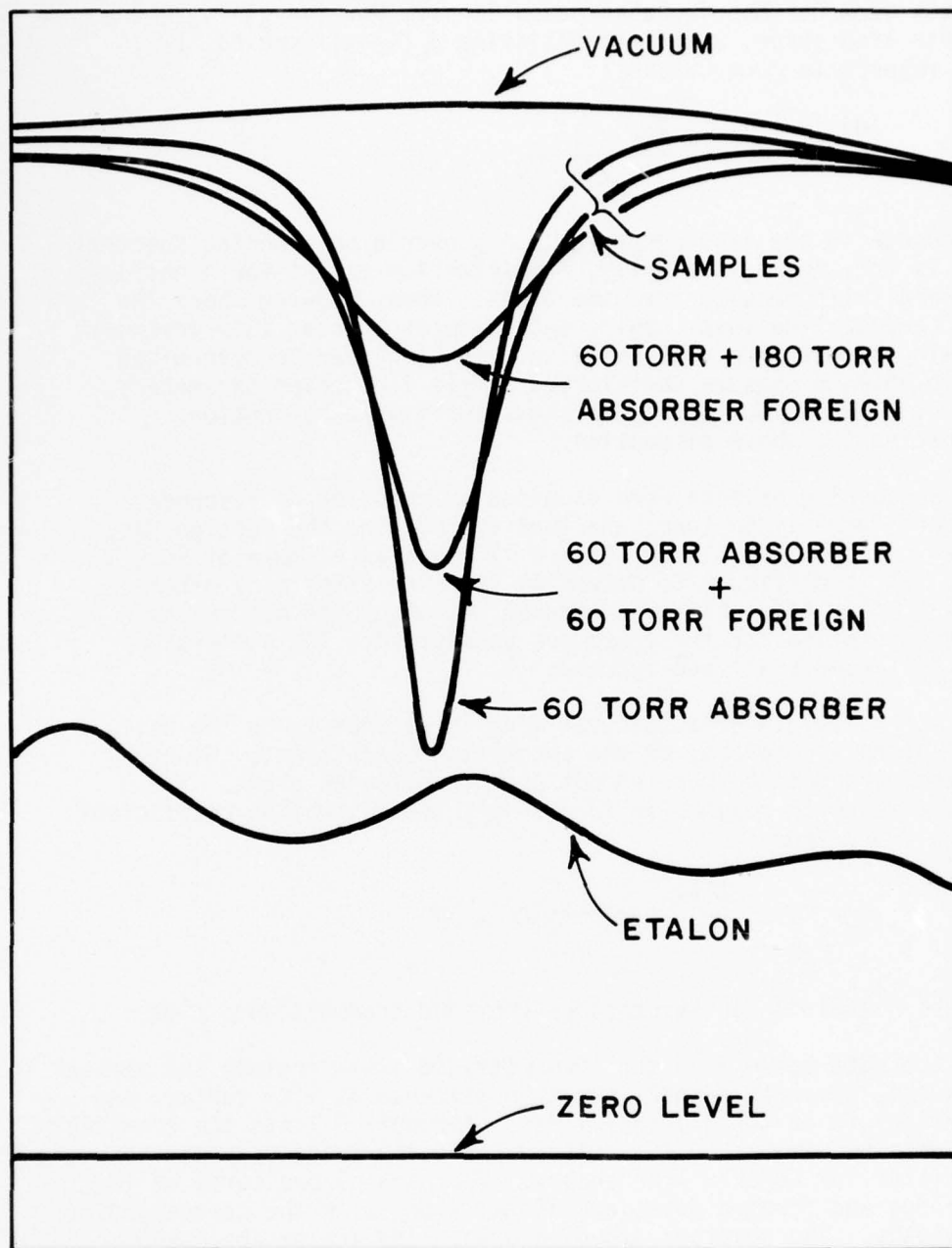


Fig. 17. Typical recorded data, foreign broadened line shape.

Appendix B lists results of the Voigt line shape measurements. No foreign broadening was examined in this regime, thus, only absorber pressures are listed. The halfwidth has two columns, one for measured values and one for calculated values. The technique in evaluating the calculated values used Eqs. (38) to (41) and the experimental value for  $\alpha_{CO}$ , Eq. (33) to determine  $\alpha_D$ , and a numerical technique to evaluate the integral [15]. Thus, solving  $k(\gamma_0 + \alpha_V) = \frac{1}{2} k(\gamma_0)$  produced the Voigt halfwidth,  $\alpha_V$ . The absorption coefficient and absorber amount were obtained in the same way as the Lorentz line shape tables of Appendix A.

Using the data in Appendix A and B, a plot of the halfwidth versus the pressure was made for both the  $CO_2$  and  $N_2O$  data (Figs. 18-31). The curves show the linear Lorentz region, the intermediate Voigt profile region, and the beginning of the Doppler region. It should be noted that the Voigt line halfwidth data in Appendix B show, in some cases, disagreement with the calculated values. The Voigt halfwidths are between 0.002 and 0.007  $cm^{-1}$  requiring small frequency scans, the FSR of the etalon is 0.0664. The ability to measure is obviously hindered by the comparatively large FSR of the etalon. Also, the Voigt region of the halfwidth versus pressure plot shows more scatter than the Lorentz which is consistent with the above.

A least squares curve fit of the form  $y = mx$  was used on the halfwidth versus pressure data in the Lorentz region. Improved numbers for the lines of a particular J-number were obtained. A second least squares fit of the form  $y = mx + b$  was carried out on the halfwidth versus J-number acquired from the first fit. Table 1 gives the results in the

form of  $\alpha_{CO} = \alpha_{CO} \frac{P_e}{P_{e0}} \left( \frac{T_0}{T} \right)^{1/2}$  with  $T = T_0$  and  $P_{e0} = 1 \text{ atm}$  ( $T_0 = 296 \text{ K}$ ).

Since  $p_f = 0$  for pure absorber measurements, the equation can be written

$$(7) \quad \alpha_c = \alpha_{CO} B p_a \quad .$$

Figures 32 and 33 are plots of  $\alpha_{CO}$  versus the J-number where for  $CO_2$ ,  $B = 1.3$ , and for  $N_2O$ ,  $B = 1.24$ . The values chosen for the self-broadening coefficient,  $B$ , are empirical values [16]. The plots make a comparison with McClatchey [18].

Calculations of the self-broadening coefficients and the foreign-broadening coefficients for individual absorption lines were made using Eq. (31) of Appendix C. Again, consider the

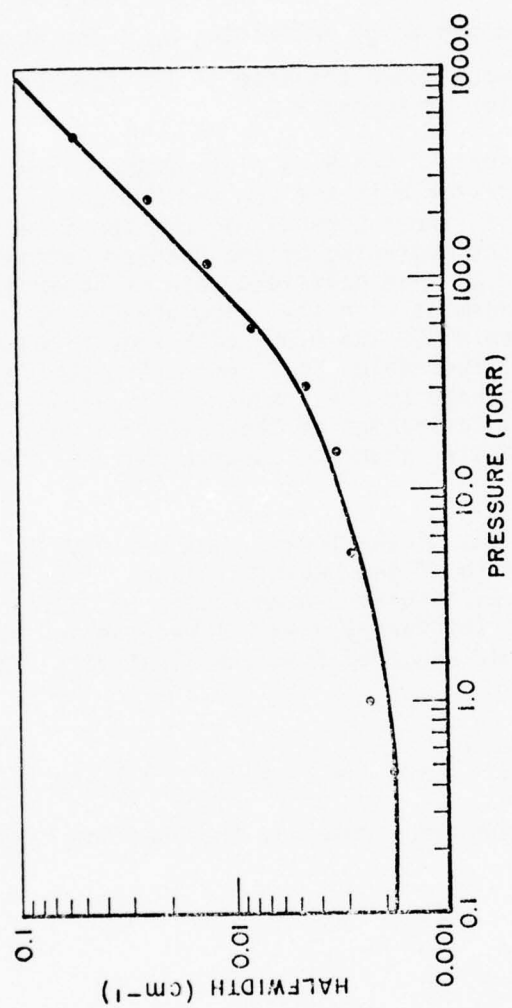


Fig. 18. Halfwidth versus pressure, CO<sub>2</sub> 11'0-00°0 R(24).

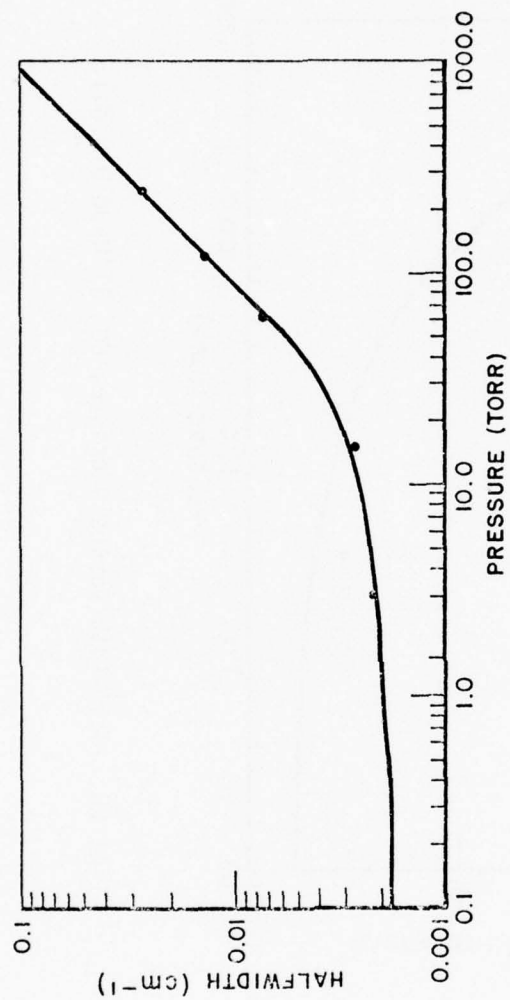


Fig. 19. Halfwidth versus pressure, CO<sub>2</sub> 11'0-00°0 R(28).



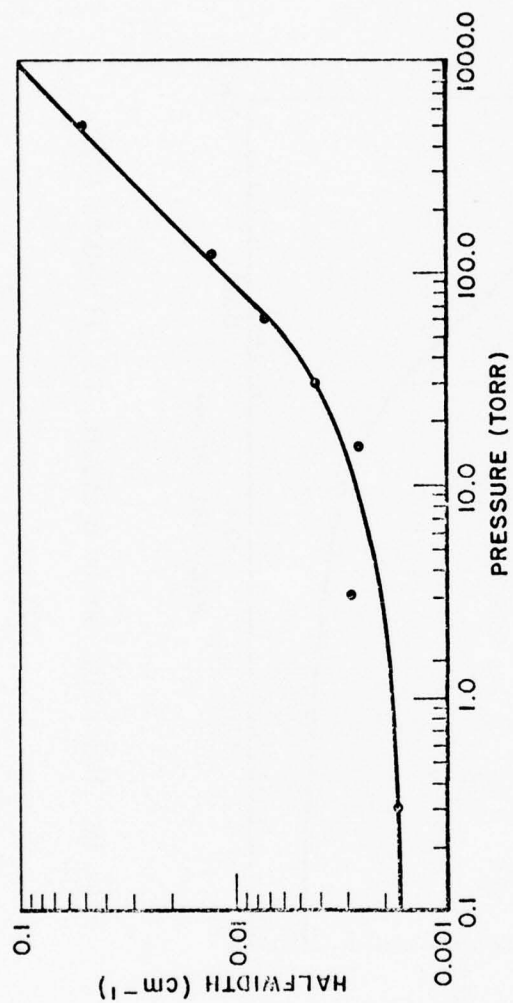


Fig. 20. Halfwidth versus pressure, CO<sub>2</sub> 11'0-00°0 R(30).

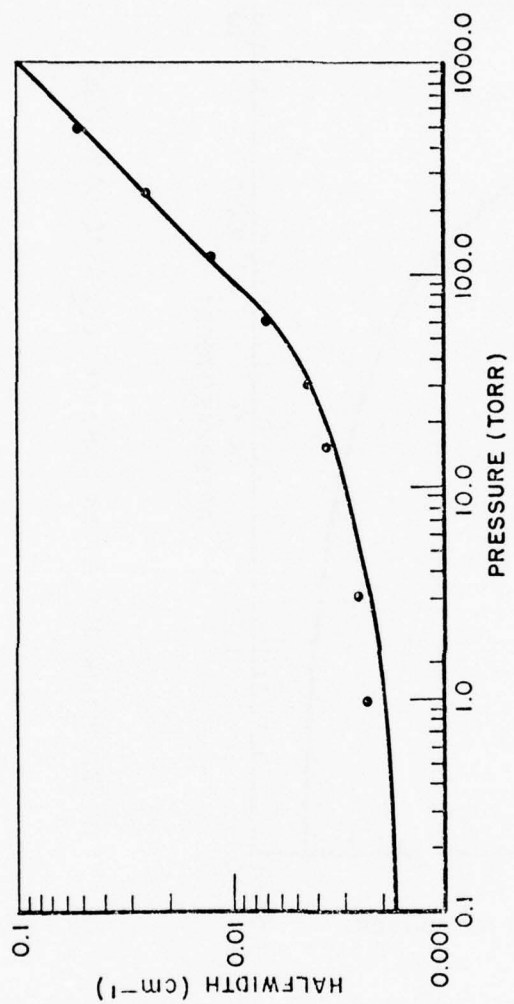


Fig. 21. Halfwidth versus pressure, CO<sub>2</sub> 11'0-00°0 R(34).

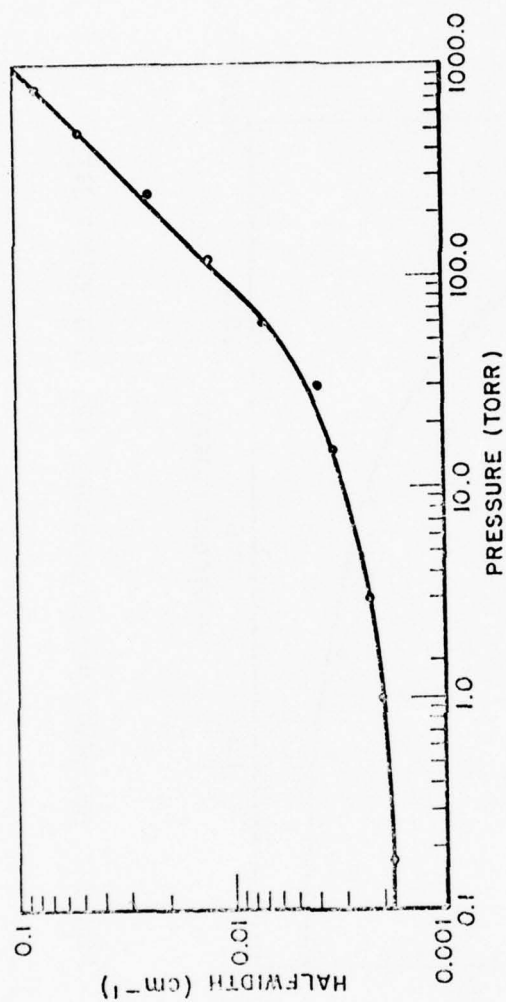


Fig. 22. Halfwidth versus pressure, CO<sub>2</sub> 11'0-00°0 R(36).

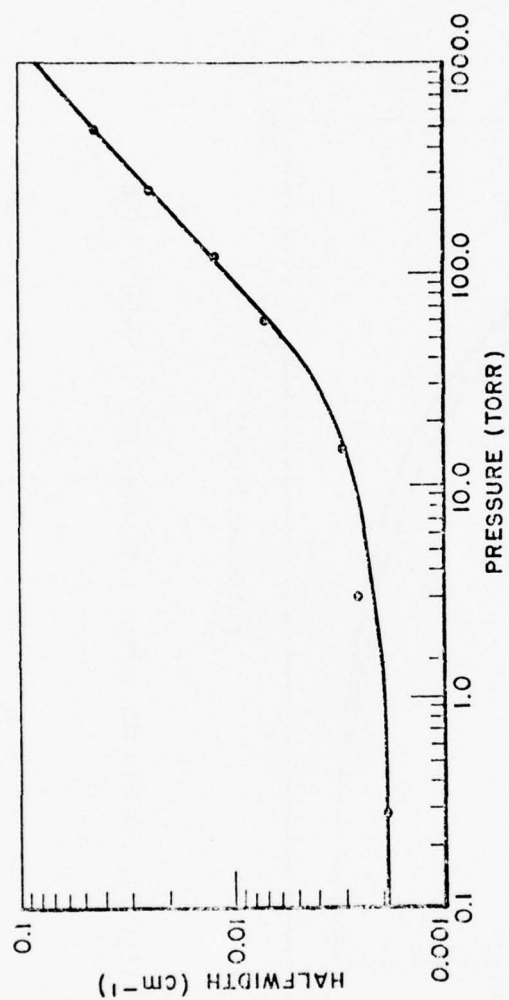


Fig. 23. Halfwidth versus pressure, CO<sub>2</sub> 11'0-00'0 R(46).



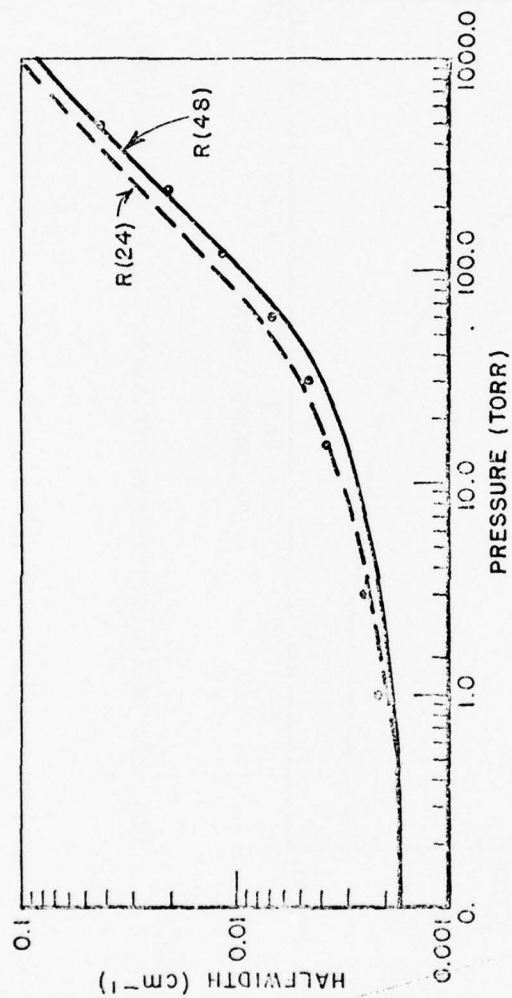


Fig. 24. Halfwidth versus pressure, CO<sub>2</sub> 11'0-00'0 R(48).

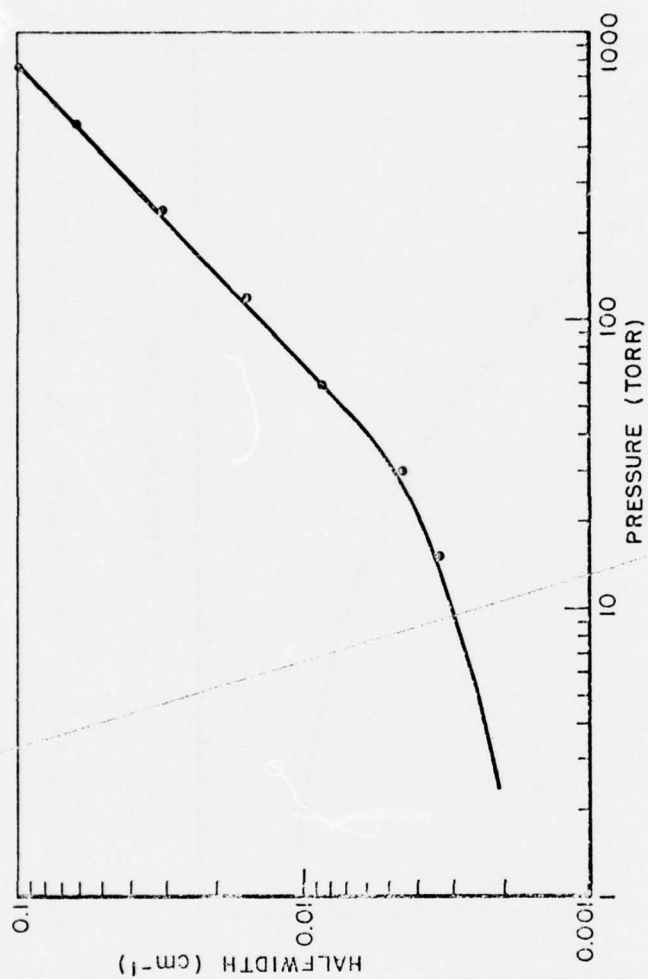


Fig. 25. Halfwidth versus pressure, N<sub>2</sub>O 20°C-01'0 P(12).

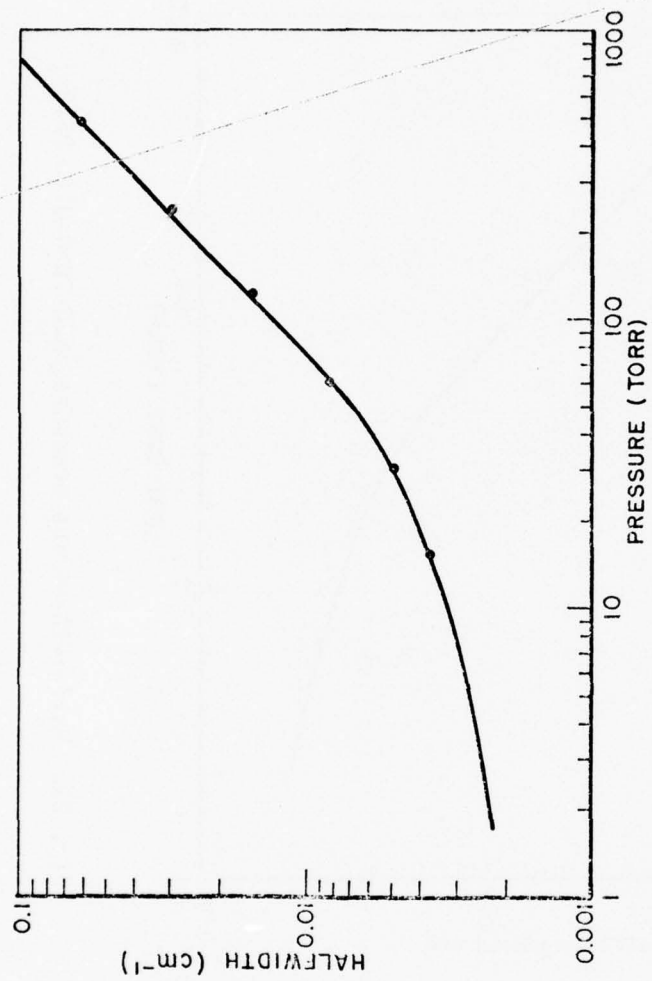


Fig. 26. Halfwidth versus pressure, N<sub>2</sub>O 20°C-0.1° P(13).

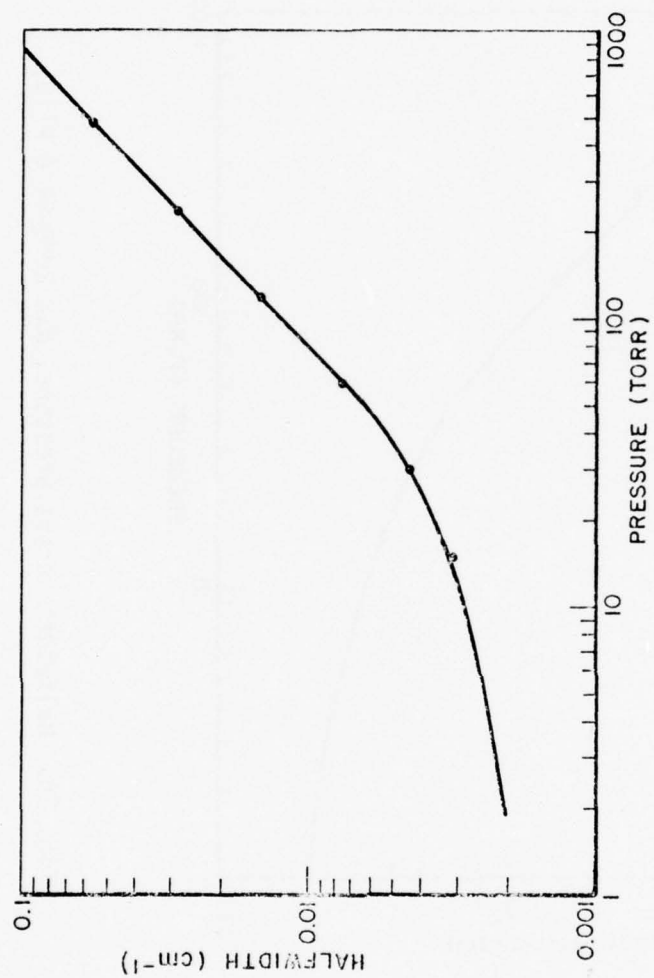


Fig. 27. Halfwidth versus pressure, N<sub>2</sub>O 20°C-0.01'0 P(16).

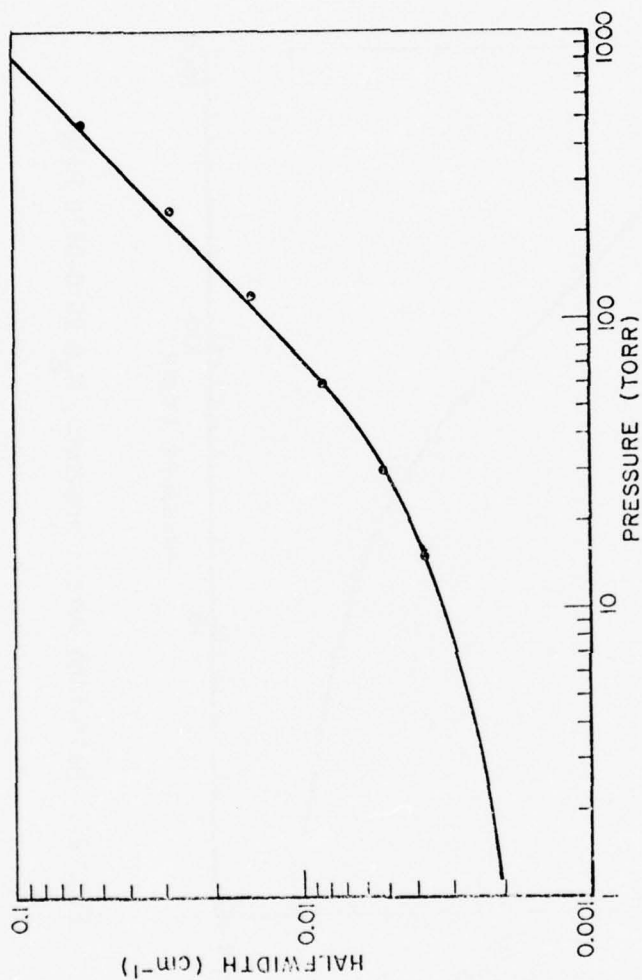


Fig. 28. Halfwidth versus pressure, N<sub>2</sub>O 20°C-01'0 P(19).



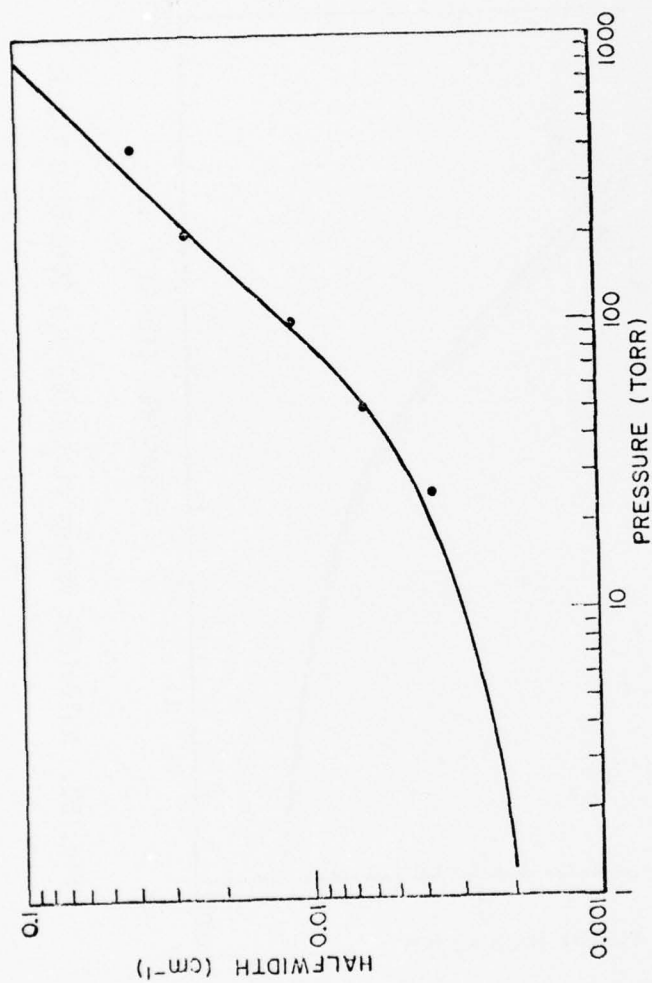


Fig. 29. Halfwidth versus pressure, N<sub>2</sub>O 20°0-01'0 P(21).

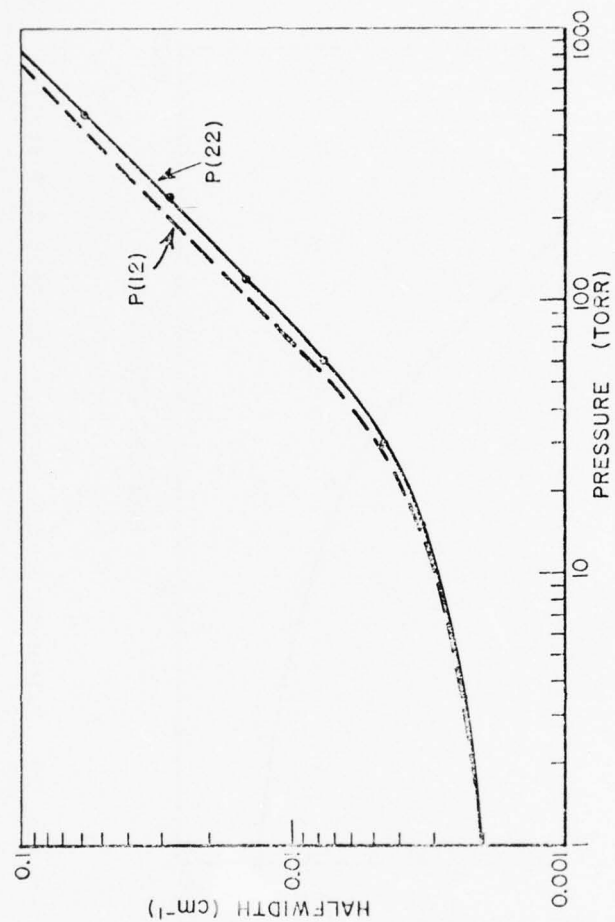


Fig. 30. Halfwidth versus pressure, N<sub>2</sub>O 20°0-01'0 P(22).

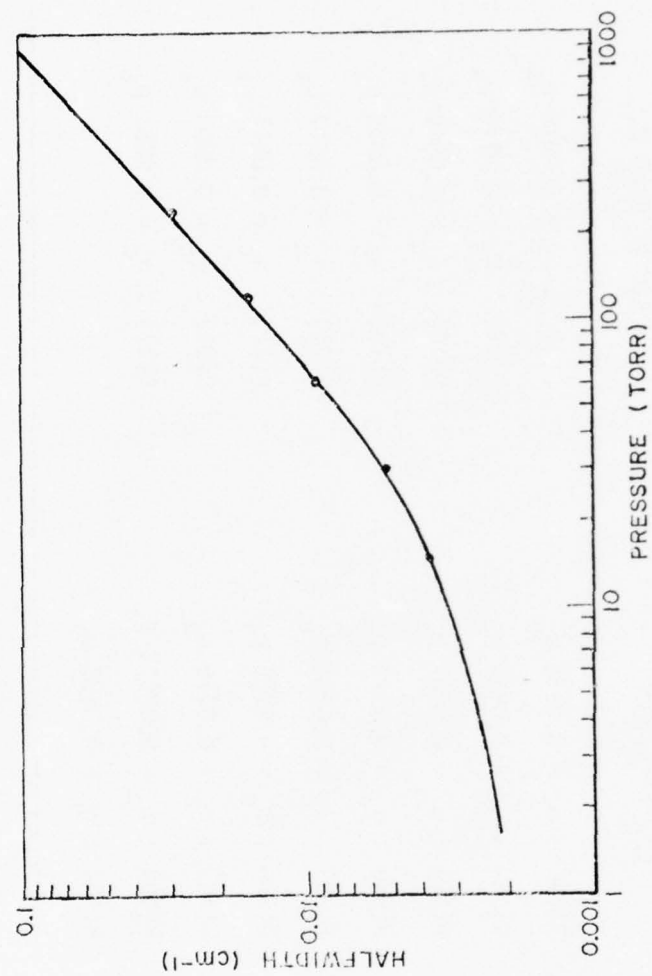


Fig. 31. Halfwidth versus pressure, N<sub>2</sub>O 20°C-0.1° P(27).

Table 1.  $\alpha_c = (\alpha_{CO} B) p_a$

$CO_2$ 11'0-00'0	$N_2O$ 20'0-01'0
R(24) : $\alpha_c = 0.0838 p_a$	P(12) : $\alpha_c = 0.0970 p_a$
R(28) : $\alpha_c = 0.0814 p_a$	P(13) : $\alpha_c = 0.0964 p_a$
R(30) : $\alpha_c = 0.0802 p_a$	P(16) : $\alpha_c = 0.0946 p_a$
R(34) : $\alpha_c = 0.0779 p_a$	P(19) : $\alpha_c = 0.0929 p_a$
R(36) : $\alpha_c = 0.0767 p_a$	P(21) : $\alpha_c = 0.0917 p_a$
R(38) : $\alpha_c = 0.0755 p_a$	P(22) : $\alpha_c = 0.0911 p_a$
R(44) : $\alpha_c = 0.0719 p_a$	P(23) : $\alpha_c = 0.0905 p_a$
R(46) : $\alpha_c = 0.07071 p_a$	P(27) : $\alpha_c = 0.0881 p_a$
R(48) : $\alpha_c = 0.0695 p_a$	

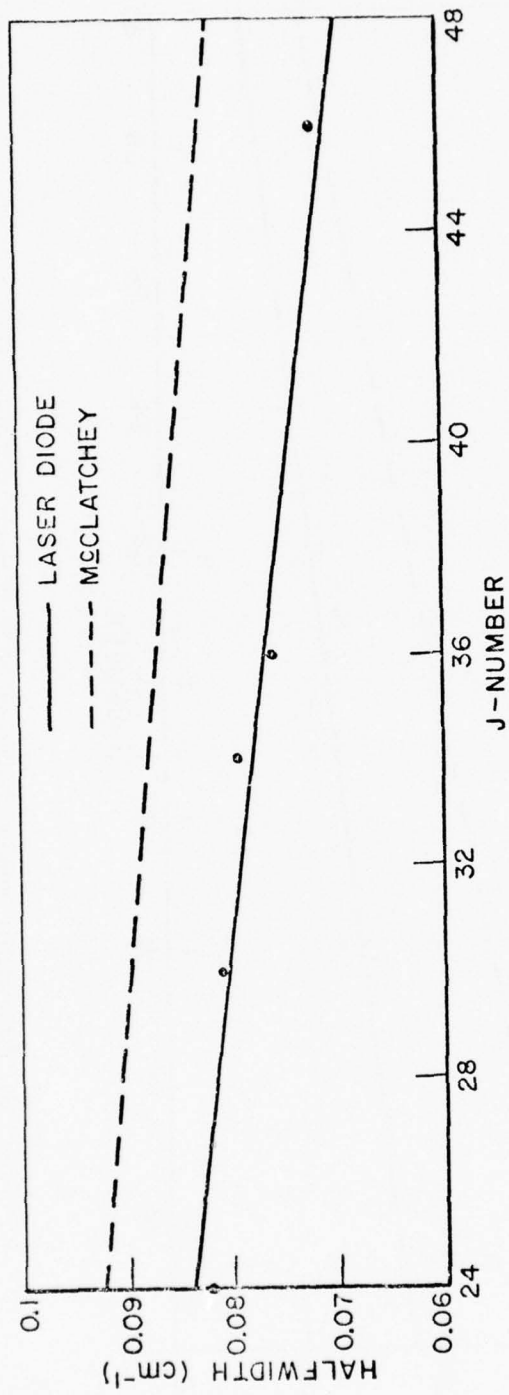


Fig. 32. Halfwidth versus J-number, CO<sub>2</sub> 11'0-00°0 R-Branch.



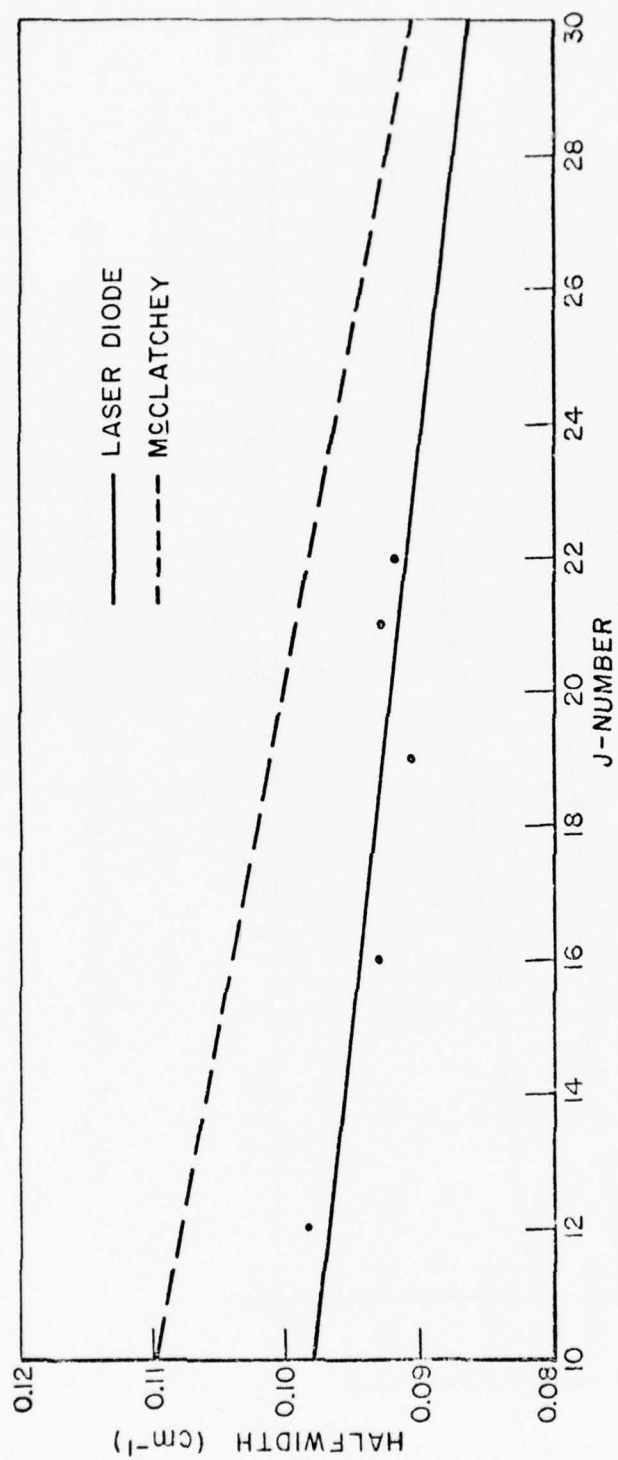


Fig. 33. Halfwidth versus J-number,  $N_2O$  20°0-01'0 P-Branch.

equation for  $T = T_0$  and  $P_{e0} = 1$  atm; then two separate measurements of a broadened spectral line give two equations and three unknowns. However, for the nitrogen broadened case,  $F$  is defined to be 1, which makes the problem tractable. Solving for  $B$ , one obtains

$$(8) \quad B = \frac{p_{f1} - \beta p_{f2}}{\beta p_{a2} - p_{a1}}$$

$$\text{where} \quad \beta = \frac{\alpha_{c1}}{\alpha_{c2}}$$

Precise measurements of  $B$  require accurate and stable values of the halfwidth. Unfortunately this level of accuracy and stability was not attained in this study; the values determined are, however, worth listing. Tables 2 and 3 list the self-broadening coefficients of the particular spectral lines and the partial pressures of the separate measurements used in the calculation.

Knowing  $B$ , the foreign-broadening coefficient can then be determined. In this case it is for helium broadening. The equation for  $F$  becomes:

$$(9) \quad F = B \left[ \frac{\beta p_{a2} - p_{a1}}{p_{f1} - \beta p_{f2}} \right] .$$

Again stable measurements are required for good results. Tables 4 and 5 list the foreign-broadening coefficients where the empirical values of  $B$  are used.

As shown in Appendix C, the line strength is not a function of pressure; thus, using the Lorentz line shape data an accurate value may be obtained for all line shapes. Using Eq. (6) and the smoothed halfwidth results, plots of the line strength versus  $J$ -number were made. Figures 34 and 36 show these results for  $CO_2$  and  $N_2O$ , respectively. The  $CO_2$  line strengths measured differ from the values of McClatchey in an interesting manner. The separation of the two curves is largest at the band center and then decreases as  $J$  becomes larger or smaller. This suggests that the distortions generated by the wings of neighboring lines was not accounted for in the McClatchey data. This could also partially account for the relatively large disagreement between the two curves. The agreement of the relative magnitudes is better in the  $N_2O$  case; however, the laser diode measured values indicate the band center to be around  $P(16)$  and  $P(17)$  rather than  $P(14)$  and  $P(15)$ .

To test the values of the line strength another approach was taken, based on Eq. (19) of Appendix C. The transmission plot was converted to an absorption plot and then a numerical integration

Table 2. CO<sub>2</sub> 11'0-00°0  
(Self-Broadening Coefficient)

Partial Pressures				Self- Broadening Coefficient (B)
Measurement 1		Measurement 2		
Pure (torr)	Nitrogen (torr)	Pure (torr)	Nitrogen (torr)	
Line ID: R(24)				
60.0	0.0	60.0	60.0	1.172
60.0	60.0	60.0	180.0	1.808
Line ID: R(28)				
60.0	0.0	60.0	60.0	1.578
Line ID: R(30)				
60.0	0.0	60.0	72.0	1.285
60.0	72.0	60.0	180.0	1.146
Line ID: R(34)				
60.0	0.0	60.0	60.0	1.451
60.0	60.0	60.0	180.0	1.083
Line ID: R(36)				
60.0	0.0	60.0	60.0	1.169
60.0	60.0	60.0	180.0	.855
Line ID: R(46)				
60.0	0.0	60.0	60.0	1.321

Table 3. N<sub>2</sub>O 20°0-01'0  
(Self-Broadening Coefficient)

Partial Pressures				Self- Broadening Coefficient (B)
Measurement 1		Measurement 2		
Pure Nitrogen (torr)	Pure Nitrogen (torr)	Pure Nitrogen (torr)	Pure Nitrogen (torr)	
Lind ID: P(12)				
60.0	0.0	60.0	60.0	1.294
60.0	60.0	60.0	180.0	.813
Line ID: P(13)				
60.0	0.0	60.0	60.0	1.560
60.0	60.0	60.0	180.0	1.372
Line ID: P(16)				
60.0	0.0	60.0	60.0	1.344
60.0	60.0	60.0	180.0	1.336
Line ID: P(19)				
60.0	0.0	60.0	60.0	1.245
60.0	60.0	60.0	180.0	1.323
Line ID: P(21)				
50.0	0.0	50.0	50.0	1.404
50.0	50.0	50.0	150.0	.904
Line ID: P(23)				
60.0	0.0	60.0	87.0	1.509
60.0	87.0	60.0	180.0	1.408
Line ID: P(27)				
60.0	0.0	60.0	60.0	1.941
60.0	60.0	60.0	180.0	.886

Table 4. CO<sub>2</sub> 11'0-00°0

(Helium Broadened Line)

Partial Pressures					Broadening Coefficient (F)
Measurement 1		Measurement 2			
Pure (torr)	Foreign (torr)	Pure (torr)	Foreign (torr)		
Line ID: R(24)					
60.0	0.0	60.0	60.0	.742	
60.0	60.0	60.0	180.0	1.040	
Line ID: R(28)					
60.0	0.0	60.0	72.0	.805	
60.0	72.0	60.0	180.0	.784	
Line ID: R(30)					
60.0	0.0	60.0	60.0	.841	
60.0	60.0	60.0	180.0	.873	
Line ID: R(34)					
60.0	0.0	60.0	60.0	.747	
60.0	60.0	60.0	180.0	.676	
Line ID: R(36)					
60.0	0.0	60.0	60.0	.838	
60.0	60.0	60.0	180.0	.815	
Line ID: R(44)					
60.0	0.0	60.0	60.0	.677	
60.0	60.0	60.0	180.0	2.400	
Line ID: R(46)					
60.0	0.0	60.0	60.0	.728	



Table 5. N<sub>2</sub>O 20°0-01'0

(Helium Broadened Line)

Partial Pressures					Broadening Coefficient (F)
Measurement 1		Measurement 2			
Pure (torr)	Foreign (torr)	Pure (torr)	Foreign (torr)		
Line ID: P(12)					
60.0	0.0	60.0	60.0	.723	
60.0	60.0	60.0	180.0	.633	
Line ID: P(13)					
60.0	0.0	60.0	60.0	.636	
60.0	60.0	60.0	180.0	.711	
Line ID: P(16)					
60.0	0.0	60.0	60.0	.741	
60.0	60.0	60.0	180.0	.890	
Line ID: P(19)					
60.0	0.0	60.0	60.0	.651	
60.0	60.0	60.0	180.0	.617	
Line ID: P(21)					
25.0	25.0	25.0	75.0	.690	
Line ID: P(23)					
60.0	0.0	60.0	60.0	.784	
60.0	60.0	60.0	180.0	.899	
Line ID: P(27)					
60.0	0.0	60.0	60.0	.602	
60.0	60.0	60.0	180.0	1.052	

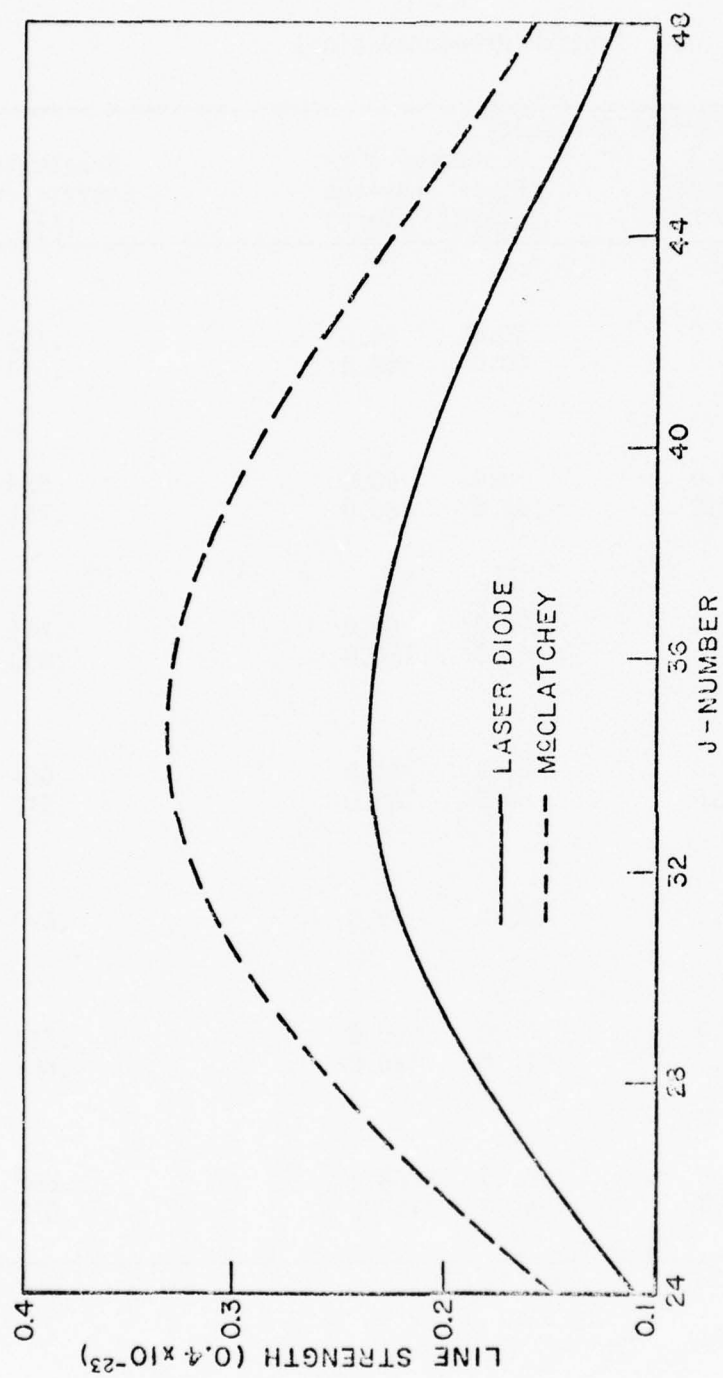


Fig. 34. Line strength versus J-number,  $\text{CO}_2$  11'0-00'0 R-Branch.

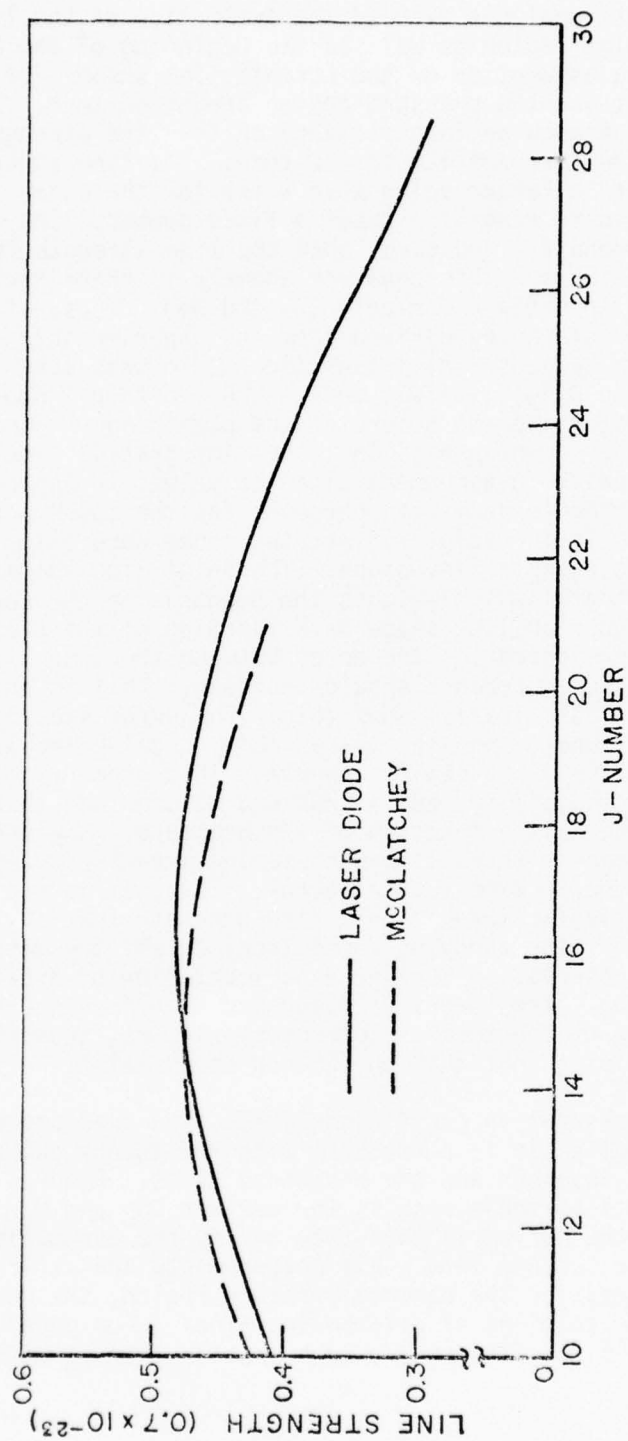


Fig. 35. Line strength versus J-number,  $N_2O$  20°0-01'0 P-Branch.

was performed. This analysis allowed the evaluation of the line strength in the Voigt region as well as the beginning of the Lorentz region, without the assumption of the Lorentz line shape. Of particular interest was the pressure region around 60 torr. The tables of Appendix A show an inconsistency in the line strength for the values at 60 torr and 120 to 480 torr. The line strength for 60 torr exhibits a larger value than those for the other pressures which tend to stabilize about a fixed number. The theory as discussed in Appendix C indicates that the line strength is not a function of the pressure. This observed anomaly is characteristic of all the data in Appendix A for both  $\text{CO}_2$  and  $\text{N}_2\text{O}$ . Thus, it was hoped that the line strengths derived from the experimental transmittance plots by numerical integration would shed some light on the problem. The R(34) line was chosen and additional pressures were measured to determine the nature of the phenomenon. Results of this analysis are shown in Fig. 36. The "integrated" line strengths are basically in agreement with the values in Appendix A with a continued trend to vary with pressure for the lower pressures. To test the results in the Voigt regime, the lines were also analyzed assuming a Lorentz line shape. The Voigt line shape is expressed as an integral which weights the emphasis on the Lorentz line shape or the Doppler line shape as a function of the pressure. Thus, as the pressure decreases the error between the true line strength and the assumed Lorentz should increase. This is observed in the data and Fig. 37 clearly shows this. The error stabilizes at less than 2 torr where the line is basically Doppler and at 60 torr where the line is basically Lorentz. This property of the data gives it credibility, and allows one to conclude that the true line strength is a function of the pressure. However, this statement must be made with caution because the amount of variation observed could be due to experimental error. Thus, it is not the nature of this particular transition's line strength that is emphasized but rather the annoying consistency of all the data. To establish this observation further experimentation of greater accuracy is required. The theory as discussed in Appendix C is a zero order solution of the total spectroscopy picture, thus it would not be surprising that this phenomenon could exist.

Finally, the absorption coefficient versus the pressure was examined. The results are in accordance with the theory and are given for the pure absorber and the broadened cases. Figures 38 through 40 are plots of these results for certain  $\text{CO}_2$  and  $\text{N}_2\text{O}$  lines. The importance of the curves is that they verify the assumption that 60 torr is indeed a Lorentz line. All measurements are at line center and in ( $\text{km}^{-1}$ ). Thus, for the Lorentz pressure region, the observed sloping line is due to wings of neighboring lines. For pure absorber gas and a fixed frequency  $\gamma$  much greater than  $\gamma_0$  we have

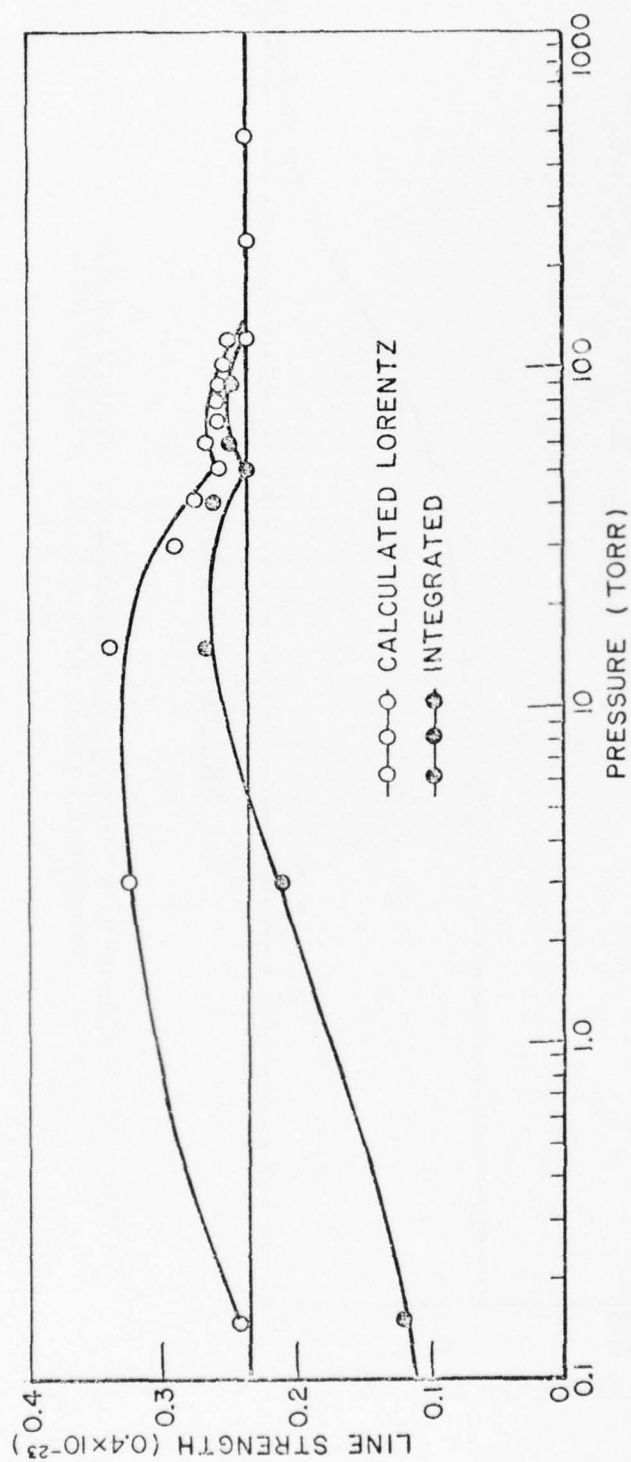


Fig. 36. Line strength versus pressure,  $\text{CO}_2$  11°0-00°0 R(34).



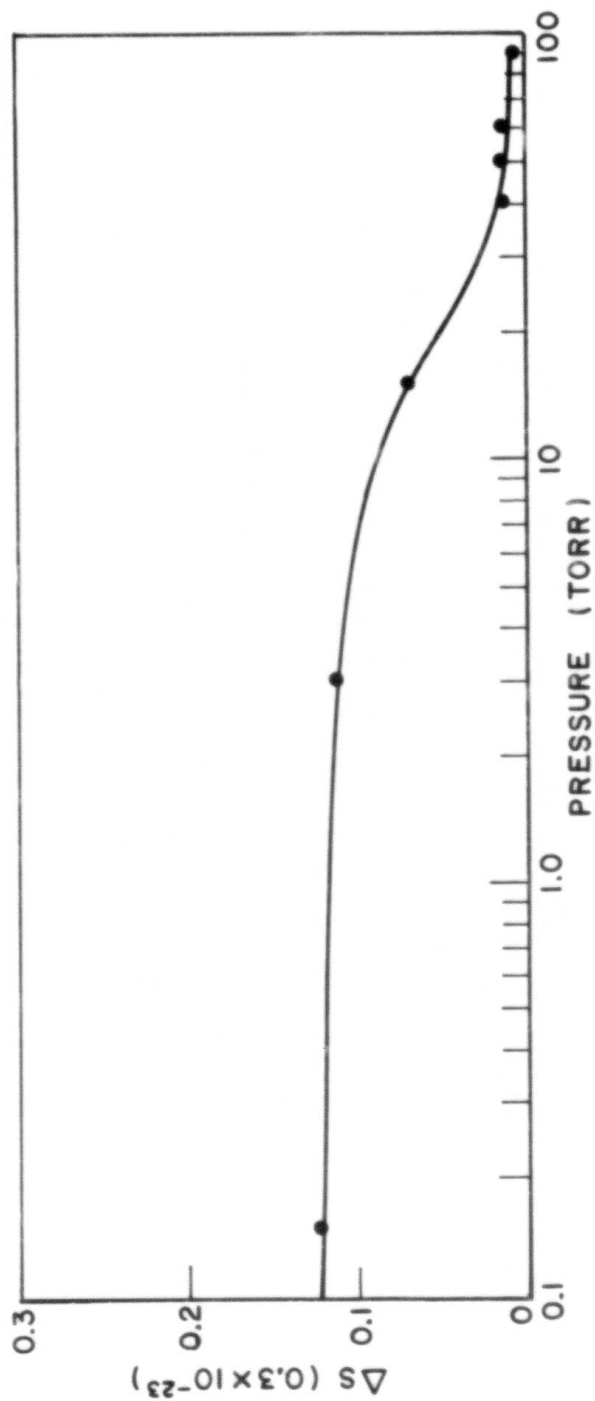


Fig. 37. Difference in line strength measurements (assumed Lorentz minus "integrated") versus pressure,  $\text{CO}_2$  11'0-00°0 R(34).

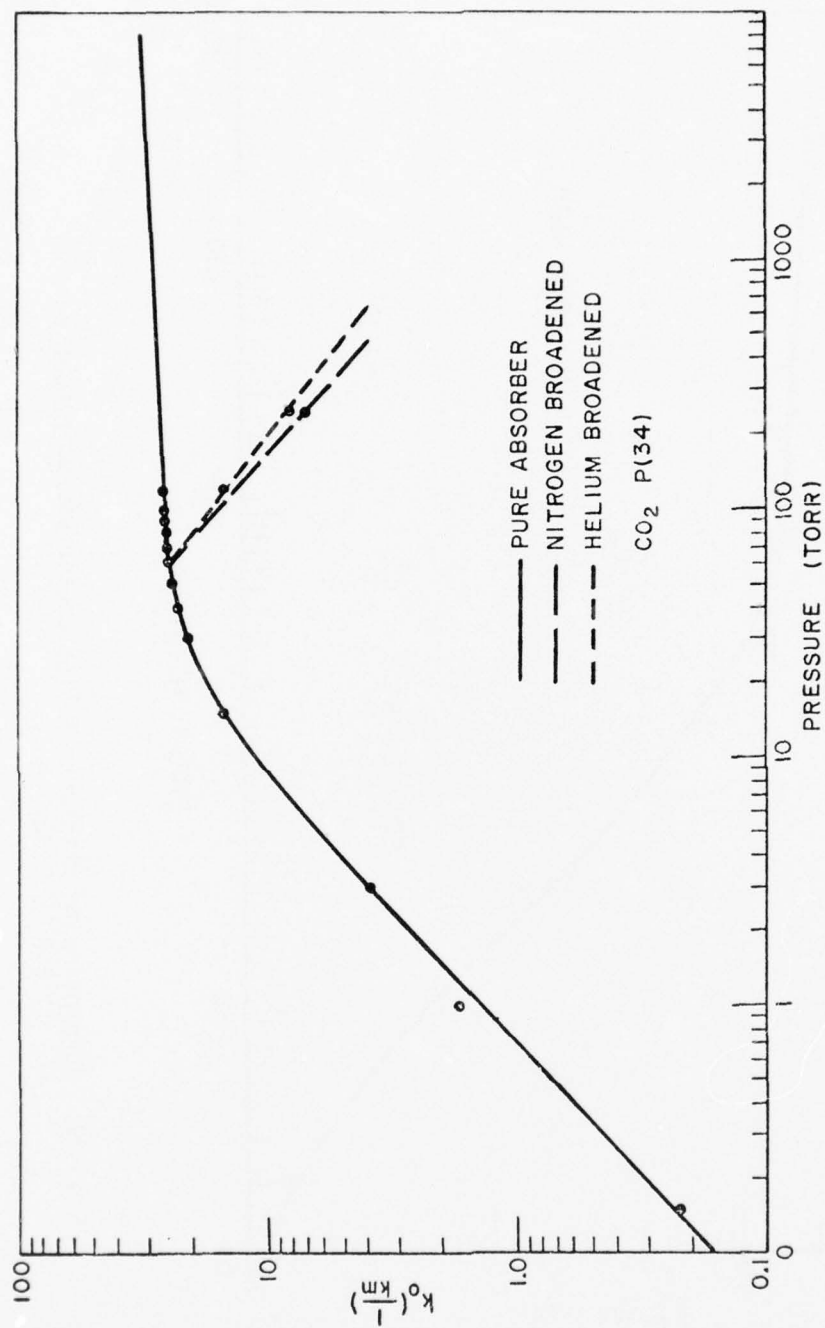


Fig. 38. Absorption coefficient at line center versus pressure, CO<sub>2</sub> 11'0-00'0 R(34).

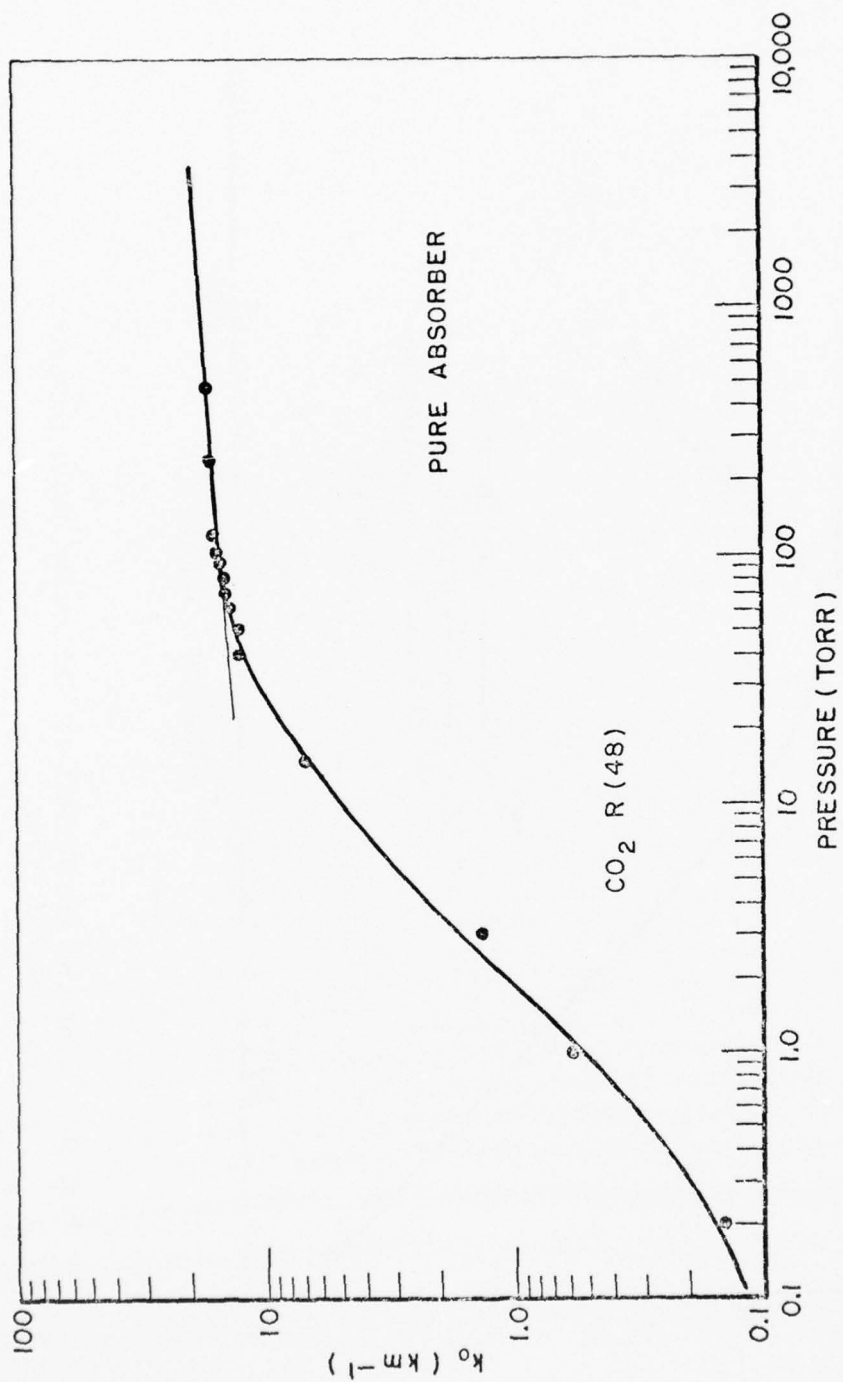


Fig. 39. Absorption coefficient at line center versus pressure,  $\text{CO}_2$  11'0-00'0 R(48).

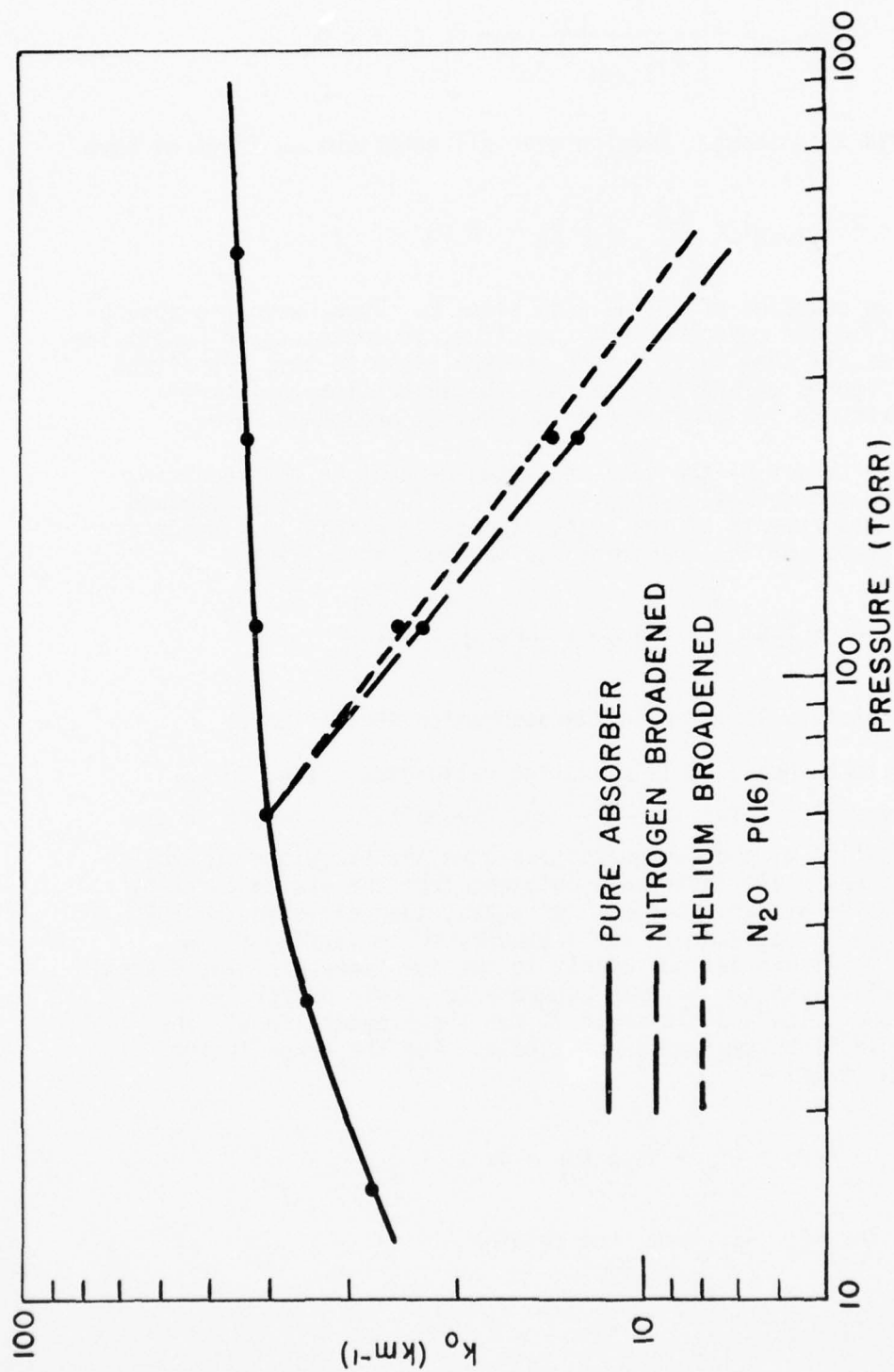


Fig. 40. Absorption coefficient at line center versus pressure,  $N_2O \quad 20^\circ C - 0.1 \text{ torr } P(16)$ .

$$(10) \quad k(\gamma_{\text{fixed}}) = \left[ \frac{S^J \alpha_{\text{co}}}{(\gamma_{\text{fixed}} - \gamma_0)^2} B \right] p_a = C p_a$$

where C is a constant. Summing over all contributing lines we have

$$(11) \quad k(\gamma_{\text{fixed}}) = \left( \sum_i C_i \right) p_a = \varnothing p_a \quad .$$

This is an equation of a line with slope  $\varnothing$ . Thus, when the absorption coefficient deviates from this line, it ceases to be Lorentzian. The curves all show that 60 torr is very close to this transition point. Figures 38 and 40 also show the absorption coefficient versus pressure for the nitrogen and helium broadened cases.

The accuracy of the data presented depends on the measuring techniques and overall system stability. The stability attained allowed measurements of the transmittance to within 1%. Since a typical value for the transmittance was 50%, using [16]

$$(12) \quad \frac{\Delta k}{k} = \frac{\Delta T/T}{\delta n T} \left[ 1 - \frac{1}{2} \frac{\Delta T}{T} + \frac{1}{3} \left( \frac{\Delta T}{T} \right)^2 \dots \right]$$

corresponds to a 1% error in the absorption coefficient.

The technique used in measuring halfwidths called for a frequency scale factor in  $\frac{(\text{cm})^{-1}}{\text{cm}}$  and the halfwidth length in cm. Multiplication of the two quantities gave the halfwidth in  $(\text{cm})^{-1}$ . The frequency scale factor was obtained from the etalon curve by measuring the distance between two peaks, then dividing the FSR (p. 12) by that distance. The frequency scale factor,  $f_s$ , was accurate to within 4%, due mainly to the low finesse of the etalon. The halfwidth length,  $\alpha_L$ , was accurate to within 5% for lines 60 torr and below and closer to 2% for the broader lines. The 5% value shall be kept as a worst case. For the error in the halfwidth, examine

$$(13) \quad \alpha + \Delta\alpha = (f_s + \Delta f_s) (\alpha_L + \Delta\alpha_L) \quad .$$

Ignoring the  $\Delta f_s \Delta\alpha_L$  term, one obtains

$$(14) \quad \frac{\Delta\alpha}{\alpha} = \frac{\Delta f_s}{f_s} + \frac{\Delta\alpha_L}{\alpha_L} \quad .$$



Therefore, the halfwidths are accurate to within 9%. The least squares curve fit analysis performed on the data should provide better numbers for the halfwidths in the Lorentz line shape region.

The values of line strengths as listed in Appendix A have a maximum error of 10% as seen from

$$(15) \quad S^{J'} + S^{J''} = \pi(k' + \Delta k') (\alpha_c + \Delta \alpha_c)$$

and

$$(16) \quad \frac{\Delta S^{J'}}{S^{J'}} = \frac{\Delta k'}{k'} + \frac{\Delta \alpha_c}{\alpha_c} .$$

No significant error is induced in converting between  $k$  in  $(\text{km}^{-1})$  and  $k'$  in  $(\text{mol (cm}^{-2})^{-1})$ .

## CHAPTER 4

### CONCLUSIONS

Successful simulation of CO laser transitions using a PbSSe tunable semiconductor laser was achieved. Transmittance measurements in a H<sub>2</sub>O-N<sub>2</sub> mixture were then carried out for the 6-5 P(10) and P(14) lines using a White-type absorption cell with a path length of 0.732 km. Good agreement with previous measurements was attained verifying the technique used.

Improvement over the AFCRL tabulation [18] listing of Lorentz line shape parameters was obtained for the 11'0-00°0 R-Branch of CO<sub>2</sub> and the 20°0-01'0 P-Branch of N<sub>2</sub>O. An accuracy of 10% for measurements above 15 torr was attained for these parameters using the PbSSe laser diode. Values of the self-broadening coefficient and the foreign broadening coefficient for helium were calculated from the Lorentz line shape data (Appendix A). Also pressures in the Voigt profile region were examined for the vibrational bands of CO<sub>2</sub> and N<sub>2</sub>O mentioned. The accuracy and stability of the broadening coefficients and the Voigt line shape data are in general not of the same quality as the Lorentz line shape data.

The measuring techniques used in this experiment do not fully realize the resolving power of the laser diode. Higher accuracy of the data is definitely possible. Improved measuring capabilities will be attained when a direct computer analysis of the raw data is used. The hardware for such a system has been developed here at Ohio State. A computer controlled data acquisition system can realize greater stability by using two channels, one for the signal and one for the reference, to simultaneously monitor fluctuations induced in the separate beams. A flat background can thus be attained which would assist measurements of the frequency scale factor and halfwidth length. Also, improved techniques of measuring the frequency scale factor and halfwidth length can be accomplished.

Such improvements could lead to an examination of the self-broadening coefficient as a function of J-number. Useful results of the line strength as a function of pressure could be attained by numerically integrating the absorption coefficient with respect to frequency.

## REFERENCES

1. Letokhov, V. S., "Non-Linear High Resolution Laser Spectroscopy," *Science*, 190, 344 (1975).
2. Nill, K. W., "Infrared Spectroscopy of CO Using a Tunable PbS<sub>2</sub> Diode Laser," *Appl. Phys. Letts.*, 19 (79) 1971.
3. Hinkley, E. D., "Tunable Infra-red Lasers and Their Applications to Air Pollution Measurements," *Opto-electronics*, 4 (1972), 69-86.
4. McNamara, F. L., "A Tunable Semiconductor Laser for Pollution Studies," *Optical Engineering*, 11, No. 1 (1972), p. 9.
5. Blum, F. A., et al., "Measurements of the Gain Line Shape of a Gas Laser Using a Tunable Semiconductor Laser," *Appl. Phys. Lett.*, Vol. 20, No. 10, 15 May 1972.
6. Blum, F. A., et al., "Observation of Nuclear Hyperfine Splitting in the Infrared Vibration-Rotation Absorption Spectrum of the NO Molecule," *Chemical Physics Letters*, 15, 1, p. 144, 1972.
7. Nill, K. W., "Broad-Band IR Spectroscopy with CW Pb<sub>0.88</sub>Sn<sub>0.12</sub>Te Double-Heterostructure Laser," *IEEE, JQE QE10* (9) 792, 1974.
8. Eng, R. S., et al., "Tunable Laser Measurements of Water Vapor Transitions in the Vicinity of 5  $\mu$ m," *Chemical Physics Letters*, 19, 524 (1973); "Diode Laser Measurement of Water-Vapor Absorption Line Parameter," *Mole. Phys.*, 28, 653 (1974).
9. Blum, F. A., et al., "Line Shape of the Doppler-Limited Infrared Magnetic Rotation Spectrum of Nitric Oxide," *Journal of Chemical Physics*, 58, (4968), (1973).
10. Butler, J. F., "Pb-Salt Tunable Diode Laser," *Proceedings of the First European Electro-Optics Markets and Technology Conference and Exhibition*, Sept. 1972.
11. Clement, J. R., and Quinell, E. H., "The Low Temperature Characteristics of Carbon-Composition Thermometers," *Review of Scientific Instruments*, Vol. 23, No. 5, p. 213, May 1952.

12. American Institute of Physics Handbook, Third Edition, Dwight E. Gray, Editor, p. 6-30.
13. Long, R. K., "Absorption of Laser Radiation in the Atmosphere," Report 1579-3, May 1963, The Ohio State University Electro-Science Laboratory, Department of Electrical Engineering; prepared under Contract AF-33(657)-10824 for Air Force Avionics Laboratory (AD 410 571).
14. Long, R. K., Mills, F. S., and Trusty, G. L., "Experimental Absorption Coefficients for Eleven CO Laser Lines," Report 3271-5, March 1973, The Ohio State University ElectroScience Laboratory, Department of Electrical Engineering; prepared under Contract F30602-72-C-0016 for Rome Air Development Center. (AD 760 140) (RADC-TR-73-126)
15. Young, C., "Calculation of the Absorption Coefficient for Lines with Combined Doppler and Lorentz Broadening," J. Quant. Spectrosc. Radit. Transfer, 5, (1965), p. 549.
16. Long, R. K., et al., "Calculated Absorption Coefficients for DF Laser Frequencies, Report 3271-7, November 1973, The Ohio State University ElectroScience Laboratory, Department of Electrical Engineering; prepared under Contract F30603-72-C-0016 for Rome Air Development Center. (AD 775 373) (RADC-TR-73-389)
17. Trusty, G. L., "Absorption Measurements of the 10.4 Micron Region Using a CO<sub>2</sub> Laser and a Spectrophone," Report 2819-4, January 1973, The Ohio State University ElectroScience Laboratory, Department of Electrical Engineering; prepared under Contract F33615-69-C-1807 for Air Force Avionics Laboratory. (AD 907 549) (AFAL-TR-72-413)
18. McClatchey, R. A., et al., "AFCRL Atmospheric Absorption Line Parameters Compilation," AFCRL-TR-73-0096 (1973).
19. Penner, S. S., Quantitative Molecular Spectroscopy and Gas Emissivities, Addison-Wesley Publishing Co. (1959).
20. Goody, R. M., Atmospheric Radiation. I. Theoretical Basis, Oxford Press (1964).
21. Herzberg, Gerhard, Spectra of Diatomic Molecules, Van Nostrand Reinhold Co. (1939).
22. Burch, D. E., et al., "Infrared Absorption by Minor Atmospheric Constituents," AF-19(604)263 (1960), p. 3.
23. Smith, W. V., et al., "Pressure Broadening of Linear Molecules. II. Theory," The Journal of Chemical Physics, 23, 339 (1955).

## APPENDIX A

### LORENTZ LINE SHAPE DATA

The following tables represent direct Lorentz line shape measurements for CO<sub>2</sub> and N<sub>2</sub>O gases. No curve fitting or data smoothing routines were used (if such processing is desired refer to Chapter 3), so that the data may be more useful for analysis.

The tables list in a vertical fashion the line identification along with the nature of the broadening, i.e., no foreign broadener, nitrogen broadened, or helium broadened. The columns are labeled for the pressure, both absorber and foreign in torr, the halfwidth in (cm<sup>-1</sup>), and the absorption coefficient given both in (km<sup>-1</sup>) and (cm<sup>2</sup>/molecule), symbolized by  $k(\gamma)$  and  $k'(\gamma)$ , respectively. To compute  $k'(\gamma)$ , the absorber amount,  $u$ , is needed, which is expressed in the formula,  $u = .733952 \times 10^{22} (p_a/760) \cdot \ell/T$ , with the units (mol/cm<sup>2</sup>), where  $p_a$  is the absorber partial pressure in torr,  $T$  is the temperature in degrees Kelvin, and  $\ell$  is the path length in cm. Then using  $T = e^{-k'(\gamma)u}$  and Eq. 6, the absorption coefficient and line strength are found. All measurements were made at a temperature of 296 K.



Table 6. Lorentz Line Shape Data, CO<sub>2</sub> 11'0-00°0

LINE ID: R(24)	PRESSURE ABSORBER (TORR)	FOREIGN (TORR)	HALFWIDTH (1/CM)	ABSORPTION COEFFICIENT (1/KM) (1/MOL*(1/CM)**2)	ABSORBER AMOUNT (MOL*(1/CM)**2)	LINE STRENGTH (1/CM)/(MOL*(1/CM)**2)
60.0	0.0	0.0	.0079	10.012	.7830E 22	.1274E-23
120.0	0.0	0.0	.0129	10.012	.1566E 23	.1037E-23
240.0	0.0	0.0	.0245	10.012	.3132E 23	.9841E-24
480.0	0.0	0.0	.0526	10.012	.6264E 23	.1056E-23
NITROGEN BROADENED						
60.0	0.0	0.0	.0075	10.012	.7830F 22	.1205E-23
60.0	60.0	0.0	.0139	5.930	.7830E 22	.1300E-23
60.0	180.0	0.0	.0238	2.970	.7830E 22	.1134E-23
HELIUM BROADENED						
60.0	0.0	0.0	.0074	10.012	.7830E 22	.1197E-23
60.0	60.0	0.0	.0117	6.340	.7830E 22	.1190E-23
60.0	180.0	0.0	.0221	3.367	.7830E 22	.1194E-23
LINE ID: R(28)						
60.0	0.0	0.0	.0074	15.582	.4698E 22	.1851E-23
120.0	0.0	0.0	.0139	15.582	.9396E 22	.1738E-23
240.0	0.0	0.0	.0271	15.582	.1679E 23	.1694E-23
NITROGEN BROADENED						
60.0	0.0	0.0	.0073	15.461	.4698E 22	.1809E-23
60.0	60.0	0.0	.0119	8.524	.4698E 22	.1629E-23
HELIUM BROADENED						
60.0	0.0	0.0	.0076	15.764	.4698E 22	.1913E-23
60.0	72.0	0.0	.0132	9.402	.4698E 22	.1989E-23
60.0	180.0	0.0	.0215	5.898	.4698E 22	.2033E-23

Table 6 (continued)

ABSORBER (TORR)	PRESSURE FOREIGN (TORR)	HALFWIDTH (1/CM)	ABSORPTION COEFFICIENT (1/KM)	ABSORBER AMOUNT (MOL*(1/CM)**2)	LINE STRENGTH ((1/CM)/(MOL*(1/CM)**2))
LINE ID: R(30)					
60.0	0.0	.0072	21.157	.7830E 22	.2445E-23
120.0	0.0	.0127	21.157	.1566E 23	.2156E-23
240.0	0.0	.0260	21.157	.3132E 23	.2207E-23
480.0	0.0	.0511	21.157	.6264E 23	.2169E-23
NITROGEN BROADENED					
60.0	0.0	.006A	21.157	.7830E 22	.2316E-23
60.0	72.0	.0132	10.693	.7830E 22	.2263E-23
60.0	180.0	.0233	6.212	.7830E 22	.2324E-23
HELIUM BROADENED					
60.0	0.0	.006A	21.157	.7830E 22	.2309E-23
60.0	60.0	.0112	13.318	.7830E 22	.2394E-23
60.0	180.0	.0202	7.192	.7830E 22	.2332E-23
LINE ID: R(34)					
60.0	0.0	.0071	23.798	.7830E 22	.2712E-23
120.0	0.0	.0123	23.798	.1566E 23	.2349E-23
240.0	0.0	.0251	23.798	.3132E 23	.2397E-23
480.0	0.0	.0501	23.798	.6264E 23	.2392E-23
NITROGEN BROADENED					
60.0	0.0	.0074	23.798	.7830E 22	.2826E-23
60.0	60.0	.0125	14.540	.7830E 22	.2917E-23
60.0	180.0	.0245	6.894	.7830E 22	.2711E-23
HELIUM BROADENED					
60.0	0.0	.0072	23.798	.7830E 22	.2765E-23
60.0	60.0	.0114	14.991	.7830E 22	.2743E-23
60.0	180.0	.0192	8.005	.7830E 22	.2467E-23

Table 6 (continued)

PRESSURE		HALFWIDTH (1/CM)	ABSORPTION COEFFICIENT		ABSORBER AMOUNT (MOL*(1/CM)**2)	LINE STRENGTH (1/CM)/(MOL*(1/CM)**2)
ABSORBER (TORR)	FOREIGN (TORR)		(1/KM)	(1/MOL*(1/CM)**2)		
LINE ID: R(36)						
60.0	0.0	.0070	24.124	.1232E-21	.7830E 22	.2710E-23
120.0	0.0	.0125	24.124	.6162E-22	.1566E 23	.2420E-23
240.0	0.0	.0236	24.124	.3081E-22	.3132E 23	.2264E-23
480.0	0.0	.0480	24.124	.1540E-22	.6264E 23	.2323E-23
NITROGEN BROADENED						
60.0	0.0	.0069	24.124	.1232E-21	.7830E 22	.2671E-23
60.0	60.0	.0128	14.097	.7201E-22	.7830E 22	.2896E-23
60.0	180.0	.0266	8.040	.4107E-22	.7830E 22	.3432E-23
HELIUM BROADENED						
60.0	0.0	.0069	24.124	.1232E-21	.7830E 22	.2671E-23
60.0	60.0	.0113	14.855	.7589E-22	.7830E 22	.2706E-23
60.0	180.0	.0201	8.422	.4302E-22	.7830E 22	.2717E-23
LINE ID: R(44)						
60.0	0.0	.0070	19.359	.9885E-22	.7830E 22	.2190E-23
120.0	0.0	.0132	19.359	.4945E-22	.1566E 23	.2051E-23
240.0	0.0	.0273	19.359	.2472E-22	.3132E 23	.2120E-23
HELIUM BROADENED						
60.0	0.0	.0073	19.359	.9885E-22	.7830E 22	.2268E-23
60.0	60.0	.0111	11.157	.5700E-22	.7830E 22	.1980E-23
60.0	180.0	.0255	6.469	.3305E-22	.7830E 22	.2647E-23

Table 6 (continued)

ABSORBER PRESSURE (TORR)	FOREIGN (TORR)	HALFWIDTH (1/CM)	ABSORPTION COEFFICIENT (1/KM)	ABSORBER AMOUNT (MOL*(1/CM)**2)	LINE STRENGTH ((1/CM)/(MOL*(1/CM)**2))
LINE ID: R(46)					
60.0	0.0	.0076	13.748	.7830E 22	.1677E-23
120.0	0.0	.0122	13.748	.1566E 23	.1346E-23
240.0	0.0	.0240	13.748	.3132E 23	.1324E-23
480.0	0.0	.0446	13.748	.6254E 23	.1230E-23
NITROGEN BROADENED					
60.0	0.0	.0070	13.748	.7830E 22	.1544E-23
60.0	60.0	.0123	8.005	.7830E 22	.1580E-23
HELIUM BROADENED					
60.0	0.0	.0070	13.748	.7830E 22	.1555E-23
60.0	60.0	.0110	8.527	.7830E 22	.1505E-23
LINE ID: R(46)					
60.0	0.0	.0062	15.822	.9396E 22	.1685E-23
120.0	0.0	.0109	16.822	.1879E 23	.1473E-23
240.0	0.0	.0205	16.822	.3759E 23	.1384E-23
480.0	0.0	.0468	16.822	.7517E 23	.1579E-23
LINE ID: R(48)					
60.0	0.0	.0069	13.865	.9396E 22	.1535E-23
120.0	0.0	.0114	13.865	.1879E 23	.1266E-23
240.0	0.0	.0207	13.865	.3759E 23	.1152E-23
480.0	0.0	.0426	13.865	.7517E 23	.1185E-23

Table 7. Lorentz Line Shape Data, N<sub>2</sub>O 20°0-01'0

PRESSURE ABSORBER (TORR)	HALFWIDTH (1/CM)	ABSORPTION COEFFICIENT (1/KM)	ABSORBER AMOUNT (MOL*(1/CM)**2)	LINE STRENGTH (1/CM)/(MOL*(1/CM)**2)
LINE ID: P(12)				
50.0 0.0	.0085	34.959	.7830E 22	.4791E-23
120.0 0.0	.0159	34.959	.1566E 23	.4466E-23
240.0 0.0	.0316	34.959	.3132E 23	.4438E-23
480.0 0.0	.0617	34.959	.6264E 23	.4329E-23
NITROGEN BROADENED				
60.0 0.0	.0085	36.204	.7830E 22	.4962E-23
60.0 60.0	.0151	21.510	.7830E 22	.5226E-23
60.0 180.0	.0319	11.432	.7830E 22	.5842E-23
HELIUM BROADENED				
60.0 0.0	.0085	35.887	.7830E 22	.4890E-23
60.0 60.0	.0134	22.229	.7830E 22	.4735E-23
60.0 180.0	.0225	11.830	.7830E 22	.4276E-23
LINE ID: P(13)				
50.0 0.0	.0084	37.967	.7830E 22	.5143E-23
120.0 0.0	.0154	37.967	.1566E 23	.4680E-23
240.0 0.0	.0299	37.967	.3132E 23	.4549E-23
480.0 0.0	.0610	37.967	.6264E 23	.4648E-23
NITROGEN BROADENED				
60.0 0.0	.0084	37.853	.7830E 22	.5127E-23
60.0 60.0	.0138	23.159	.7830E 22	.5149E-23
60.0 180.0	.0255	12.235	.7830E 22	.5013E-23
HELIUM BROADENED				
60.0 0.0	.0085	37.967	.7830E 22	.5155E-23
60.0 60.0	.0128	25.541	.7830E 22	.5247E-23
60.0 180.0	.0221	14.755	.7830E 22	.5244E-23



Table 7 (continued)

PRESSURE ABSORBER (TORR)	FOREIGN (TORR)	HALFWIDTH (1/CM)	ABSORPTION COEFFICIENT (1/KM)	ABSORPTION COEFFICIENT (1/MOL*(1/CM)**2)	ABSORBER AMOUNT (MOL*(1/CM)**2)	LINE STRENGTH ((1/CM)/(MOL*(1/CM)**2))
LINE ID: P(16)						
60.0	0.0	.0079	40.519	.2070E-21	.9396E 22	.5137E-23
120.0	0.0	.0151	40.519	.1035E-21	.1879E 23	.4919E-23
240.0	0.0	.0293	40.519	.5175E-22	.3759E 23	.4771E-23
480.0	0.0	.0587	40.519	.2587E-22	.7517E 23	.4771E-23
NITROGEN BROADENED						
60.0	0.0	.0079	40.086	.2048E-21	.9396E 22	.5102E-23
60.0	60.0	.0139	22.046	.1167E-21	.9396E 22	.5071E-23
60.0	180.0	.0257	12.304	.6285E-22	.9396E 22	.5069E-23
HELIUM BROADENED						
60.0	0.0	.0076	40.086	.2046E-21	.9396E 22	.4921E-23
60.0	60.0	.0122	24.875	.1271E-21	.9396E 22	.4878E-23
60.0	180.0	.0224	13.855	.7063E-22	.9396E 22	.4991E-23
LINE ID: P(19)						
60.0	0.0	.0084	40.519	.2070E-21	.9396E 22	.5443E-23
120.0	0.0	.0147	40.519	.1035E-21	.1879E 23	.4796E-23
240.0	0.0	.0282	40.519	.5175E-22	.3759E 23	.4586E-23
480.0	0.0	.0573	40.519	.2587E-22	.7517E 23	.4656E-23
NITROGEN BROADENED						
60.0	0.0	.0077	40.519	.2070E-21	.9396E 22	.5027E-23
60.0	60.0	.0139	22.660	.1158E-21	.9396E 22	.5069E-23
60.0	180.0	.0259	12.992	.6637E-22	.9396E 22	.5409E-23
HELIUM BROADENED						
60.0	0.0	.0080	40.086	.2046E-21	.9396E 22	.5147E-23
60.0	60.0	.0122	25.013	.1270E-21	.9396E 22	.4897E-23
60.0	180.0	.0203	13.987	.7145E-22	.9396E 22	.4559E-23

Table 7 (continued)

ABSORBER (TORR)	PRESSURE FOREIGN (TORR)	HALFWIDTH (1/CM)	ABSORPTION COEFFICIENT (1/KM)	ABSORPTION COEFFICIENT (1/MOL*(1/CM)**2)	ABSORBER AMOUNT (MOL*(1/CM)**2)	LINE STRENGTH (1/CM)/(MOL*(1/CM)**2)
LINE ID: P(21)						
50.0	0.0	.0064	35.653	.2186E-21	.3915E 22	.4429E-23
100.0	0.0	.0115	38.179	.1170E-21	.7830E 22	.4239E-23
200.0	0.0	.0235	33.179	.5851E-22	.1566E 23	.4323E-23
400.0	0.0	.0494	38.179	.2925E-22	.3112E 23	.4556E-23
NITROGEN BROADENED						
50.0	0.0	.0064	34.684	.2126E-21	.3915E 22	.4268E-23
50.0	50.0	.0109	20.053	.1229E-21	.3915E 22	.4225E-23
50.0	150.0	.0224	10.406	.6379E-22	.3915E 22	.4495E-23
HELIUM BROADENED						
25.0	25.0	.0057	20.120	.2467E-21	.1958E 22	.4433E-23
25.0	75.0	.0098	12.210	.1497E-21	.1958E 22	.4613E-23
LINE ID: P(22)						
60.0	0.0	.0074	37.287	.1905E-21	.9396E 22	.4542E-23
120.0	0.0	.0145	37.287	.9524E-22	.1879E 23	.4338E-23
240.0	0.0	.0268	37.287	.4762E-22	.3759E 23	.4308E-23
480.0	0.0	.0582	37.287	.2381E-22	.7517E 23	.4353E-23

Table 7 (continued)

PRESSURE ABSORBER FOREIGN (TCRR) (TCRR)	HALFWIDTH (1/CM)	ABSORPTION COEFFICIENT (1/KM)	ABSORBER AMOUNT (MOL*1/CM)**2)	LINE STRENGTH ((1/CM)/(MOL*(1/CM)**2))
LINE ID: P(23)				
60.0 0.0	.0074	36.794	.9396E 22	.4352E-23
120.0 0.0	.0146	36.794	.1879E 23	.4302E-23
240.0 0.0	.0291	36.794	.3759E 23	.4291E-23
480.0 0.0	.0583	36.794	.7517E 23	.4303E-23
NITROGEN BROADENED				
60.0 0.0	.0082	37.792	.9396E 22	.4973E-23
60.0 87.0	.0161	19.457	.9396E 22	.5021E-23
60.0 180.0	.0248	12.645	.9396E 22	.5033E-23
HELIUM BROADENED				
60.0 0.0	.0077	36.672	.9396E 22	.4526E-23
60.0 60.0	.0125	23.869	.9396E 22	.4807E-23
60.0 180.0	.0231	13.384	.9396E 22	.4964E-23
LINE ID: P(27)				
60.0 0.0	.0091	28.306	.9396E 22	.4120E-23
120.0 0.0	.0158	28.306	.1879E 23	.3582E-23
240.0 0.0	.0290	28.306	.3759E 23	.3299E-23
NITROGEN BROADENED				
60.0 0.0	.0096	26.669	.9396E 22	.4113E-23
60.0 60.0	.0146	17.056	.9396E 22	.3986E-23
60.0 180.0	.0300	9.892	.9396E 22	.4763E-23
HELIUM BROADENED				
60.0 0.0	.0098	28.633	.9396E 22	.4494E-23
60.0 60.0	.0145	18.728	.9396E 22	.4367E-23
60.0 180.0	.0279	10.817	.9396E 22	.4838E-23

## APPENDIX B

### VOIGT LINE SHAPE DATA

The following tables represent direct Voigt line shape measurements for CO<sub>2</sub> and N<sub>2</sub>O gases. The tables are structured similarly to those on Lorentz line shape, except no foreign broadening effects are listed, no line strengths are listed because there is not a direct method of calculation from the given experimental data, and a calculated halfwidth (this procedure is outlined in Chapter 3, p. 29) is listed for comparison with measured halfwidths.



Table 8. Voigt Line Shape Data, CO<sub>2</sub> 11'0-00°0

PRESSURE (TORR)	HALFWIDTH MEASURED (1/CM)	HALFWIDTH CALCULATED (1/CM)	ABSORPTION COEFFICIENT (1/KM)	ABSORPTION COEFFICIENT (1/MOL*(1/CM)**2)	ABSORBER AMOUNT (MOL*(1/CM)**2)
LINE ID: R(24)					
.45	.0018	.0018	.251	.1711E-21	.1075E 22
1.00	.0024	.0019	.854	.2615E-21	.2388E 22
5.00	.0027	.0021	2.979	.1826E-21	.1194E 23
15.00	.0033	.0028	7.292	.1490E-21	.1958E 22
30.00	.0045	.0040	9.096	.9293E-22	.3915E 22
60.00	.0075	.0068	10.012	.5115E-22	.7830E 22
LINE ID: R(26)					
.14	.0017	.0018	.117	.2559E-21	.3344E 21
1.00	.0018	.0019	.941	.2886E-21	.2388E 22
3.00	.0021	.0020	2.041	.2902E-21	.7165E 22
LINE ID: R(28)					
3.00	.0022	.0020	3.274	.3345E-21	.7165E 22
15.00	.0027	.0028	10.999	.2247E-21	.1175E 22
30.00	.0039	.0040	14.506	.1482E-21	.2349E 22
60.00	.0074	.0068	15.582	.7960E-22	.4698E 22



Table 8 (continued)

PRESSURE (TORR)	MEASURED HALFWIDTH (1/CM)	ABSORPTION COEFFICIENT (1/KM)	ABSORPTION COEFFICIENT (1/MOL*(1/CM)**2)	ABSORBER AMOUNT (MOL*(1/CM)**2)
LINE ID: R(30)				
.30	.0017	.201	.2668E-21	.7165E 21
3.00	.0029	2.199	.2246E-21	.7165E 22
15.00	.0026	15.220	.3110E-21	.1958E 22
30.00	.0041	18.769	.1918E-21	.3915E 22
60.00	.0072	21.099	.1078E-21	.7830E 22
LINE ID: R(32)				
.15	.0019	.167	.3410E-21	.3582E 21
1.00	.0021	1.622	.4972E-21	.2384E 22
3.00	.0027	4.746	.4848E-21	.7165E 22
LINE ID: R(34)				
.15	.0017	.225	.4602E-21	.3582E 21
1.00	.0023	1.715	.5256E-21	.2384E 22
3.00	.0026	3.914	.3980E-21	.7165E 22
15.00	.0036	14.810	.3026E-21	.1958E 22
30.00	.0044	20.298	.2074E-21	.3915E 22
60.00	.0071	23.798	.1216E-21	.7830E 22

Table 8 (continued)

PRESSURE (TORR)	HALFWIDTH MEASURED (1/CM)	HALFWIDTH CALCULATED (1/CM)	ABSORPTION COEFFICIENT (1/KM)	ABSORPTION COEFFICIENT (1/MOL*(1/CM)**2)	ABSORBER AMOUNT (MOL*(1/CM)**2)
LINE ID: R(36)					
.16	.0018	.0018	.175	.3345E-21	.3821E 21
1.00	.0020	.0019	1.269	.3889E-21	.2388E 22
3.00	.0023	.0020	4.148	.4238E-21	.7165E 22
15.00	.0033	.0027	15.072	.3243E-21	.1958E 22
30.00	.0039	.0037	20.658	.2109E-21	.3915E 22
60.00	.0070	.0061	24.124	.1232E-21	.7830E 22
LINE ID: R(38)					
.03	.0019	.0018	.043	.4395E-21	.7165E 21
.83	.0020	.0019	1.450	.5354E-21	.1982E 21
3.00	.0027	.0020	4.093	.4181E-21	.7165E 22
15.00	.0031	.0027	13.266	.2711E-21	.2349E 22
30.00	.0039	.0037	18.474	.1887E-21	.4698E 22
60.00	.0062	.0061	23.738	.1213E-21	.9396E 22
LINE ID: R(42)					
1.00	.0021	.0019	.947	.2902E-21	.2388E 22
3.00	.0027	.0020	2.437	.2490E-21	.7165E 22

Table 8 (continued)

PRESSURE (TORR)	HALFWIDTH MEASURED (1/CM)	HALFWIDTH CALCULATED (1/CM)	ABSORPTION COEFFICIENT (1/KM)	ABSORPTION COEFFICIENT (1/MOL*(1/CM)**2)	ABSORBER AMOUNT (MOL*(1/CM)**2)
LINE ID: R(44)					
15.00	.0035	.0027	12.113	.2475E-21	.1958E 22
30.00	.0044	.0037	16.204	.1656E-21	.3915E 22
60.00	.0070	.0061	19.359	.9889E-22	.7830E 22
LINE ID: R(46)					
.28	.0019	.0018	.346	.3792E-21	.6687E 21
3.00	.0026	.0020	2.185	.2332E-21	.7165E 22
15.00	.0031	.0027	10.752	.2303E-21	.2349E 22
30.00	.0040	.0037	13.623	.1392E-21	.4698E 22
60.00	.0062	.0061	16.822	.8593E-22	.9396E 22
LINE ID: R(48)					
.20	.0017	.0016	.147	.2552E-21	.4776E 21
1.00	.0022	.0019	.589	.1804E-21	.2388E 22
3.00	.0025	.0020	1.636	.1722E-21	.7165E 22
15.00	.0036	.0027	7.018	.1434E-21	.2349E 22
30.00	.0046	.0037	10.712	.1094E-21	.4698E 22
60.00	.0069	.0061	13.865	.7003E-22	.9396E 22

Table 9. Voigt Line Shape Data, N<sub>2</sub>O 20°0-01'0

PRESSURE (TORR)	HALFWIDTH MEASURED	HALFWIDTH CALCULATED (1/CM)	ABSORPTION COEFFICIENT (1/KM)	ABSORPTION COEFFICIENT (1/MOL*(1/CM)**2)	ABSORBER AMOUNT (MOL*(1/CM)**2)
LINE ID: P(12)					
15.00	.0033	.0030	26.317	.5378E-21	.1958E 22
30.00	.0045	.0044	32.003	.3270E-21	.3915E 22
60.00	.0065	.0076	34.959	.1786E-21	.7830E 22
LINE ID: P(13)					
15.00	.0037	.0030	22.106	.4517E-21	.1958E 22
30.00	.0050	.0044	30.775	.3144E-21	.3915E 22
60.00	.0084	.0076	37.967	.1940E-21	.7830E 22
LINE ID: P(16)					
15.00	.0032	.0029	27.511	.6621E-21	.2349E 22
30.00	.0045	.0044	35.495	.3626E-21	.4698E 22
60.00	.0079	.0076	40.519	.2070E-21	.9396E 22

Table 9 (continued)

PRESSURE (TORR)	MEASURED HALFWIDTH (1/CM)	CALCULATED HALFWIDTH (1/CM)	ABSORPTION COEFFICIENT (1/KM) (1/MOL*(1/CM)**2)	ABSORBER AMOUNT (MOL*(1/CM)**2)
LINE ID: P(19)				
15.00	.0037	.0029	23.351	.4772E-21
30.00	.0052	.0044	33.117	.384E-21
60.00	.0080	.0076	40.519	.2070E-21
				.2349E 22
				.4698E 22
				.9396E 22
LINE ID: P(21)				
25.00	.0037	.0039	31.194	.3824E-21
50.00	.0064	.0065	35.653	.2166E-21
				.1958E 22
				.3915E 22
LINE ID: P(22)				
15.00	.0032	.0029	24.534	.5013E-21
30.00	.0045	.0044	31.076	.3175E-21
60.00	.0076	.0076	37.287	.1905E-21
				.2349E 22
				.4698E 22
				.9396E 22
LINE ID: P(23)				
15.00	.0034	.0029	23.415	.4785E-21
30.00	.0049	.0044	31.735	.3242E-21
60.00	.0074	.0076	36.794	.1880E-21
				.2349E 22
				.4698E 22
				.9396E 22



Table 9 (continued)

PRESSURE (TORR)	HALFWIDTH MEASURED (1/CM)	HALFWIDTH CALCULATED (1/CM)	ABSORPTION COEFFICIENT (1/KM) (1/MOL*(1/CM)**2)	ABSORBER AMOUNT (MOL*(1/CM)**2)
LINE ID: P(27)				
15.00	.0039	.0028	18.073	.2349E 22
30.00	.0054	.0040	24.400	.4698E 22
60.00	.0091	.0068	28.306	.9396E 22

## APPENDIX C

### SPECTRAL LINE INTENSITY

#### A. Spectral Line Intensity

The absorption coefficient is a function of the characteristics of the absorber molecules, foreign molecules, and the frequency of the electromagnetic wave. The analysis of this function is usually accomplished by expressing the dependencies of the molecular systems and radiation frequency by the general relation for a single absorption line

$$(17) \quad k([M_a], [M_f], \gamma) \\ = \sum_q S(M_{aq}) j(\alpha(M_{aq}; M_{f1q}, M_{f2q}, \dots, M_{frq}; \gamma_0), \gamma - \gamma_0)$$

where

- $[M_a]$  - is a row matrix of parameters representing absorbing molecules with  $M_{aq}$  as the  $q^{th}$  element
- $[M_f]$  - is a  $r$  by  $q$  matrix of parameters representing foreign molecules acting on the  $q^{th}$  absorbing molecule, with  $M_{frq}$  as the  $rq^{th}$  element
- $\gamma$  - wavenumber
- $S(M_{aq})$  - line strength of  $q^{th}$  absorbing molecule
- $j(\alpha)$  - line shape function
- $\alpha(\ )$  - halfwidth at half intensity of the line shape
- $\gamma_0$  - wavenumber at line center.

For the purposes of this study only one absorbing molecule and one foreign molecule shall be considered. This simplifies the equation for the absorption coefficient to

$$(18) \quad k(M_{a1}, M_{f11}, \gamma) = S(M_{a1}) j(\alpha(M_{a1}, M_{f11}, \gamma_0), \gamma - \gamma_0)$$

It is interesting to note that the line strength is a function of the absorbing molecule only. The line shape function depends on the frequency and is a composite function of the independent variables of the absorbing molecule, the foreign molecule, and the line center wavenumber. It is convenient to normalize

$j(\alpha(M_{a1}, M_{f11}, \gamma_0, \gamma - \gamma_0))$  by requiring the integration of  $j$  over all  $\gamma$  to be equal to one, so that

$$(19) \quad \int_{-\infty}^{\infty} k(M_{a1}, M_{f11}, \gamma) d\gamma = S(M_{a1})$$

where

$$(20) \quad \int_{-\infty}^{\infty} j(\alpha(M_{a1}, M_{f11}, \gamma_0), \gamma - \gamma_0) d\gamma = 1$$

The parameters  $M_a$  and  $M_f$  are themselves multi-variable functions of quantities affecting the properties of the associated molecular systems. They are used here to emphasize this fact and, having served that purpose, shall be eliminated from the notation and replaced by more explicit variables. The description of the absorption coefficient,  $k(\gamma)$ , can now be broken down into two parts, the line strength and the line shape function.

### 1. The Line Strength

The line strength is a measure of the intensity for a particular absorption line. Intuitively the line strength should be related to the probability of a particular transition occurring and the population of the lower energy state. This is expressed in the formula for the line strength [19,20].

$$(21) \quad S_{lu}^J = \frac{N_l}{g_u} \frac{8 \pi^3 \gamma_{lu}}{3 h} |R_{lu}^i|^2 \left( 1 - e^{-hc\gamma_{lu}/kT} \right)$$

where

- $N_l$  - number of molecules per unit volume in the lower quantum state
- $g_u$  - degeneracy of upper quantum state
- $\gamma_{lu}$  - wavenumber of incident radiation
- $h$  - Planck's constant
- $|R_{lu}^i|^2$  - transition moment
- $T$  - temperature in K
- $k$  - Boltzmann's constant.

The superscript  $J$  on  $S_{lu}^J$  represents the rotational quantum number and serves as a reminder of the dependence of the line strength for a particular vibration band on  $J$ . The transition moment as discussed by Herzberg [21] may be written as

$$(22) \quad R_{\ell u}^i = \langle \ell | M_i | u \rangle$$

where  $\langle \ell |$  and  $| u \rangle$  are the lower and upper eigenstates, respectively, and  $M_i$  represents the electric dipole moment with the subscript  $i$  denoting components in the  $x$ ,  $y$ , and  $z$  directions. The dipole moment is the major mechanism of interaction between the electromagnetic field and molecular system. Other mechanisms of interaction may be present, such as electric quadrupoles and magnetic moments, but are by far weaker. Thus, the line strength is a function of the absorber molecule via the temperature, the population distributions, the wavefunctions, the dipole moment, and the incident radiation wavenumber. The line strength as used by McClatchey, et al. [18] places the pressure dependence of  $S_{\ell u}^J$ , represented by  $N_{\ell}$  into the absorption coefficient  $k'$ . Thus the line strength,  $S_{\ell u}^J$ , is generally considered to be independent of pressure, however, this assumes that the wavefunctions are unperturbed by neighboring systems.

## 2. The Line Shape

The line shape of a pressure broadened absorption line is determined by the perturbations of exterior systems upon the absorber molecule. A smearing of the energy levels results from these disturbances, which produce a probability distribution of the energy level shifts. For a collision broadened line, the line shape function takes the form [18]

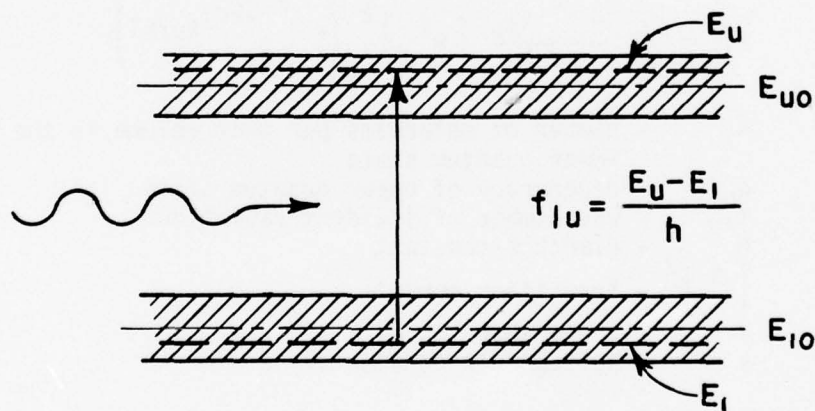


Fig. 41. Smearing of energy levels.

$$(23) \quad j_L (\gamma - \gamma_0) = \frac{1}{\pi} \frac{\alpha_c}{(\gamma - \gamma_0)^2 + \alpha_c^2} \quad .$$

This function is known as the Lorentz line shape. The half-width,  $\alpha_c$ , to a good approximation is determined by the kinetic theory of gases [22].

$$(24) \quad \alpha_c = \frac{1}{4\pi} \sum_j N_i (D_{a,i})^2 \left[ 2 \pi kT \left( \frac{1}{M_a} + \frac{1}{M_i} \right) \right]^{1/2}$$

where  $N_i$  - number of molecules of the  $i^{\text{th}}$ -type per volume  
 $D_{a,i}$  - optical collision diameter of the absorbing molecule related to the  $i^{\text{th}}$ -type molecule  
 $M_a$  - absorber mass  
 $M_i$  -  $i^{\text{th}}$ -type molecule's mass  
 $T$  - temperature in K  
 $k$  - Boltzmann's constant.

For an absorbing molecule with a single foreign broadener, the halfwidth becomes

$$(25) \quad \alpha_c = \frac{1}{4\pi} [2 \pi kT]^{1/2} \left\{ N_a (D_{a,a})^2 \left[ \frac{2}{M_a} \right]^{1/2} + N_f (D_{a,f})^2 \left[ \frac{1}{M_a} + \frac{1}{M_f} \right]^{1/2} \right\}$$

Using the relation  $N_i = \frac{P_i}{kT}$  and defining

$$(26) \quad B = \frac{(D_{a,a})^2 \left[ \frac{2}{M_a} \right]^{1/2}}{(D_{a,N_2})^2 \left[ \frac{1}{M_a} + \frac{1}{M_{N_2}} \right]^{1/2}}$$

$$(27) \quad F = \frac{(D_{a,f})^2 \left[ \frac{1}{M_a} + \frac{1}{M_f} \right]^{1/2}}{(D_{a,N_2})^2 \left[ \frac{1}{M_a} + \frac{1}{M_{N_2}} \right]^{1/2}}$$



the halfwidth becomes

$$(28) \quad \alpha_c = \frac{1}{4\pi} [2 \pi kT]^{1/2} \left[ \frac{P_a}{kT} B + \frac{P_f}{kT} F \right] (D_a, N_2)^2 \left[ \frac{1}{M_a} + \frac{1}{M_{N_2}} \right]^{1/2}$$

B represents the self-broadening coefficient and is measured relative to nitrogen as the equational definition demonstrates. F represents the foreign-broadening coefficient and is defined relative to nitrogen. When the foreign molecule is nitrogen gas, F equals one. To express the collision halfwidth in a standard form, the term  $P_e$ , the effective pressure, is introduced as

$$(29) \quad P_e = Bp_a + Fp_f \quad .$$

The halfwidth at standard temperature and pressure becomes

$$(30) \quad \alpha_{co} = \frac{(2\pi)^{1/2}}{4 \pi k} (D_a, N_2)^2 \left[ \frac{1}{M_a} + \frac{1}{M_{N_2}} \right] \frac{P_{eo}}{T_o^{1/2}} \quad .$$

For any pressure and temperature

$$(31) \quad \alpha_c = \alpha_{co} \frac{P_e}{P_{eo}} \left( \frac{T_o}{T} \right)^{1/2} \quad .$$

The kinetic theory does not account for all observed phenomenon concerning halfwidth measurements. It is necessary to treat the problem quantum mechanically. Using such an approach, the halfwidth displays a dependence on J, the rotational quantum number [23]. Increasing J-numbers produces decreasing halfwidths.

At low altitudes where the pressure is above 60-70 torr, the collision broadening and the Lorentz line shape will determine  $j(\gamma - \gamma_0)$ . However, at high altitudes where the atmospheric pressure is below 60-70 torr, a different line shape will occur. Due to the reduced number of molecules, fewer collisions occur. The spectral line shape is then influenced by the kinetic motion of the molecules. Such phenomenon is described by the Doppler effect. Pure Doppler broadening occurs around 0.1 torr and below, thus the pressure region between Doppler and collision broadening is a combination of the two phenomena.

The pure Doppler broadened line has a line shape via the Doppler equation and the Maxwell-Boltzmann distribution.

$$(32) \quad j_D(\gamma - \gamma_0) = \frac{(\ln 2)^{1/2}}{\alpha_D} \exp -\frac{(\gamma - \gamma_0)^2}{\alpha_D^2} (\ln 2)$$

where

$$(33) \quad \alpha_D = \left( \frac{2 kT \ln 2}{Mc^2} \right)^{1/2} \gamma_0 .$$

The shape is Gaussian in nature, which reduces the wing absorption as compared to a Lorentz profile. Figure 42 exhibits this fact for lines with the same halfwidth and line strength. Doppler lines are very much narrower than collision-broadened lines, for example typical values for  $\text{CO}_2$  at  $5 \mu\text{m}$  may be

$$\alpha_D = 0.0018$$

$$\alpha_C = 0.0800 \text{ @ } 760 \text{ torr.}$$

The combined Doppler and collisional broadening effects determine the Voigt line shape. Let the molecule have a stationary shape factor  $j'(\gamma - \gamma_0)$  and the velocity probability distribution of  $p(u)$  then

$$(34) \quad j_V(\gamma - \gamma_0) = \int_{-\infty}^{\infty} p(u) j'(\gamma - \gamma_0 + \frac{u}{c} \gamma_0) du .$$

Using Doppler's equation

$$(35) \quad \gamma' = \gamma_0 (1 - \frac{u}{c})$$

one obtains

$$(36) \quad \gamma - \gamma_0 + \gamma_0 \frac{u}{c} = (\gamma - \gamma_0) - (\gamma' - \gamma_0) .$$

$j'$  becomes the Lorentz line shape and  $p(u)$  is a Maxwell-Boltzmann distribution. Substituting into Eq. (34)  $j_V(\gamma - \gamma_0)$  becomes [19]

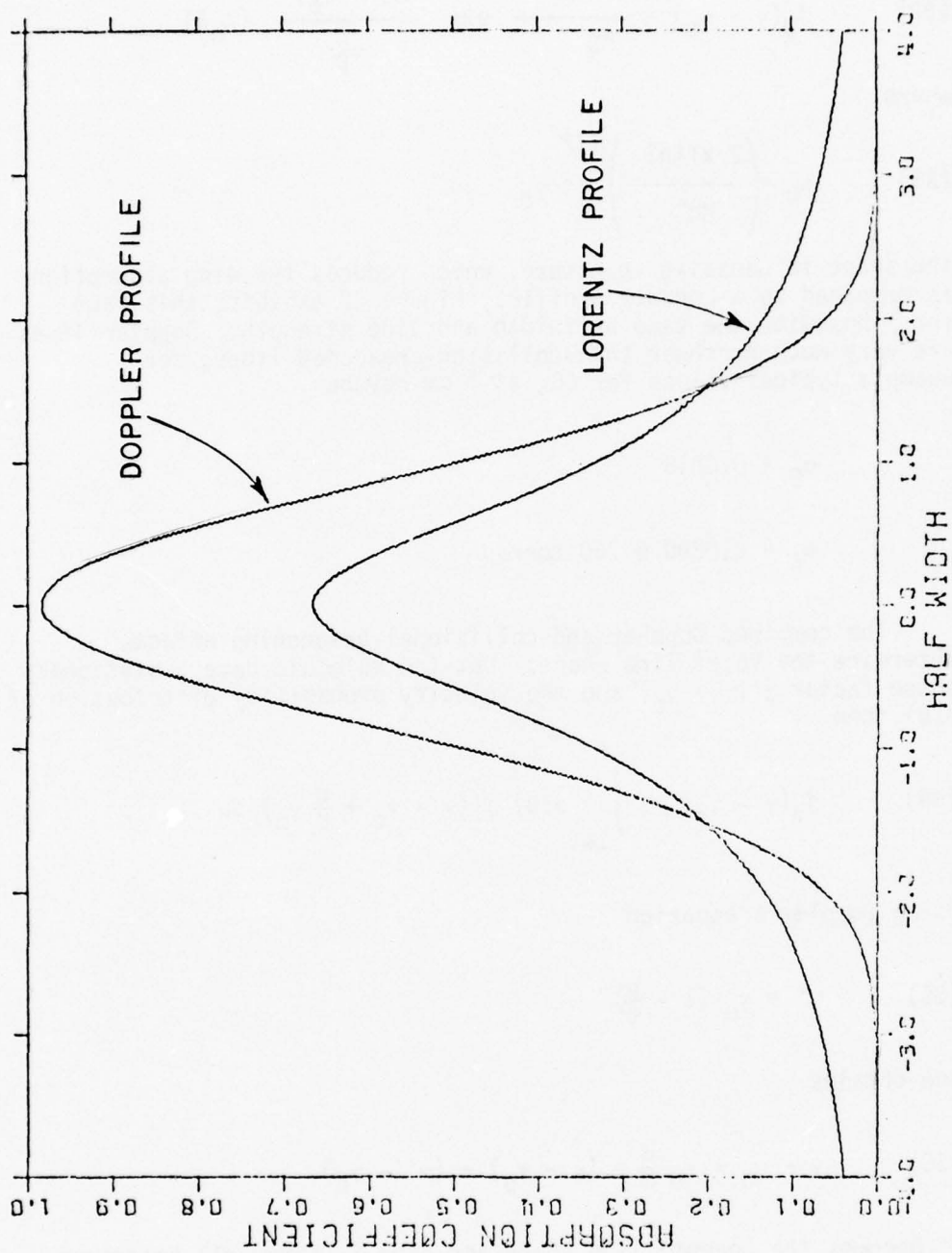


Fig. 42. Lorentz versus Doppler line shape. [17]

$$(37) \quad j_v(\gamma - \gamma_0) = \frac{1}{\pi^{3/2}} \frac{\alpha_c}{\alpha_D} (\ln 2)^{1/2} \cdot \int_{-\infty}^{\infty} \frac{\exp - \left( \frac{(\gamma' - \gamma_0)^2}{\alpha_D^2} \ln 2 \right)}{[(\gamma - \gamma_0) - (\gamma' - \gamma_0)]^2 + \alpha_c^2} dv'$$

$$\text{Let (38) } y = \frac{\gamma' - \gamma_0}{\alpha_D} (\ln 2)^{1/2}$$

$$(39) \quad a = \frac{\alpha_c}{\alpha_D} (\ln 2)^{1/2}$$

$$(40) \quad \zeta = \frac{\gamma - \gamma_0}{\alpha_D} (\ln 2)^{1/2}$$

then

$$(41) \quad j_v(\gamma - \gamma_0) = \frac{\alpha_c}{\alpha_D^2 \pi^{3/2}} \ln 2 \int_{-\infty}^{\infty} \frac{\exp(-y^2)}{(\zeta - y)^2 + a^2} dy$$

This is the expression for the Voigt line shape. The equations below summarize the results obtained in the description of the absorption coefficient. The equational forms are valid for either  $k$  or  $k'$ , however the dimensions of the parameters must be adjusted.

#### Lorentz Line Shape

$$(42a) \quad k(\gamma) = S_{lu}^J j_L(\gamma - \gamma_0) = \frac{S_{lu}^J}{\pi} \frac{\alpha_c}{(\gamma - \gamma_0)^2 + \alpha_c^2} \quad (\text{km}^{-1})$$

$$(42b) \quad k'(\gamma) = S_{lu}^{J'} j_L(\gamma - \gamma_0) = \frac{S_{lu}^{J'}}{\pi} \frac{\alpha_c}{(\gamma - \gamma_0)^2 + \alpha_c^2}$$

$$\left( \left( \text{mol (cm}^{-2}) \right)^{-1} \right)$$

### Voigt Line Shape

$$(43) \quad k(\gamma) = S_{\ell_u}^J j_V(\gamma - \gamma_0) = \frac{S_{\ell_u}^J \alpha_c}{\alpha_D^2 \pi^{3/2}} \ln 2 \int_{-\infty}^{\infty} \frac{\exp(-y)^2 dy}{(\zeta - y)^2 + a^2} (\text{km}^{-1})$$

### Doppler Line Shape

$$(44) \quad k(\gamma) = S_{\ell_u}^J j_D(\gamma - \gamma_0) = \frac{S_{\ell_u}^J (\ln 2)^{1/2}}{\alpha_D \sqrt{\pi}} \cdot \exp \left\{ - \left( \frac{\gamma - \gamma_0}{\alpha_D} \right)^2 \ln 2 \right\} (\text{km}^{-1})$$



PART D  
A DIFFERENTIAL SPECTROPHONE OF UNIQUE DESIGN

Contents

	Page
INTRODUCTION	D-1
A. Introduction	D-1
B. The O.S.U. Differential Spectrophone	D-3
THE EXPERIMENTAL APPARATUS	D-6
A. Introduction	D-6
B. The Stabilized CO <sub>2</sub> Laser	D-6
C. The Differential Spectrophone	D-9
D. Accessory Equipment	D-12
1. The Electronic Apparatus	D-12
2. Pressure Signal Processing	D-13
TEST MEASUREMENTS AND RESULTS	D-17
A. Introduction	D-17
B. Test Measurements	D-17
C. Experimental Procedure	D-22
D. Measurements	D-26
SUMMARY AND CONCLUSIONS	D-42
A. Summary	D-42
B. Conclusions	D-42
APPENDIX A	D-44
REFERENCES	D-48

## CHAPTER I

### INTRODUCTION

#### A. Introduction

This research was prompted by the need for a portable instrument capable of measuring molecular absorption coefficients on the order of  $10^{-8}$   $\text{cm}^{-1}$  with an accuracy of  $\pm 10\%$  using a one-watt c.w. laser source. The conventional method used for laboratory measurements of molecular absorption employs the multi-traversal or White cell [1]. In order to determine the transmittance for low absorption levels, this technique requires taking the ratio of two quantities that are very nearly equal. It can be easily shown [2] that a small error in this measurement will produce a larger error when it is used to determine the absorption coefficient. For a transmittance near 90%, Figure 1 shows that a 1% error in the transmittance will result in a 10% error in the absorption coefficient.

Measurements with a laser-illuminated spectrophone give results which are linearly related to the absorption coefficient so that this instrument is potentially capable of meeting the above specifications; however, a number of problems have limited its usefulness. These problems include calibration, "window" effects, and contaminants. The present effort has resulted in an improved instrument which will be described.

The optoacoustic effect, which was discovered in 1880 by Alexander Graham Bell [3], received relatively little attention until intense coherent light sources became available. The first attempts at employing this effect to measure absorption in gas samples were limited by the intensity of thermal radiation sources. Viengerov [4] made the first such measurements in 1938 using a pressure transducer mounted in a resonant cavity. However, it was the advent of the laser which allowed Kerr and Atwood [5] to demonstrate the potential of the spectrophone as a sensitive instrument for the measurement of weak absorptivity in gases. In 1967 they employed both a pulsed ruby and a c.w.  $\text{CO}_2$  laser for the purpose of measuring water vapor and  $\text{CO}_2$  absorption with a non-resonant gas sample cell and a capacitance manometer (pressure transducer). Using a chopping frequency of 0.19 Hz, they achieved a sensitivity of  $10^{-7}$   $\text{cm}^{-1}$ , that was limited by a false pressure

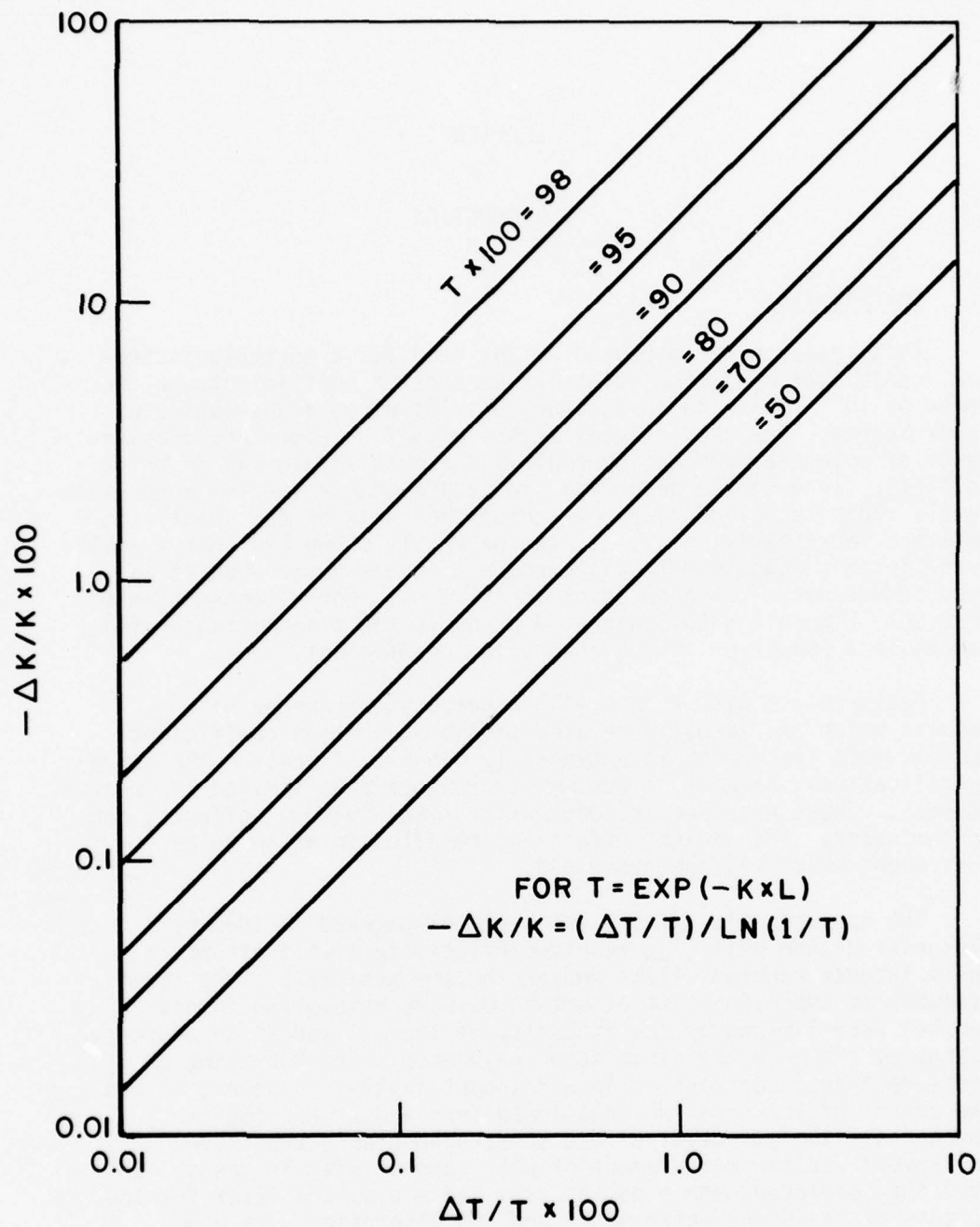


Figure 1. Percentage error in absorption coefficient plotted versus percentage error in transmittances.

signal which was proportional to laser power and associated with the end windows. In 1970 Kreuzer [6] used a non-resonant cell with a pressure sensing microphone in order to measure gas concentrations with a He-Ne laser and to further study the ultimate sensitivity of the spectrophone. At  $3.39 \mu$  he was able to achieve an experimental sensitivity of  $10^{-8}$  parts methane in air using a modulation frequency of 400 Hz in conjunction with a high Q, frequency selective amplifier. Amplifier noise limited sensitivity, while contaminants, i.e., gases trapped in the cell walls, apparently limited the accurate determination of low level absorber concentrations.

In an attempt to improve the acoustic technique, Dewey and co-workers [7] modulated the excitation beam at a frequency corresponding to a natural (Helmholtz) frequency of the sample cell, thus producing a resonant spectrophone. While the non-resonant acoustic (pressure) signal decreases with modulation frequency, this work demonstrated the enhancement of the pressure signal at or near the resonant frequencies of the sample cell ( $\sim 3900$  Hz). This type device has a relatively large volume-to-surface area ratio which should serve to reduce the problem of contamination but because of the large acoustic "Q" required and observed, this technique is extremely sensitive to variations in either modulation frequency or the speed of sound in different samples of gas.

Deaton, et al. [8], improved the sensitivity of the basic spectrophone by designing a non-resonant differential instrument consisting of two isolated chambers connected by a single IR window. This technique, which will be described later, served to substantially reduce the false pressure signal and produced an equivalent absorption background signal of  $3.3 \times 10^{-9} \text{ cm}^{-1}/\text{watt}$ . Because their instrument employs a sensitive differential capacitive manometer, (DCM) connected between two isolated chambers, small volume adjustments were required in one of the two cavities in order to equalize the static pressure across the manometer. It is believed that this practice could have a serious effect on the instrument calibration. This point will be given further consideration in Chapter III.

#### B. The O.S.U. Differential Spectrophone

The instrument shown schematically in Figure 2 was designed by Professor E. K. Damon to improve the spectrophone sensitivity by employing a "differential technique" similar to that considered in electronic amplifiers.

Our experience, like that of Kerr and Atwood [5], had shown that the principal problem associated with the achievement of

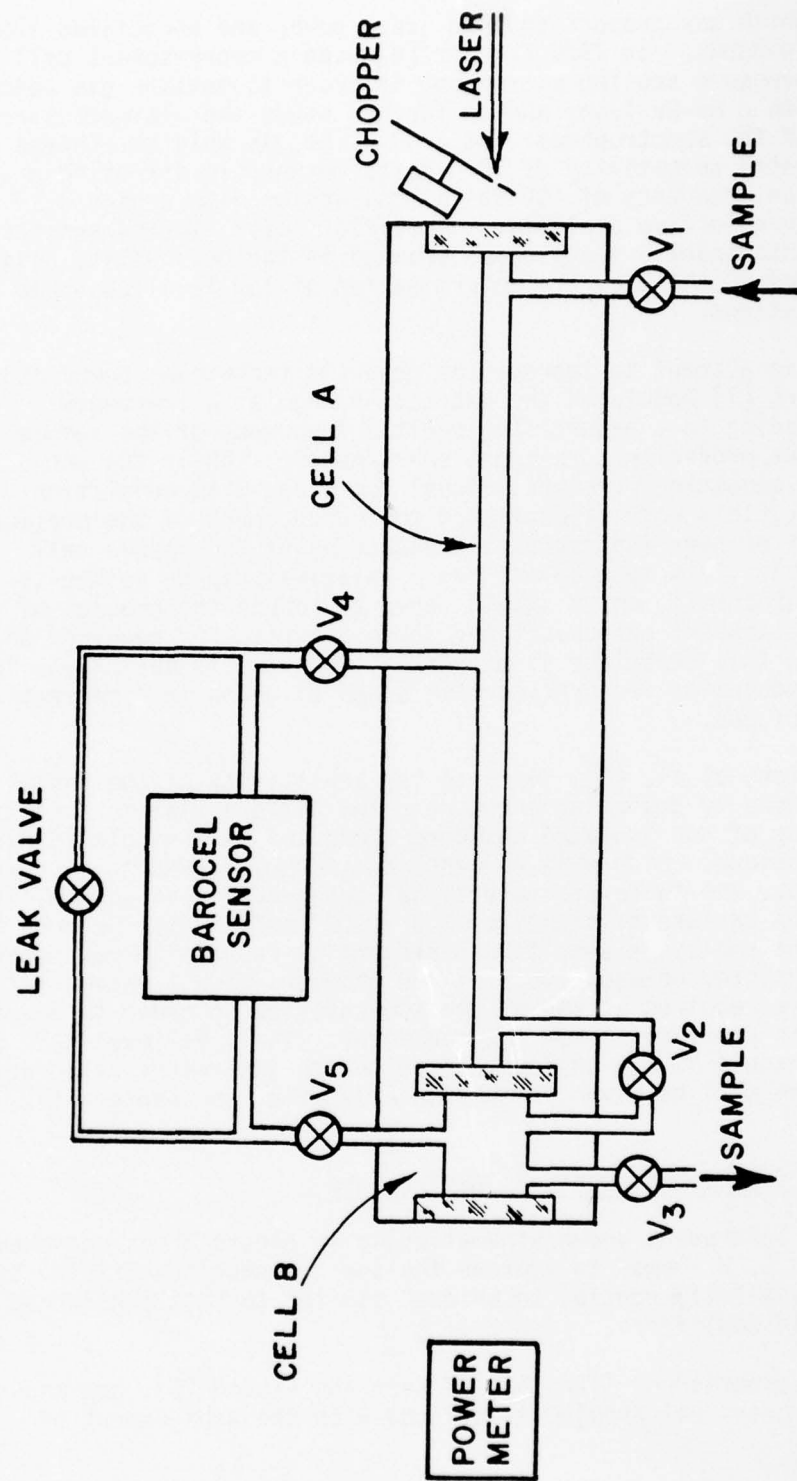


Figure 2. Differential spectrophone.



maximum sensitivity in the spectrophone was derived from a false pressure signal which generally could be attributed to "window noise." When performing measurements this "window noise" presented itself in the form of an in-phase signal that produced a constant background which seemed to naturally determine the lower limit of sensitivity. A more powerful radiation source could not improve the system signal-to-noise ratio, since the predominant noise source was also proportional to laser power. Further, its phase appeared to be nearly coincident with that of the desired pressure signal; thus filtering by a lock-in amplifier could not reject its presence.

The differential spectrophone which appears in Figure 2 was designed with the intention of eliminating that portion of the false pressure signal caused by the absorption of incident radiation by the IR windows. In order to accomplish this objective, two chambers of different lengths but equal volumes were joined together. The principle employed is that, when the instrument contains an inert sample gas, the pressure rise produced by the windows in each chamber will appear as equal signals (in magnitude and phase) on opposite sides of the pressure sensor (acting in a differential mode). This should then produce a null signal out of the DCM (trade name Barocel) assuming the heating effects at all three windows are identical.

When an absorbing gas sample is being measured, the pressure signal in cells A and B will consist of two parts -- that due to the windows and that due to molecular absorption by the gas. Assuming that all windows and both volumes are equal, the window signal will be equal in both chambers and therefore cancel. Because the radiation energy absorbed by the gas is proportional to path length, the absorber signal will be greater in cell A than in cell B. Thus, the response of this instrument is roughly equivalent to that of a conventional spectrophone whose length is equal to the difference between that of cell A and cell B with the important difference being that there will be no false window signal.

Because one is interested in measuring pressure variations on the order of  $10^{-3}$  -  $10^{-6}$  torr, it is necessary to equalize the static pressure across the DCM to within its working range (approximately 0.01 torr). By employing a micro-metering (leak) valve (see Figure 2) between the two chambers, this balance is achieved without any adjustments to system parameters, i.e., cell volume.

## CHAPTER II

### THE EXPERIMENTAL APPARATUS

#### A. Introduction

The absorption coefficient of a gas sample can be obtained from a spectrophone measurement by simply taking the ratio of the pressure signal to the incident radiation (laser) power and multiplying by a predetermined calibration constant [5]. Because the pressure signal varies linearly with laser power, it is essential that the two be compared at the same time or that the laser power remain relatively constant during a measurement. Although the time constant of the DCM signal processing electronics was adjusted to match that of the laser power meter ( $\approx 4$  sec), the method of data acquisition employed here precluded a simultaneous comparison of the two signals. Thus it was necessary to build a radiation source whose output varied slowly with time. The stabilized, grating tunable, CO<sub>2</sub> laser which resulted will be described in section B of this chapter.

The differential spectrophone which appears in Figure 2 served as the prototype for this study which was undertaken to investigate certain problems that had previously been encountered [9]. As a result, several physical improvements were made on this instrument in an effort to eliminate these problems which will be discussed in Chapter III. The Brewster angle differential spectrophone that was ultimately developed will be described in section C.

Section D contains a description of the electronics and transducers utilized in this study. Included here is a brief analysis of the signal processing which was performed by a lock-in amplifier on the analog signal from the electronic manometer. This discussion will have significance when the topic of kinetic cooling is considered in Chapter III.

#### B. The Stabilized CO<sub>2</sub> Laser

The source of radiation used to perform measurements with the spectrophone was a frequency stabilized, grating tunable, sealed

off CO<sub>2</sub> gas laser. This laser operates at a nominal power level of two watts in the TEM<sub>00</sub> mode on the P(20) line of the 10  $\mu$  band. The important feature is the stability of the output power which was observed to remain constant within  $\pm 0.25\%$  over several minutes as measured with a Sciencetech disc calorimeter, Model 3600.

Following construction, the Pyrex plasma tube was chemically cleaned and subsequently outgassed using a high vacuum diffusion pump in conjunction with an infrared heat lamp. The tube was then filled with CO<sub>2</sub>, N<sub>2</sub>, He, Xe, and H<sub>2</sub> using the manifold shown in Figure 3. It was necessary to refill the plasma tube every few days, as the laser power was gradually degraded by unknown contaminants. A roughing pump (see Figure 3) was used to evacuate the laser to a pressure of approximately 20 microns, after which the tube was refilled. Following this procedure, the laser output returned to the desired level.

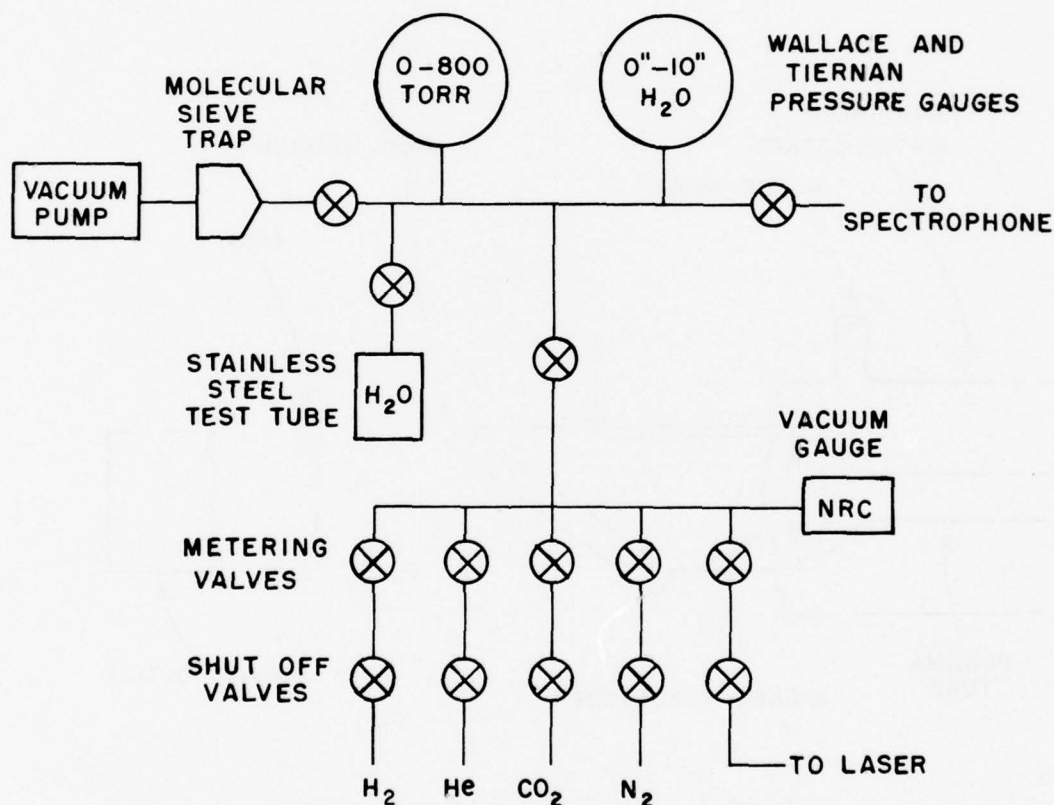


Figure 3. Manifold.

The optical cavity consists of a plane grating, to allow single line operation, and a spherical output mirror. The aluminum grating is blazed at  $26^{\circ} 45'$  and ruled with 150 grooves per millimeter. The germanium output mirror is 20% transmitting and has a 10 meter radius. The mirror is attached to a piezoelectric crystal, PZT, to provide both manual and electronic tuning of the cavity length; the latter function will be discussed in subsequent paragraphs.

To limit lasing action to the  $TEM_{00}$  mode, irises are located internally at each end of the laser cavity. High purity nickel electrodes and a regulated and filtered d.c. power source are used to excite the plasma. The electrodes, see Figure 4, are shaped in the form of a semi-closed circular band, which is located within the cooling zone of the plasma tube. Sodium chloride windows, 3 mm thick, are mounted at the Brewster angle on both ends of the plasma tube.

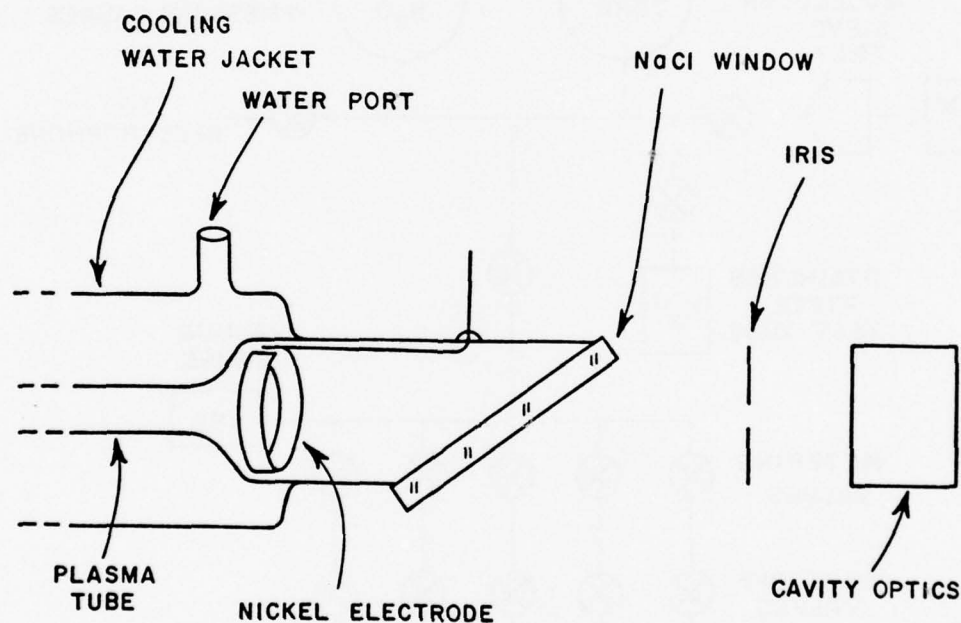


Figure 4.  $CO_2$  laser tube and optics.



Electronic tuning of the cavity length is accomplished by a frequency stabilizer which is electrically connected to the PZT. The stabilizer design was adapted from one that Thomason and Elbers [10] used with a commercial laser. In operation, the stabilizer periodically varies the cavity length a small distance which causes a small modulation in the laser's output power, when operating above threshold. This variation in output power simultaneously produces oscillations in the plasma impedance which are synchronously detected by the stabilizer. This signal is then used to create a control voltage which is "added" to a manually adjusted PZT bias voltage.

The impedance of the CO<sub>2</sub> laser plasma varies inversely with gain. By sensing changes in plasma impedance, it is possible to maintain laser operation at line center (maximum gain) by adjusting the cavity length to continuously minimize impedance. The stabilizer correction signal is derived by integrating the output of the synchronously detected variations in plasma impedance induced by a 520 Hz voltage applied to the PZT. The integrated signal is then amplified and "added" to the PZT bias voltage so as to adjust the optical cavity length to obtain a minimum error (plasma impedance) signal and thus maintain maximum gain.

### C. The Differential Spectrophone

The instrument which will be described here was derived from modifications performed on the prototype device which is shown in Figure 2. The essential difference between the original and modified version, schematically displayed in Figure 5, is the mounting of the three IR windows at the Brewster angle. This was accomplished by vacuum sealing three NaCl windows on aluminum adapters which were machined to the appropriate angle. An equally important modification was to correct the volume of cell B', to achieve equal volumes on both sides of the center window. The final modification eliminated a mechanical plunger which had been incorporated into the design of cell B' which was to be used for small volume adjustments. This was eliminated to prevent any future variations in the cell volume and to insure a vacuum-tight instrument.

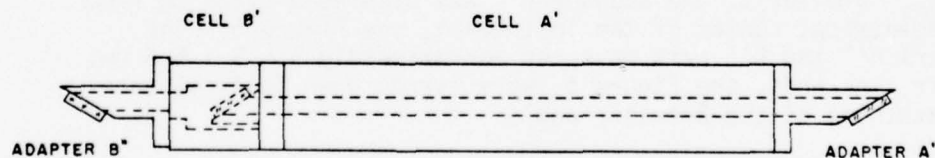


Figure 5. Brewster angle differential spectrophone.



The long and short cavities of the spectrophone were machined from aluminum, as were the three Brewster angle window adapters. The NaCl windows were cemented onto the adapters with a low vapor pressure sealant, trade name "Torr Seal", which is specifically intended for vacuum applications. Vacuum integrity of the assembled instrument was achieved by Viton "O" rings which were installed between each of the separate sections. External plumbing, see Figure 2, was composed of bellows sealed vacuum valves connected by #304 stainless steel tubing using #316 stainless steel fittings, trade name "Swagelok."

The cell A' measures approximately 5 x 5 x 30 cm and includes a 30 cm long hole thru the center of the cell which was reamed and polished to a final diameter of 1.031 cm. "O" ring grooves 1.588 cm in diameter were cut at each end and a 0.318 cm hole, running perpendicular to but not penetrating the 1.031 cm bore, was drilled near the center of the chamber to accommodate the temperature sensor. The volume of the long chamber which includes that of cell A' and several short sections of 0.64 cm diameter tubing, see Figure 2, measured approximately 38 cc as did the modified short chamber.

The short cell, B' shown in Figure 6, measures approximately 5 x 5 x 7.62 cm and as can be seen is somewhat complex compared to cell A'. This cell offers a relatively short path for the incident beam but with the compensating volume B''' comprises a volume equal to that of the long chamber. The compensator B''' was originally designed to incorporate a small mechanical plunger within the cavity in order to permit small volume adjustments. It was originally theorized that a small adjustment in the volume of cell B could be performed which would allow complete cancellation of the false window signal. This was never realized in the spectrophone of Figure 2 for reasons which will be discussed in Chapter III. The compensator B''' was modified, i.e., the original hole was enlarged and undercut, to increase the cell volume. Also the end was threaded for use with a stainless steel fitting, which was used to vacuum seal the chamber.

The hole B'-B' of the cell B' was enlarged to allow for the refraction of the laser beam caused by the 5 mm x 25 mm NaCl windows. Similarly, the adapter B'' was displaced 0.229 cm from the geometrical center of the instrument, see Figure 5. The adapters A'' and B'' both measured approximately 5 x 5 x 6.5 cm; however, the ends, see Figure 5, were turned down to facilitate the machining of the Brewster angle.

The spectrophone which appears in Figure 5 is the instrument that was employed for the final tests and measurements which are described in Chapter III.

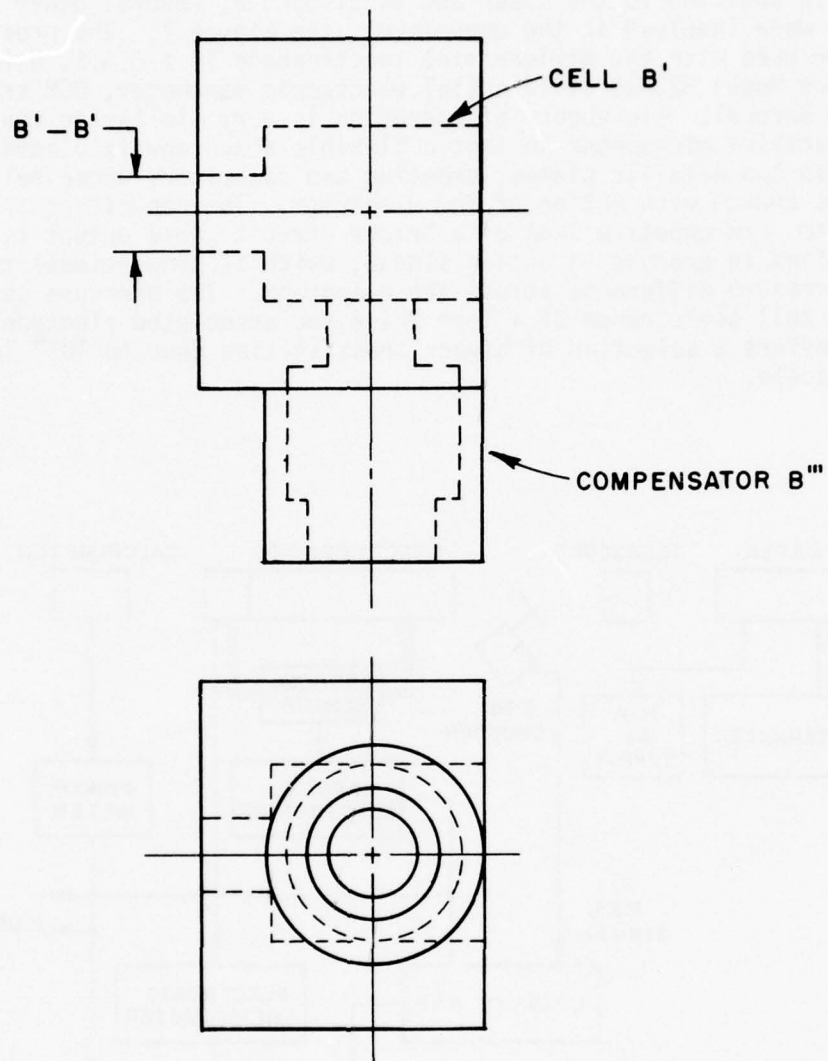


Figure 6. Short cell.

## D. Accessory Equipment

### 1. The Electronic Apparatus

In addition to the laser and spectrophone, several other instruments were involved in the experiment, see Figure 7. The pressure sensor used with the differential spectrophone is a C.G.S. Data-metrics Model 523-15 differential electronic manometer, DCM trade named Barocel. Its theory of operation is very similar to that of a capacitive microphone in that a flexible diaphragm is placed between two metallic plates, creating two capacitors whose relative values change with motion of the diaphragm. The capacitors are used to form opposite legs of a bridge circuit whose output is amplified to produce an analog signal, which is proportional to the pressure difference across the diaphragm. The pressure sensor has a full scale range of 1 Torr while the associated electronic unit offers a selection of higher sensitivities down to  $10^{-4}$  Torr full scale.

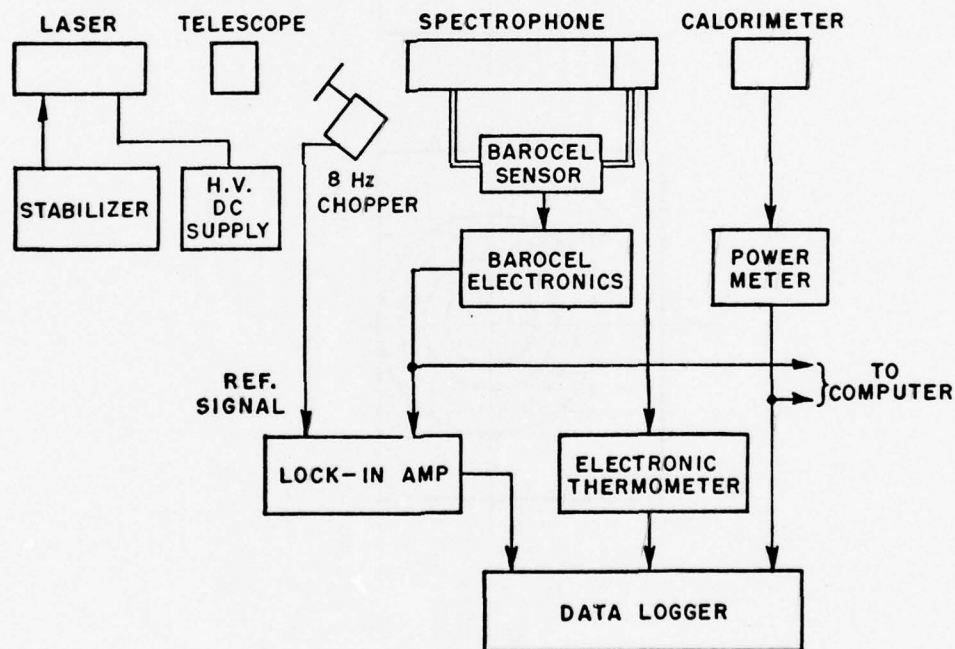


Figure 7. Experimental apparatus.

The pressure signal is processed by a lock-in amplifier, Princeton Applied Research Corporation Model 128 A, which synchronously detects and integrates the pressure signal. The reference signal for the lock-in amplifier is obtained from an infrared diode-photo transistor pair that is mounted on the mechanical chopper. The chopper, which employs a synchronous 240 rpm motor and a stainless steel blade, provided 100% modulation of the laser beam at a frequency of 8 Hz. This frequency was selected in order to limit the problems of d.c. drift while maintaining a good signal-to-noise ratio for the pressure signal.

The laser power was monitored by a disc calorimeter, Scientech Model 3600, which when used with its associated power meter has a time constant of 4 seconds. Thus, the laser power readings were not affected by the 8 Hz modulation, except that half the power was lost by chopping.

Because of the significant temperature dependence in the absorption coefficient for CO<sub>2</sub> gas samples, it was necessary to continuously monitor the temperature of the spectrophone. An electronic thermometer, Stow Laboratories, Inc. Model 911 PL, was employed for this purpose, with its sensor located in the body of the long chamber.

The raw data which included the integrated pressure signal, laser power, temperature, and the time of day were recorded by a United System Corp. Model 1267 data logger. The outputs of the pressure transducer and power meter were also interfaced to a digital computer, see Figure 7. This capability was employed to determine the response of the Barocel pressure sensor and the shape of the pressure signal.

## 2. Pressure Signal Processing

The pressure signal that was obtained from the Barocel electronic manometer was fed into the lock-in amplifier, which was used to determine both the magnitude and phase of that signal. The purpose of this section is to clarify the manner in which this was accomplished; its application and importance will be discussed in Chapter III.

As was previously mentioned, the reference frequency signal was derived from a photo diode-transistor pair located on the mechanical chopper. The output of the photo transistor was a square wave voltage that went high while the chopper blade was passing in front of the diode and low otherwise. In order to have a well defined phase reference the motor-chopper assembly was positioned so that its signal was going high as the laser radiation became incident on the spectrophone cell.

Figure 8 shows an oscilloscope trace of the relevant signals; the square wave is the reference signal while the second trace is the output of a pyroelectric detector which senses laser power passing thru the spectrophone cavity. If one ignores the response time of the pyroelectric detector, the two signals are seen to be in phase. Thus, the phase lag and/or time delays which will be discussed in the following paragraphs and chapters may be taken equivalently with respect to either the reference signal or laser beam incidence.

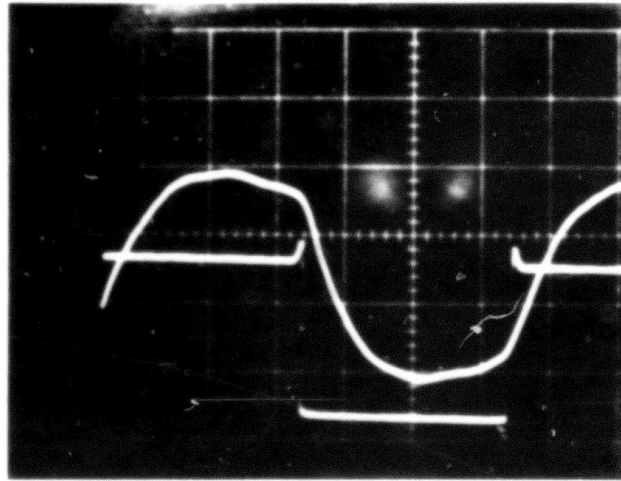


Figure 8. Laser power and chopper reference signals.

The lock-in amplifier acts as a synchronous detector which will filter input signals whose frequencies are not identical to that of a reference signal. Figure 9 will be used to analyze the manner in which the input signal is processed. The square wave at the top of Figure 9 (a) represents the laser power signal, while the waveform below it, 9 (b), shows the plot of an arbitrary "ideal" (no time delays) pressure signal. The lock-in amplifier convolves the pressure signal with an internally generated square wave having a fundamental frequency equal to that of the reference signal, see graph 9 (c). The particular square wave shown in graph 9 (c) is phased in such a manner that the output will have a maximum non-zero value after a time average integration is performed.



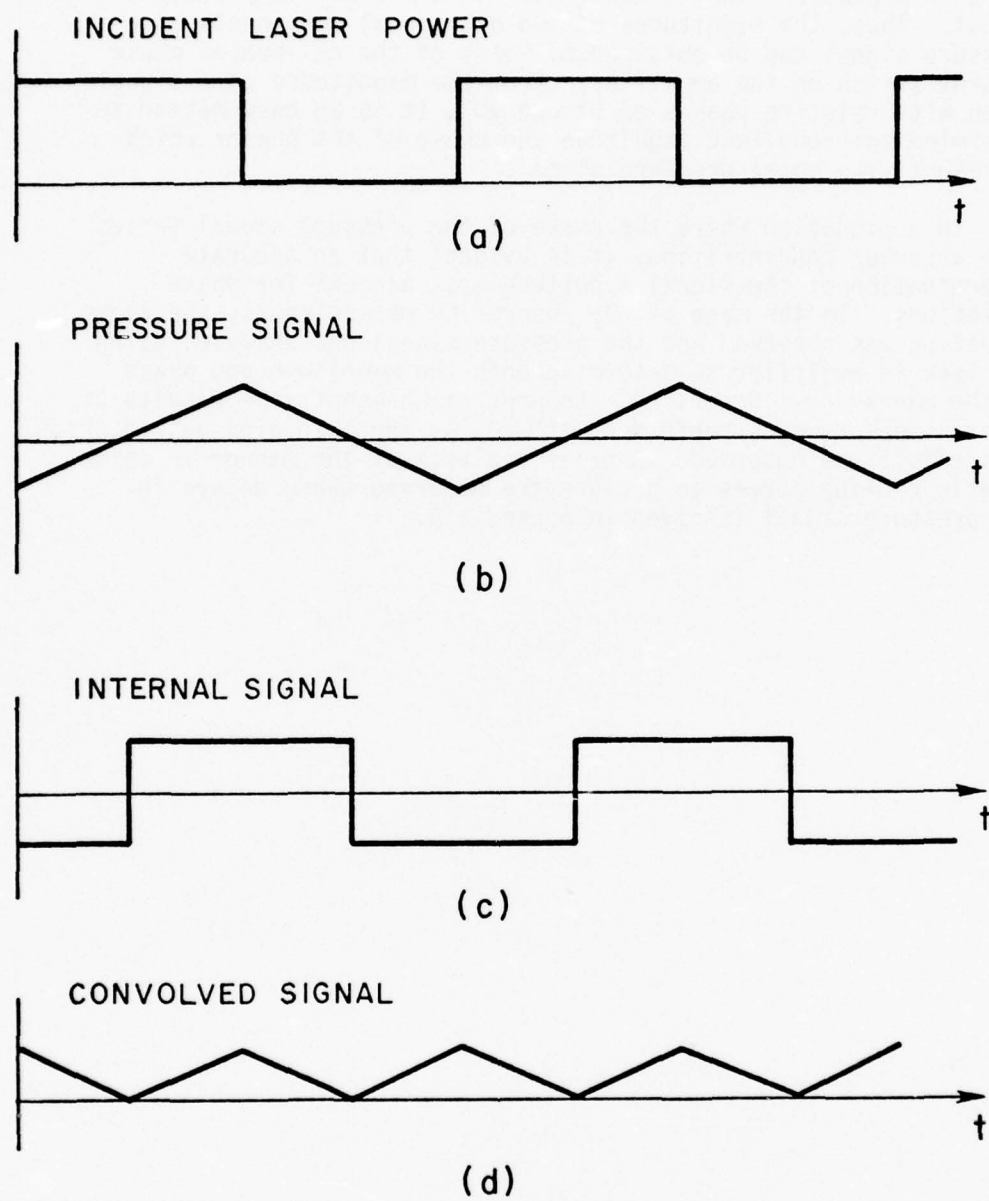


Figure 9. Analysis of pressure signal processing.

The lock-in amplifier allows the user to choose the relative phase (with respect to the reference signal) of the internal square wave. The one displayed in graph 9 (c) is defined to have a phase of  $90^\circ$ . It is easy to show that a phase of  $0^\circ$  or  $180^\circ$  for this pressure signal would result in a minimum time average signal. Thus, the magnitudes of two orthogonal components of a pressure signal can be obtained by means of the calibrated phase control switch on the amplifier. From the magnitudes of a signal taken with relative phases of  $0^\circ$  and  $90^\circ$ , it is an easy matter to determine the resultant magnitude and phase of the phasor which represents the total pressure signal.

In a situation where the phase of the pressure signal varies with absorber concentration, it is evident that an accurate determination of the signal magnitude must account for phase variations. In the case of  $\text{CO}_2$  absorption measurements, the above situation was observed and the pressure signal was analyzed using the lock-in amplifier to determine both the magnitude and phase in the manner just described. Chapter III presents the results of several measurements performed with  $\text{CO}_2$  as the absorbing gas in which this effect was observed. A brief analysis of the manner in which kinetic cooling serves to produce the observed phase delays in the pressure signal is given in Appendix A.

## CHAPTER III

### TEST MEASUREMENTS AND RESULTS

#### A. Introduction

There should be no background window signal observed with the differential spectrophone and its response for an absorbing sample must be proportional to the difference in length between the long and short chambers. Attempts to measure the differential effect raises two fundamental questions.

- (1) Are there any other background sources which could serve to mask the window signal?
- (2) Can the pressure signals in each cell be measured independently?

Associated with these questions is the influence on the instrument response of cell volumes and the laser beam trajectory. These questions together with test measurements performed on the prototype and modified versions of the differential spectrophone are considered in section B of this chapter.

Having demonstrated that the Brewster angle differential spectrophone, shown in Figure 5, performed as required, a series of measurements with CO<sub>2</sub> in air and selected measurements of H<sub>2</sub>O in N<sub>2</sub> were undertaken to demonstrate the performance of the instrument. The experimental procedures are outlined in section C while the results which were obtained are given in section D. Also considered in section D is the kinetic cooling that was observed in the measurements of CO<sub>2</sub> in air. A more detailed description of kinetic cooling appears in Appendix A.

#### B. Test Measurements

The experimental analysis of the differential spectrophone consists of two parts:

- (1) a demonstration of sensitivity, and
- (2) a demonstration of linearity.

The sensitivity of the conventional spectrophone is limited by a false pressure signal which is generally attributed to the end windows. The advantage offered by the differential instrument is the increased sensitivity which can be obtained by eliminating this unwanted signal. This does not necessarily mean that all background signals will be eliminated, but it is expected that there will be a major improvement.

When measuring an inert sample gas, the proper operation of the differential spectrophone is indicated by equal pressure signals in cells A and B, see Figure 2, and therefore no net signal should be observed from the pressure transducer. This theory tacitly assumes that all three windows are "identical," a stipulation which is difficult if not impossible to predetermine. Hence, when filled with an inert sample, this instrument functions as a window tester. A valid criterion for proper operation of the differential spectrophone is the inability to distinguish, by means of the pressure signal, the presence or absence of laser radiation thru the instrument. This requirement satisfies an intuitive understanding of the desired objective but there are other factors which need to be considered because of their influence on background as well as absorber measurements.

The initial experimental efforts in studying background levels were performed with the prototype differential spectrophone of Figure 2 using the physical arrangement shown schematically in Figure 10. The results of this investigation showed that

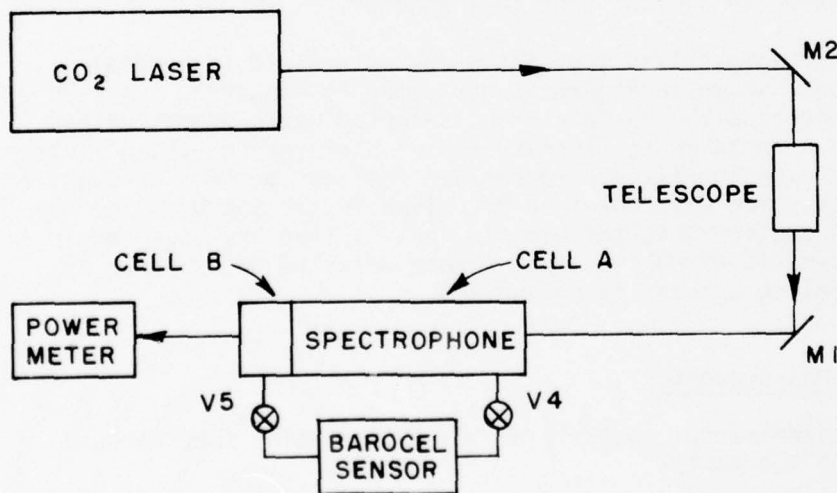


Figure 10. Schematic of experimental optics.



small changes in beam trajectory, caused by fine adjustments to mirror M1, had a dramatic influence on the magnitude and sign of the recorded pressure signal. Figure 11 shows the process by which the lock-in amplifier was used to determine whether the pressure signal from the spectrophone is positive or negative. Depicted in graphs 11 (b) and 11 (c) are the ideal pressure signals which would be independently observed from cells A and B, respectively. Graphs 11 (e) and 11 (f) indicate the convolved signals which are internally generated by the lock-in amplifier and subsequently processed using a time-average integration. Since the pressure transducer actually superimposes these two signals, the sign of the output from the lock-in amplifier is determined by the relative magnitude of the signals which appear in graphs 11 (b) and 11 (c). For convenience, the Barocel sensor was installed so that a pressure rise in cell A would cause a positive signal out of the lock-in amplifier; hence by observing the sign of the resultant pressure signal, it is possible to determine which cell is the source of the dominant background signal.

By making small adjustments of mirror M1, it was determined that the background pressure signal could be eliminated or continuously varied in either the positive or negative directions. However, these adjustments were of such a critical nature that they led to severe stability problems which caused both background and absorption measurements to lack repeatability from day to day. The critical alignment procedure which influenced the false pressure signal also affected the signal observed from an absorbing gas sample. By employing the above technique with the instrument shown in Figure 2, it was possible to realize the desired objective, i.e., eliminating the background signal but not without observing what was felt to be a more serious limitation.

At the same time, a periodic (8 Hz) instability in the CO<sub>2</sub> laser was observed which also appeared to be dependent upon the adjustments performed on mirror M1. The radiation which was reflected from the windows of the spectrophone was apparently sufficient to create measurable optical feedback which disturbed the operation of the laser. By employing infrared thermal screens and slowly adjusting mirror M1, it was possible to observe radiation reflected from each of the three windows, as well as multiple reflections from the cell walls.

Due to machining imperfections, the three windows were not quite parallel, hence the reflected radiation seldom traveled a direct path out of the spectrophone. As a result, the changes in beam trajectory which were initiated at mirror M1 not only influenced the ray path of the incident radiation but also the number of reflections inside the instrument and therefore, the radiation absorbed by the walls and windows. If the windows had been parallel, the possibility of etalon effects would have existed between the eight



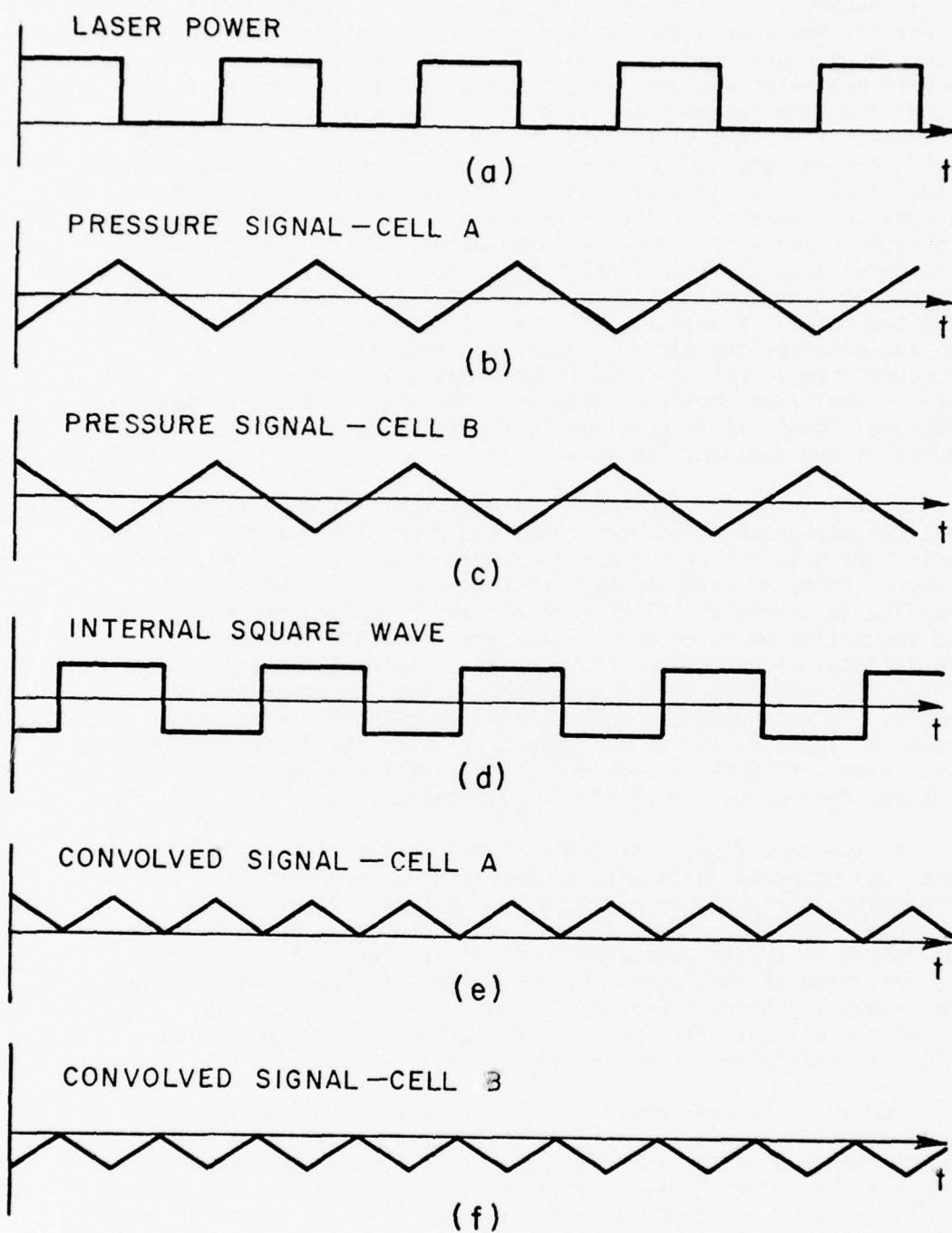


Figure 11. Analysis of background pressure signals.

window surfaces. This could have added an additional frequency dependent phenomenon to the previously mentioned difficulties. (In the past, it was felt that spectrophone calibration was necessary at each frequency to be considered.)

The solution to these problems was the construction of the differential spectrophone shown in Figure 5, with all three IR windows at the Brewster angle. This instrument had no observable reflections from the windows and the laser instabilities which had previously been encountered were no longer observed. More importantly, the criterion for proper operation of the instrument was achieved without any fine adjustments to the optical alignment. The nulling of the window signal was simply obtained by aligning the laser beam with the optical axis of the spectrophone; further, the resulting signals for inert or absorbing samples were not affected by small changes in this optical alignment.

The linearity of the differential spectrophone was demonstrated by examining the instrument response versus absorber concentration. This is presented in Figures 14 through 22, where the ordinate is a ratio of the pressure signal to laser power and the abscissa is the absorber concentration. From these figures, it is observed that the response of the instrument does appear to be linear.

Equivalently, one might consider measuring the pressure signals in the two cells, A' and B', of the modified instrument, see Figure 5, and demonstrate that the superimposed response is equal to the difference between the individual signals. Referring to Figure 10, it can be seen that it is possible to independently observe the pressure response produced in cell A (B) by closing valve V<sub>5</sub> (V<sub>4</sub>). However, it should be realized that the system response is fundamentally changed while either of these valves, V<sub>4</sub> or V<sub>5</sub>, is closed.

When a pressure rise occurs on one side of the pressure sensor, its diaphragm deforms (approximately 0.05 mm/Torr) and compresses the reference volume until equilibrium is achieved. This causes the transducer response to be a function of not only the deflection characteristics of the diaphragm but also the relevant volumes, and requires that the reference volumes "seen" by the DCM remain unchanged if comparable results are to be obtained. Because the instrument linearity was more easily and accurately established by the previous method, this last technique was never seriously attempted. However, it is interesting to examine the influence which a volume change exerts on the system response.

Figure 12 shows the results of measurements that were performed with the Brewster angle differential spectrophone using  $\text{CO}_2$  in air as the absorbing gas and the P(16) line in the  $10\ \mu$  region as a radiation source. The solid line indicates the results of measurements performed with the unmodified instrument, the dashed line represents the data obtained by adding approximately 10 cc of external volume to chamber B' of the spectrophone. It is clear from these results that the pressure signal was significantly increased as a result of this change; however the null in the background signal obtained by machining equal volumes in the original instrument was sacrificed.

### C. Experimental Procedure

The most serious problem encountered in using the spectrophone as a spectroscopic tool for measuring small absorption is contaminants. In order to minimize this problem (it was never eliminated), the spectrophone and its associated vacuum system were outgassed using heating tape and a Vacuon pump. The ultimate vacuum achieved was approximately  $10^{-7}$  Torr at a temperature of  $52^\circ\text{C}$  (measurements were performed near  $23^\circ\text{C}$ ). A mass spectrometer was connected to the vacuum system but the results obtained were inconclusive.

Gas samples were introduced using the manifold and pressure gauges shown in Figure 3. In order to minimize backstreaming, a molecular sieve trap was mounted on the roughing pump which was used to remove gas samples between measurements. The  $\text{CO}_2$  in air samples were obtained from Primary Standard gas cylinders containing 1.0%, 0.2 %, 0.1 %, and 0.04%  $\text{CO}_2$  in air. Concentrations of  $\text{CO}_2$  near 0.5%, which were also measured, were obtained by mixing the 1% sample gas with one of the smaller concentration samples. This dilution was accomplished by introducing equal amounts of the two gas samples into the spectrophone plumbing system and mixing for five minutes with a circulation pump, see Figure 13.

Water vapor samples were introduced from a Pyrex test tube containing double distilled  $\text{H}_2\text{O}$ . Before  $\text{H}_2\text{O}$  was introduced into the spectrophone, the test tube was partially evacuated in an attempt to remove any other remaining gases, see Figure 3. The water vapor sample container was then opened to the evacuated spectrophone cell until the desired partial pressure was obtained, after which  $\text{N}_2$  was added until a total pressure of 760 Torr was reached. The sample was then mixed using a circulating pump, see Figure 13, and the water vapor concentration was measured using an EGG dew point hygrometer, model 992-C1. Two one-liter stainless steel sample cylinders were included in the plumbing system in an attempt to increase the system volume-to-surface area ratio and thus reduce condensation in the mixing process. In general, the partial

pressures of H<sub>2</sub>O measured with the dew point hygrometer and the mechanical pressure gauges were in close agreement.

After a sample gas was introduced into the spectrophone, two separate measurements were consecutively performed on that sample. The first measurement was performed with the lock-in amplifier phase control set at 0°, see Figure 9 and the discussion which appears in section D of Chapter II. The second was conducted with the lock-in amplifier phase control switched to 90°. The results of these measurements, divided by the recorded laser power were interpreted as the orthogonal components of the pressure signal and were used to obtain the magnitude and phase of that signal. The absorption coefficient was determined by multiplying this calculated magnitude by a calibration constant which was obtained from White cell measurements.



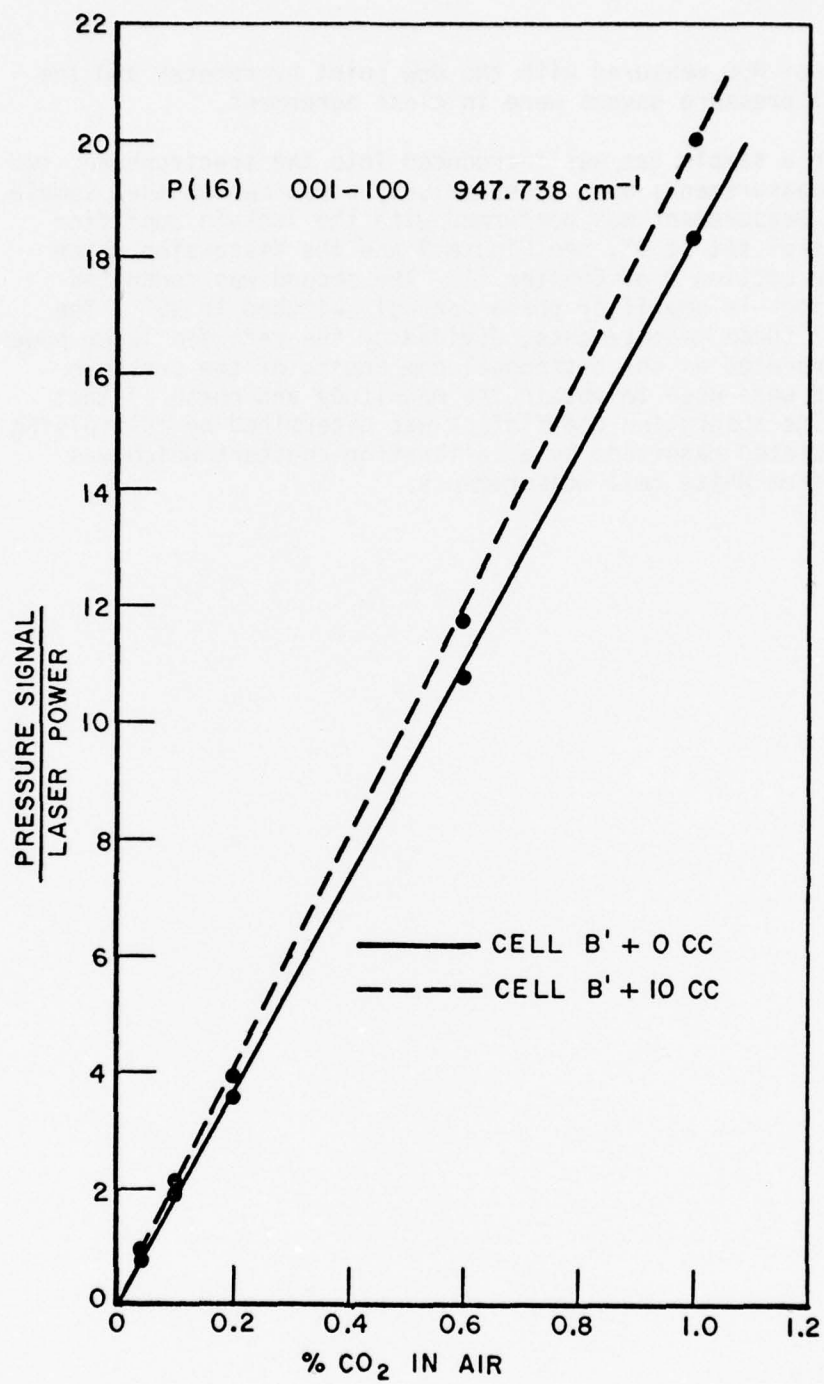


Figure 12. Test for volume dependence.



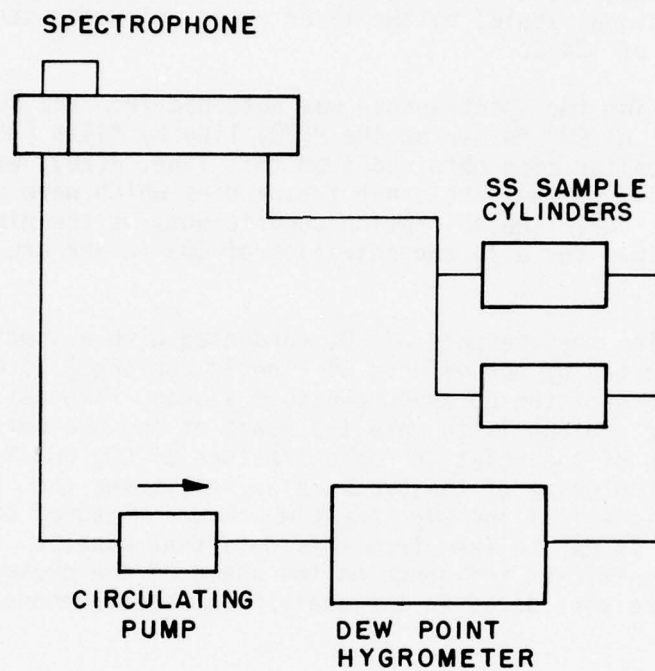


Figure 13. Plumbing for sample gas mixing and dew point measurements.

#### D. Measurements

In order to demonstrate the usefulness of the Brewster angle differential spectrophone, a series of measurements was performed on nine lines, P(12) thru P(28), in the  $10\ \mu$  region with the CO<sub>2</sub> laser that was described in section B of Chapter II. These measurements were performed using varying concentrations of CO<sub>2</sub> in air as the absorbing gas. The results of those measurements are presented in Figures 14 through 22. The data shown in these graphs are given in direct experimental units, i.e., the calculated magnitude of the pressure signal scaled by the laser power and were obtained at a temperature of  $\sim 24^\circ\text{C}$ .

Calibration for the spectrophone was obtained from the White cell measurements of CO<sub>2</sub> in air on the P(20) line by Mills [11], see Figure 23. The calibration obtained from this line, P(20), was assumed to be valid for all the other frequencies which were considered in this study. The absorption coefficients at the nine measured laser lines for a 1% concentration of CO<sub>2</sub> in air are given in Figure 24.

The absorption measurements of CO<sub>2</sub> conducted with a spectrophone are complicated by the effects of kinetic cooling [12] which influence the phase of the observed pressure signal. The net effect of kinetic cooling is to make the phase of the pressure signal a function of the relative concentrations of CO<sub>2</sub> and N<sub>2</sub>. Figure 25 shows the phase of the pressure signal versus the absorption coefficient of the CO<sub>2</sub> sample which was measured on the P(24) line. It can be seen from this data that kinetic cooling has a significant influence on the phase of the pressure signal and must be considered in the analysis of spectrophone CO<sub>2</sub> measurements.

In contrast to the phase dependence observed in the CO<sub>2</sub> data, the phase using water vapor as the absorber remained constant with absorber concentration. This pressure-signal phase is plotted in Figure 26 as a function of absorption; its phase is observed to remain constant, within experimental accuracy. The corresponding data for absorption at the P(20) line versus partial pressure of water vapor is shown in Figure 27.

The measurements presented in Figure 27 are comparable ( $\pm 5\%$ ) to established results [13] but appear slightly high. The data shown in Figure 28 indicate close agreement with the results obtained by Mills [14], which are given by the solid line. The level of absorption being measured here is nearly an order of magnitude greater than that in Figure 27; hence, the contribution of contaminants is less apparent. It is also possible that a frequency dependence is being observed in the contaminant, such that its contribution is smaller for the R(20) line in the  $10\ \mu$  band than the P(20) line.

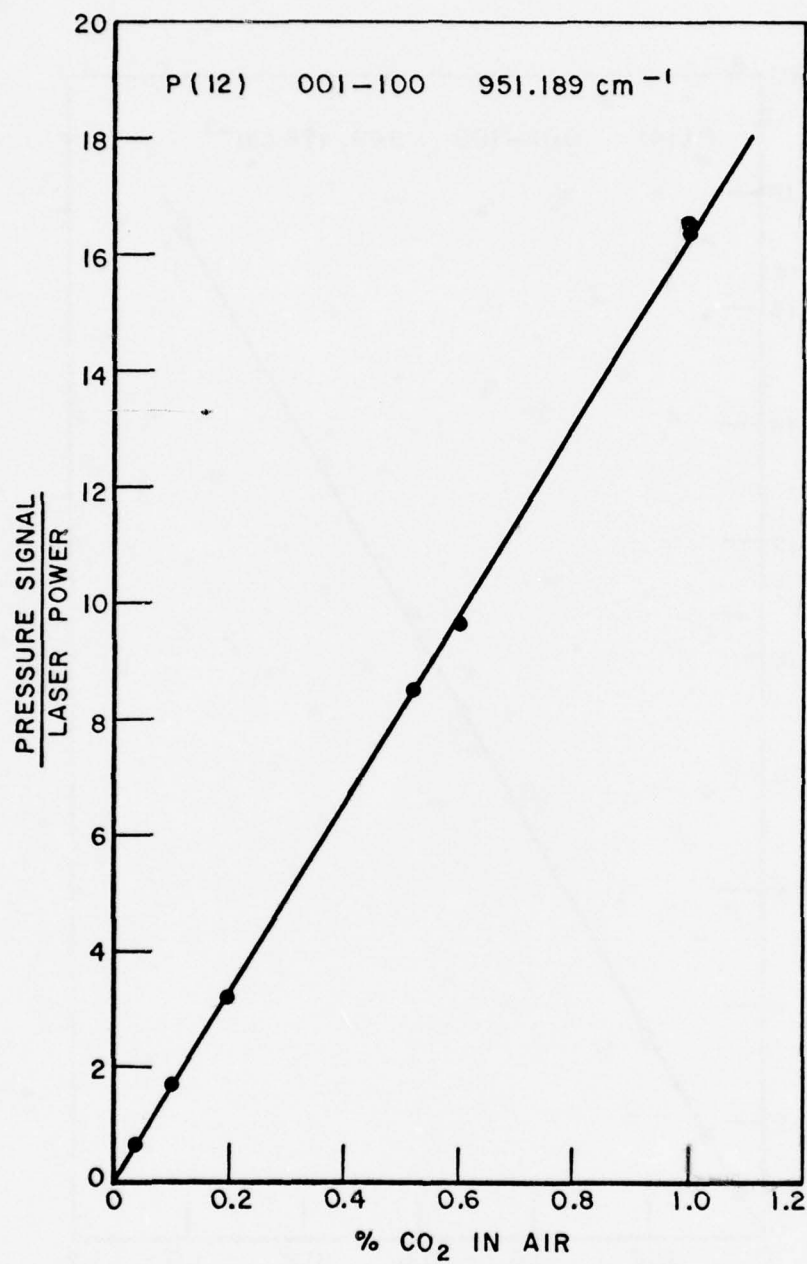


Figure 14. CO<sub>2</sub> in air.

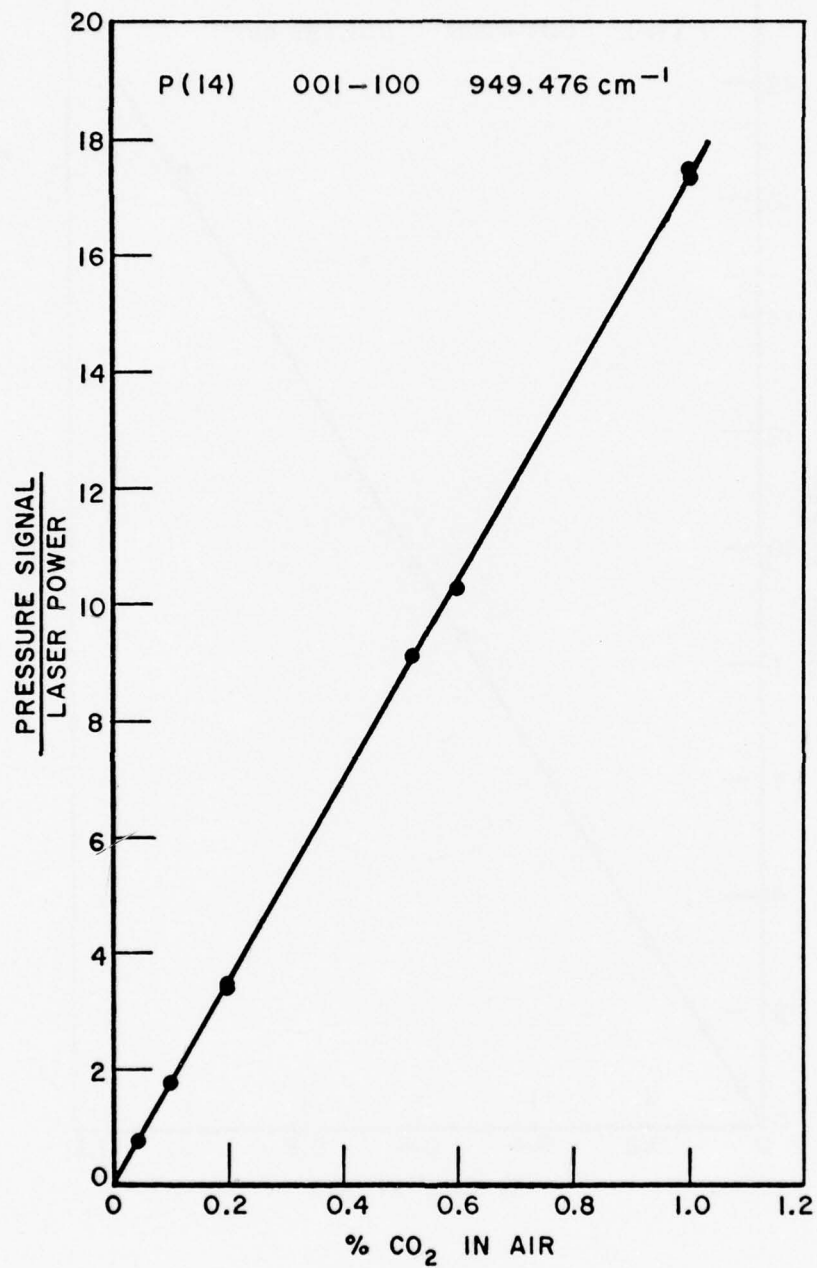


Figure 15. CO<sub>2</sub> in air.

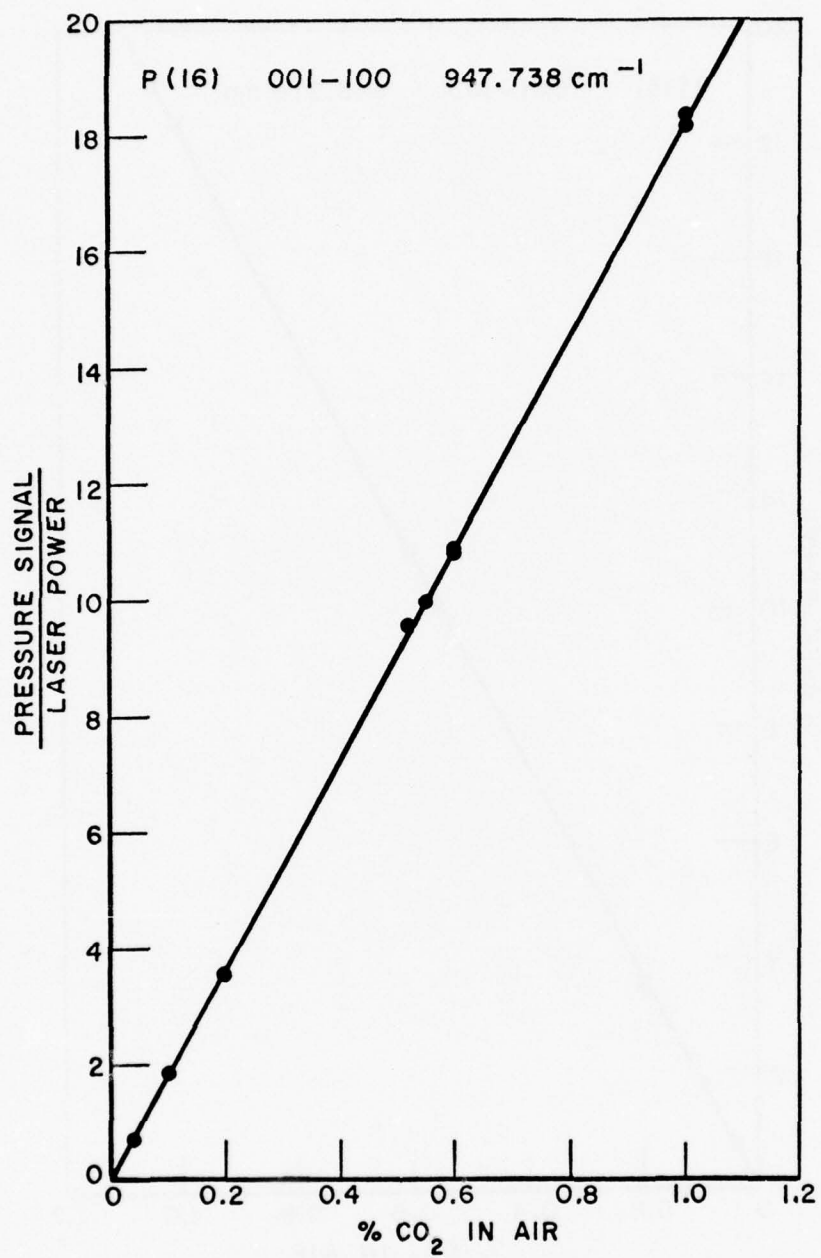


Figure 16. CO<sub>2</sub> in air.



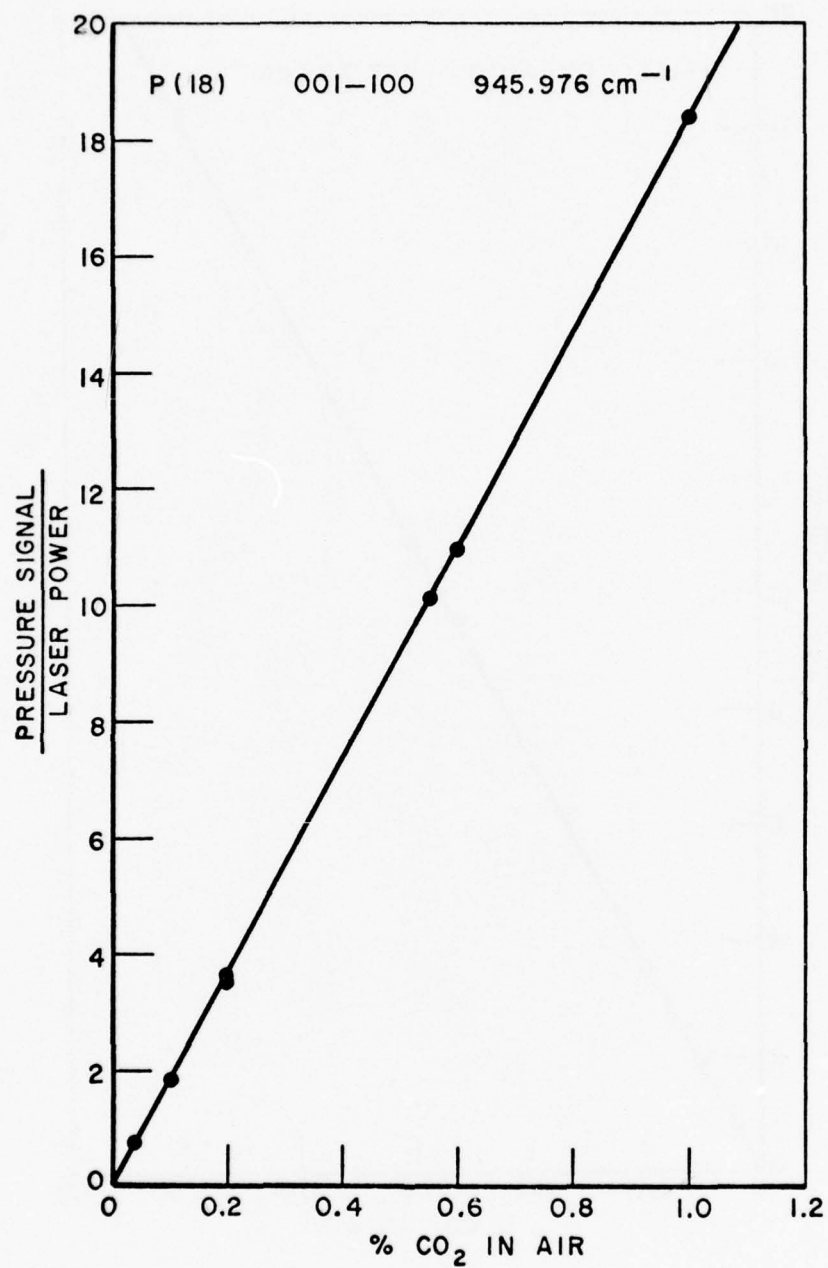


Figure 17. CO<sub>2</sub> in air.

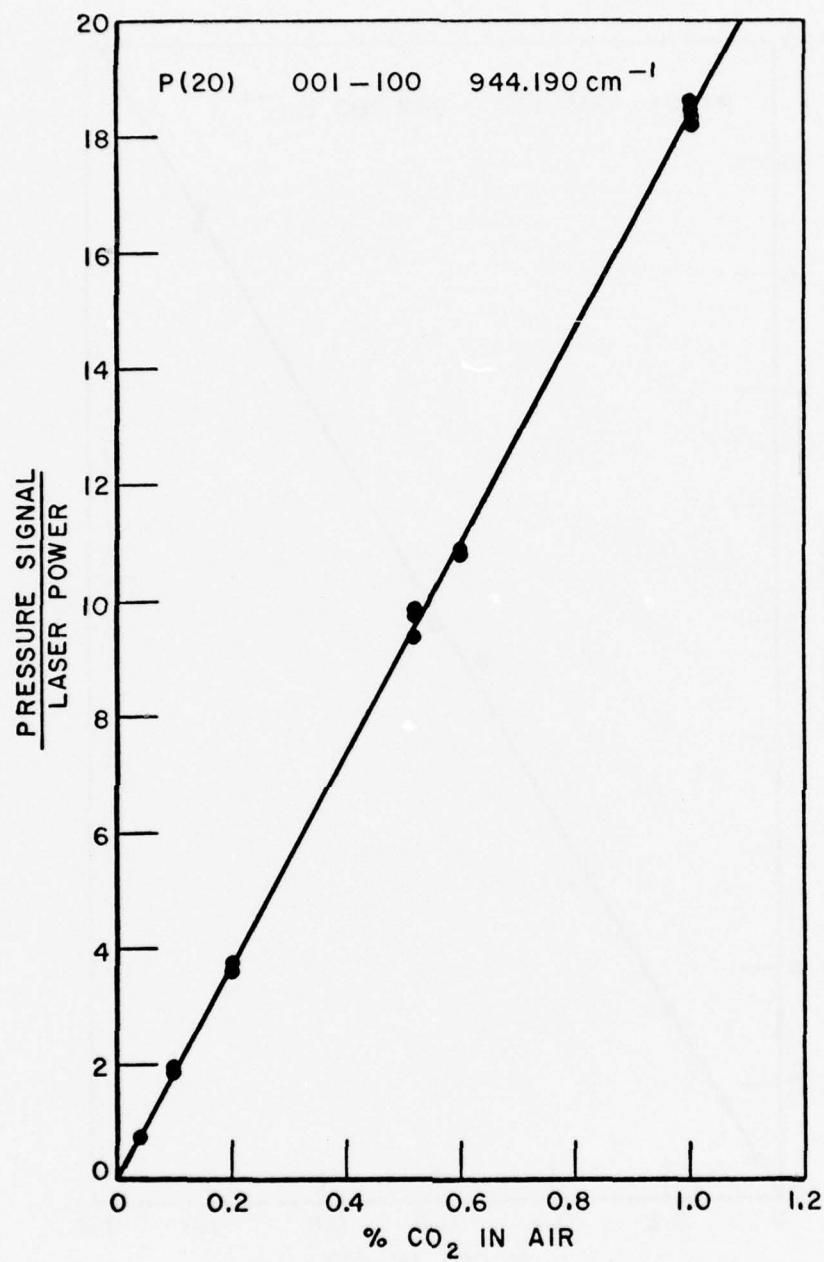


Figure 18. CO<sub>2</sub> in air.

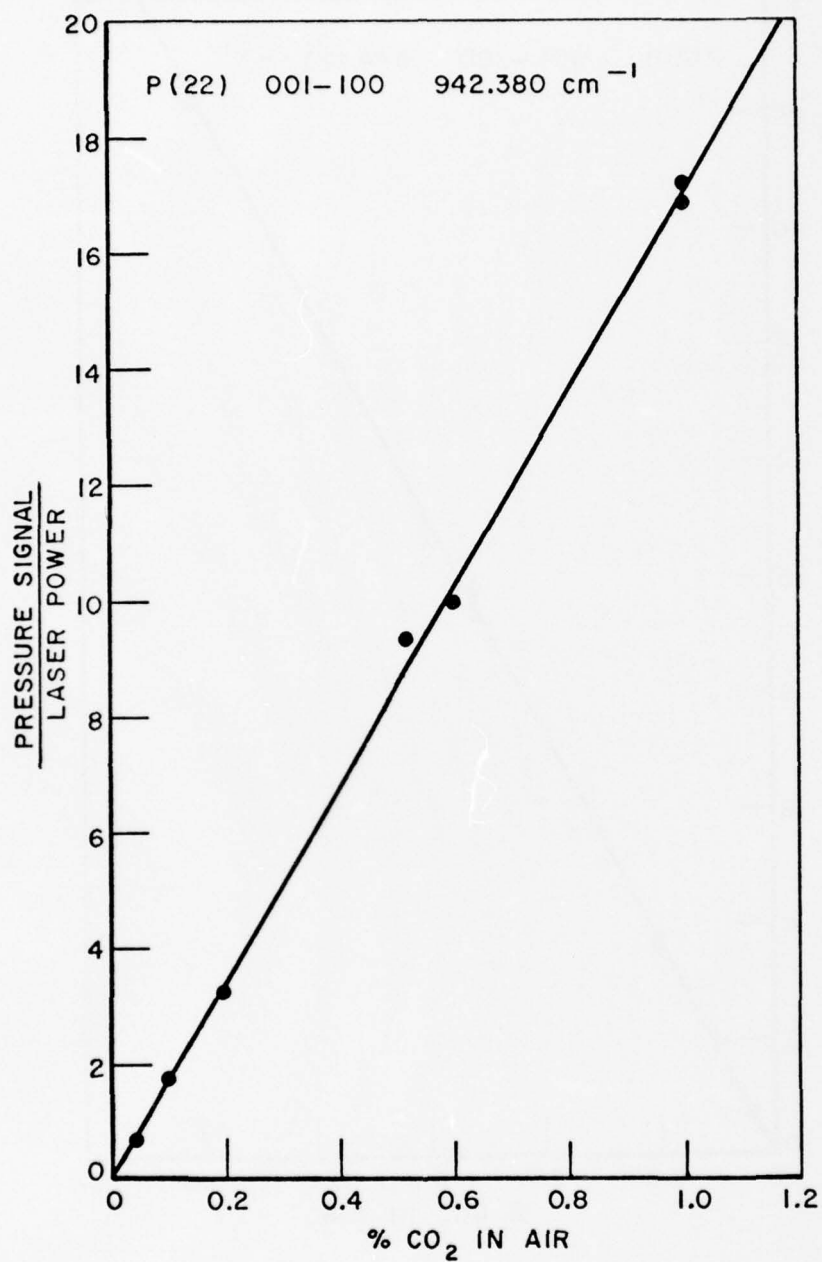


Figure 19. CO<sub>2</sub> in air.

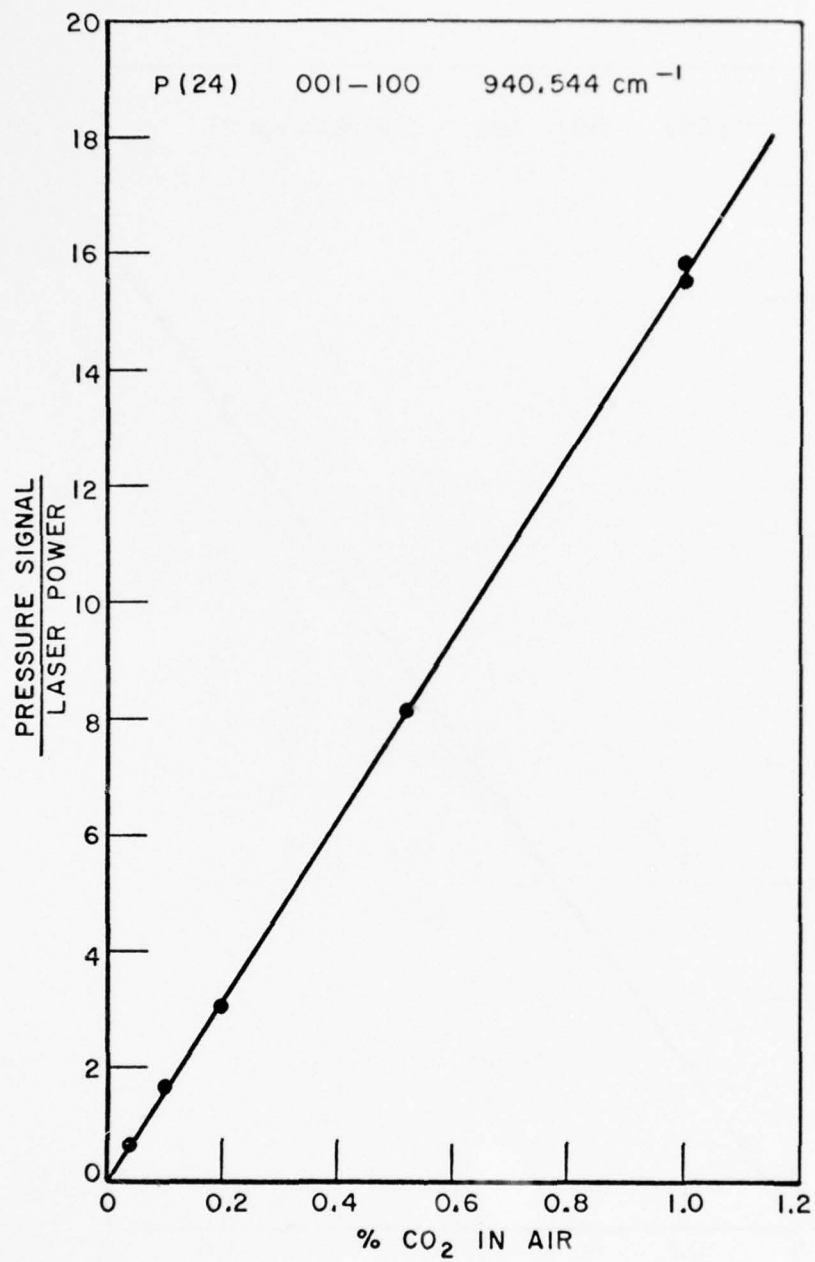


Figure 20. CO<sub>2</sub> in air.

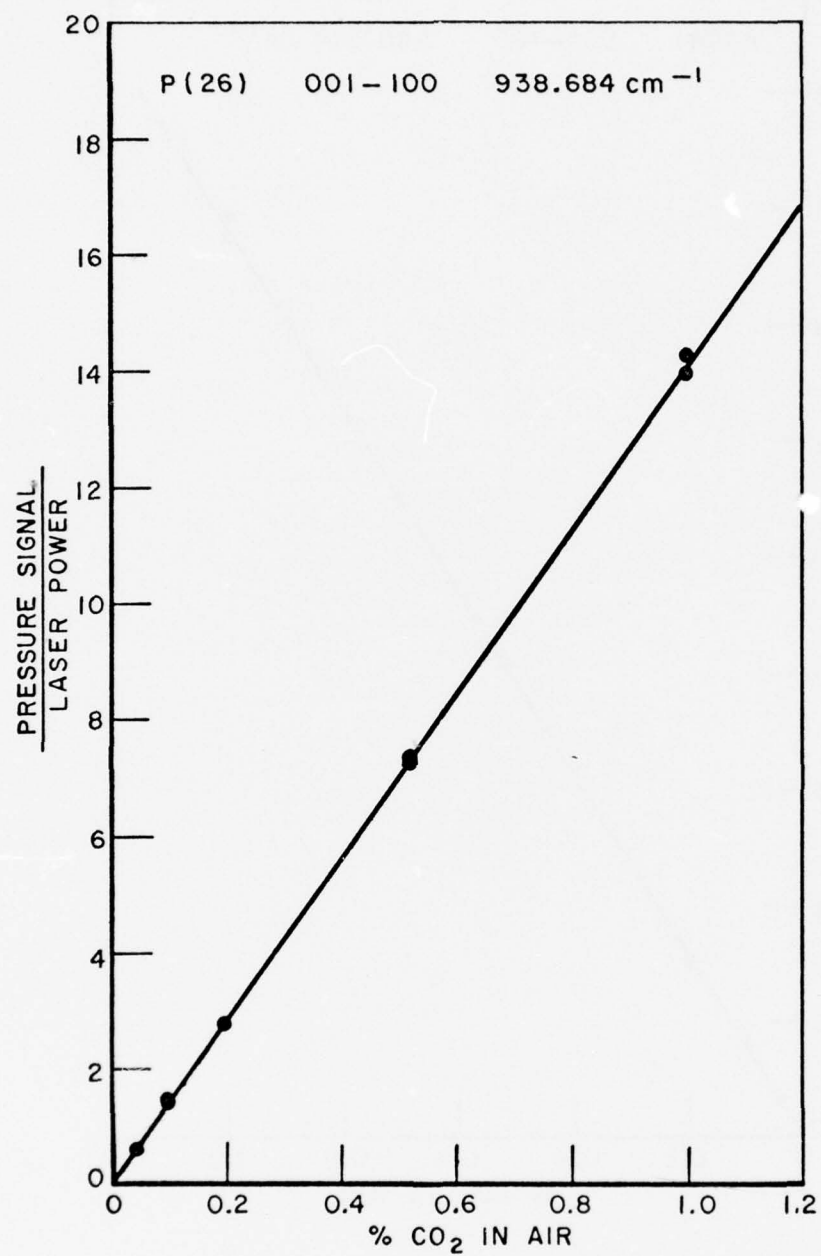


Figure 21. CO<sub>2</sub> in air.



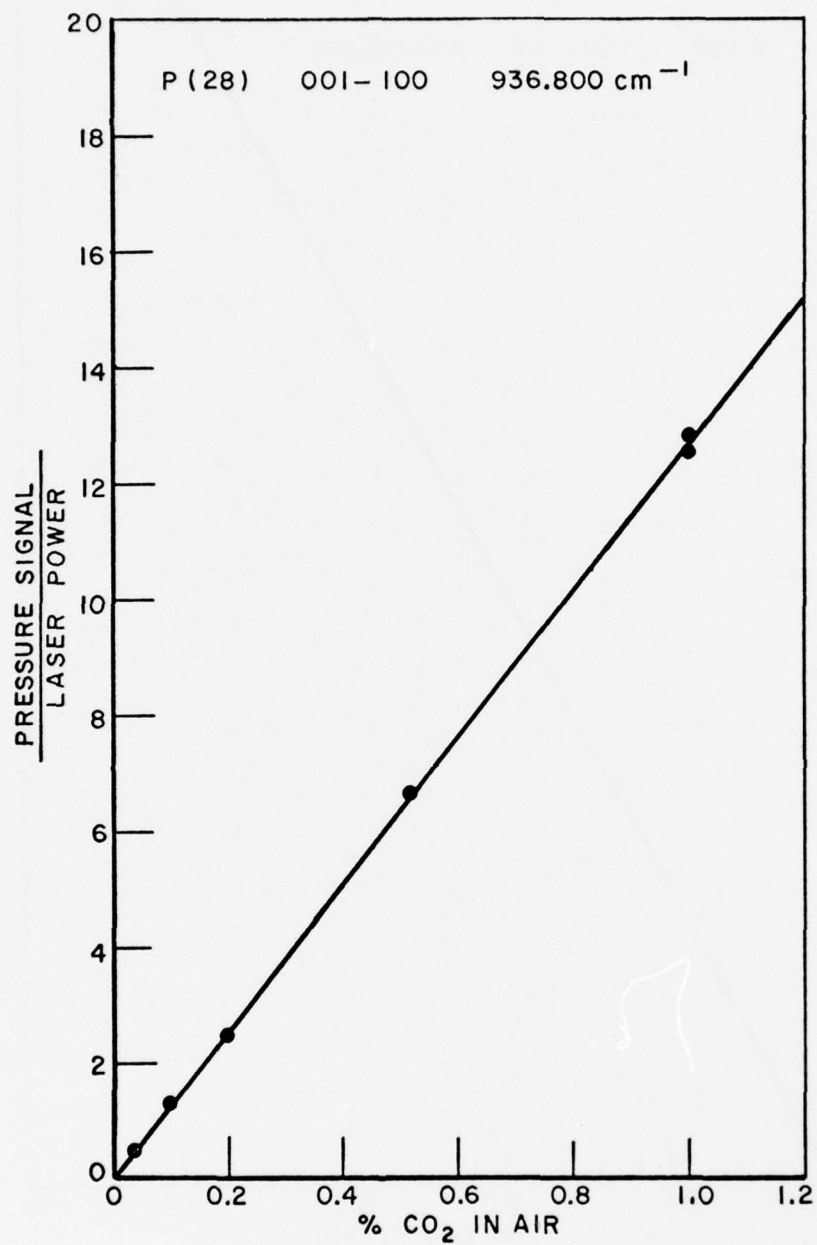


Figure 22. CO<sub>2</sub> in air.

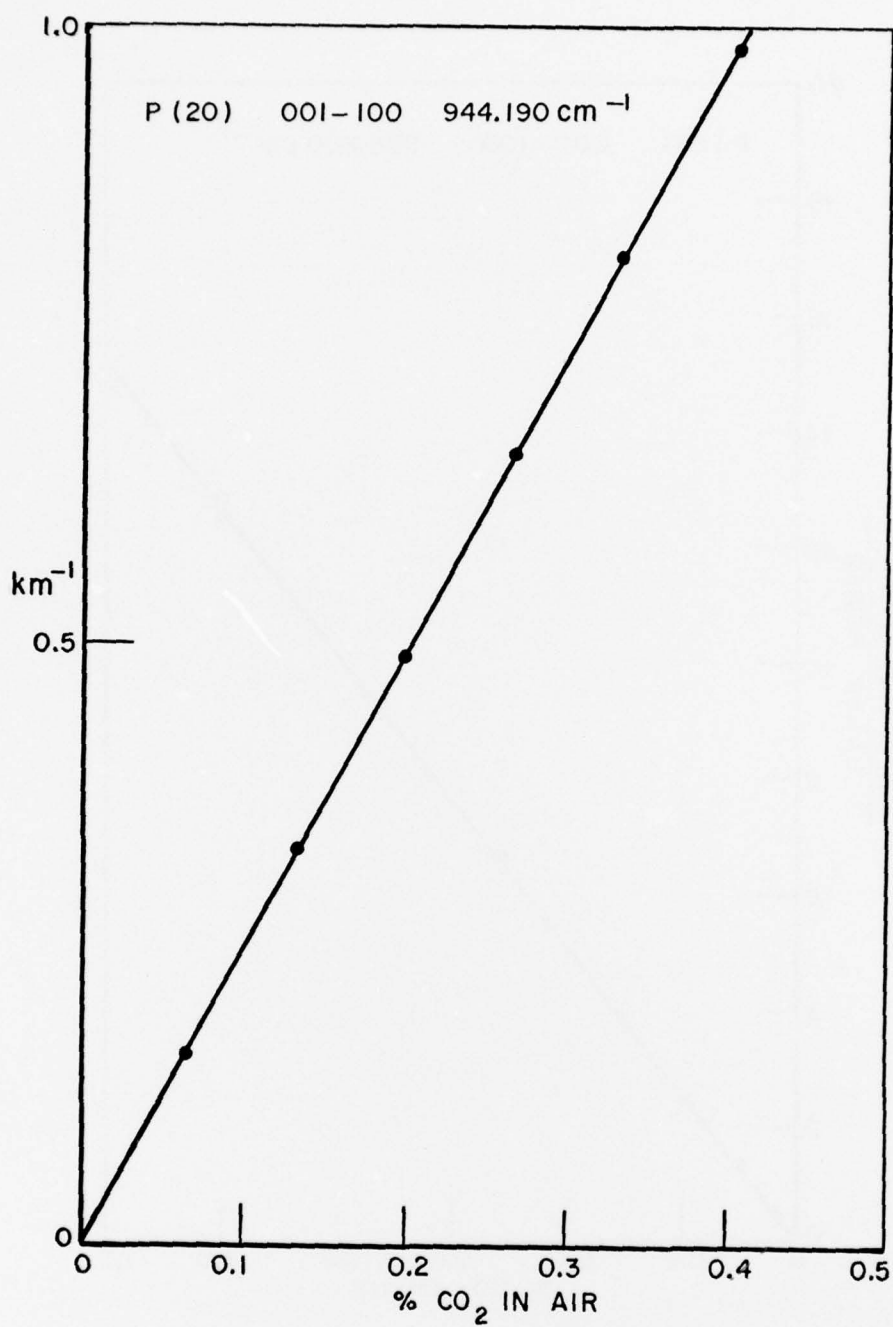


Figure 23. White cell measurement of CO<sub>2</sub> in air.

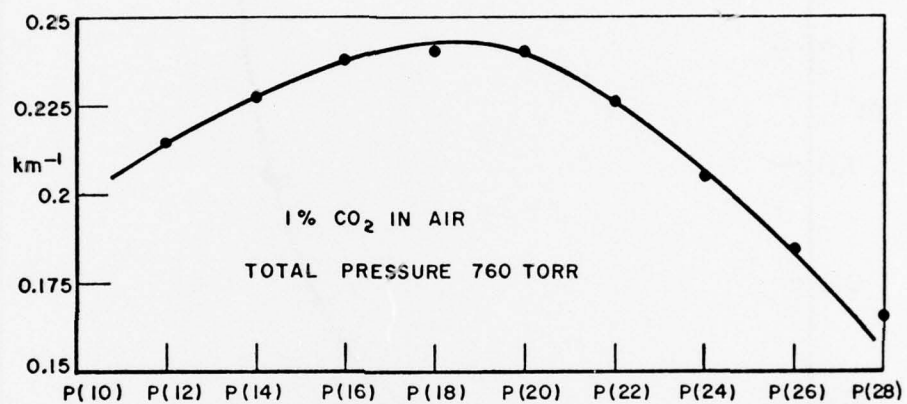


Figure 24. CO<sub>2</sub> in air absorption for nine laser lines.

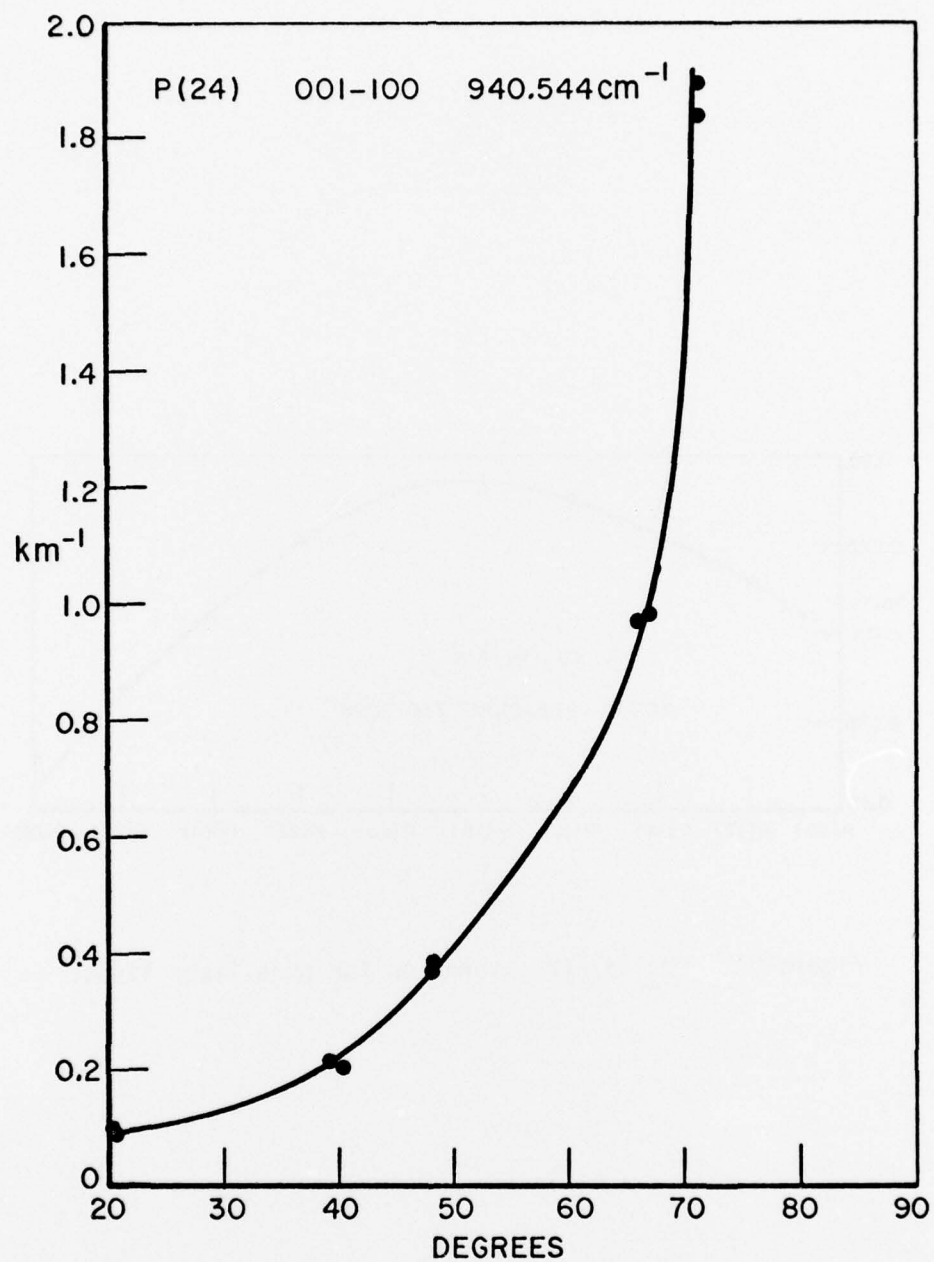


Figure 25. Pressure signal phase from CO<sub>2</sub> in air absorption measurements.

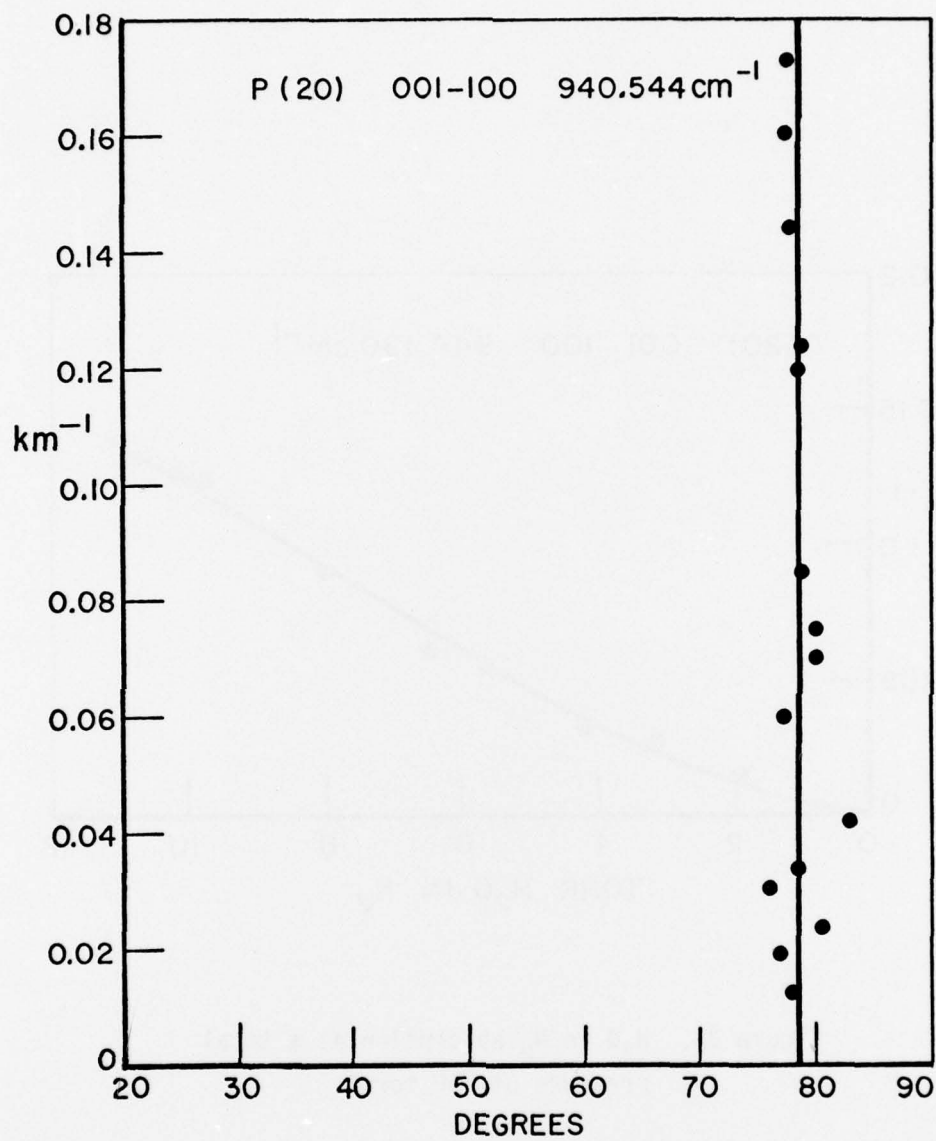


Figure 26. Pressure signal phase from H<sub>2</sub>O in N<sub>2</sub> absorption measurements.



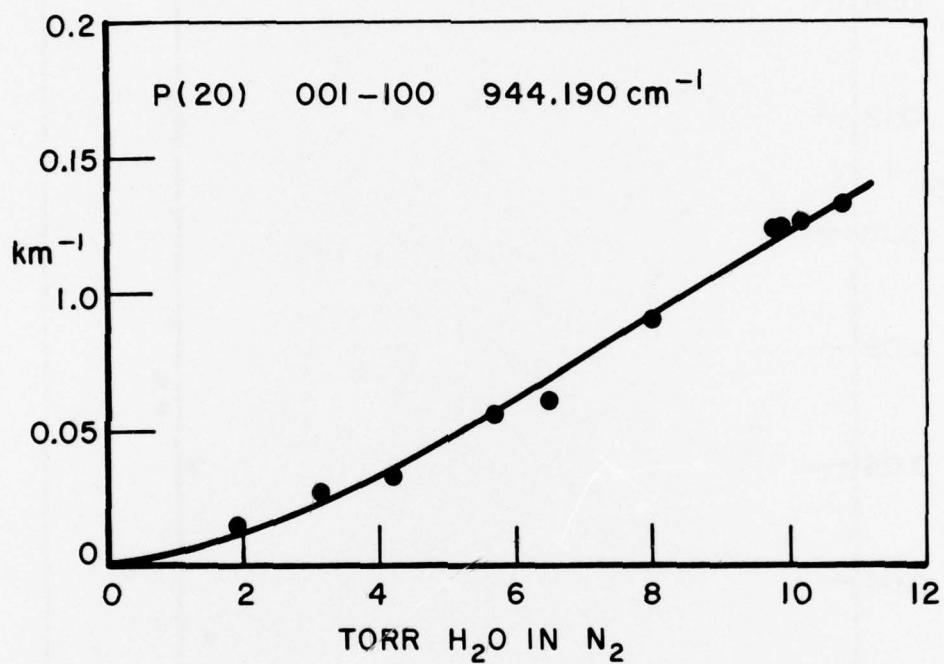


Figure 27.  $\text{H}_2\text{O}$  in  $\text{N}_2$  absorption at a total pressure of 760 torr.

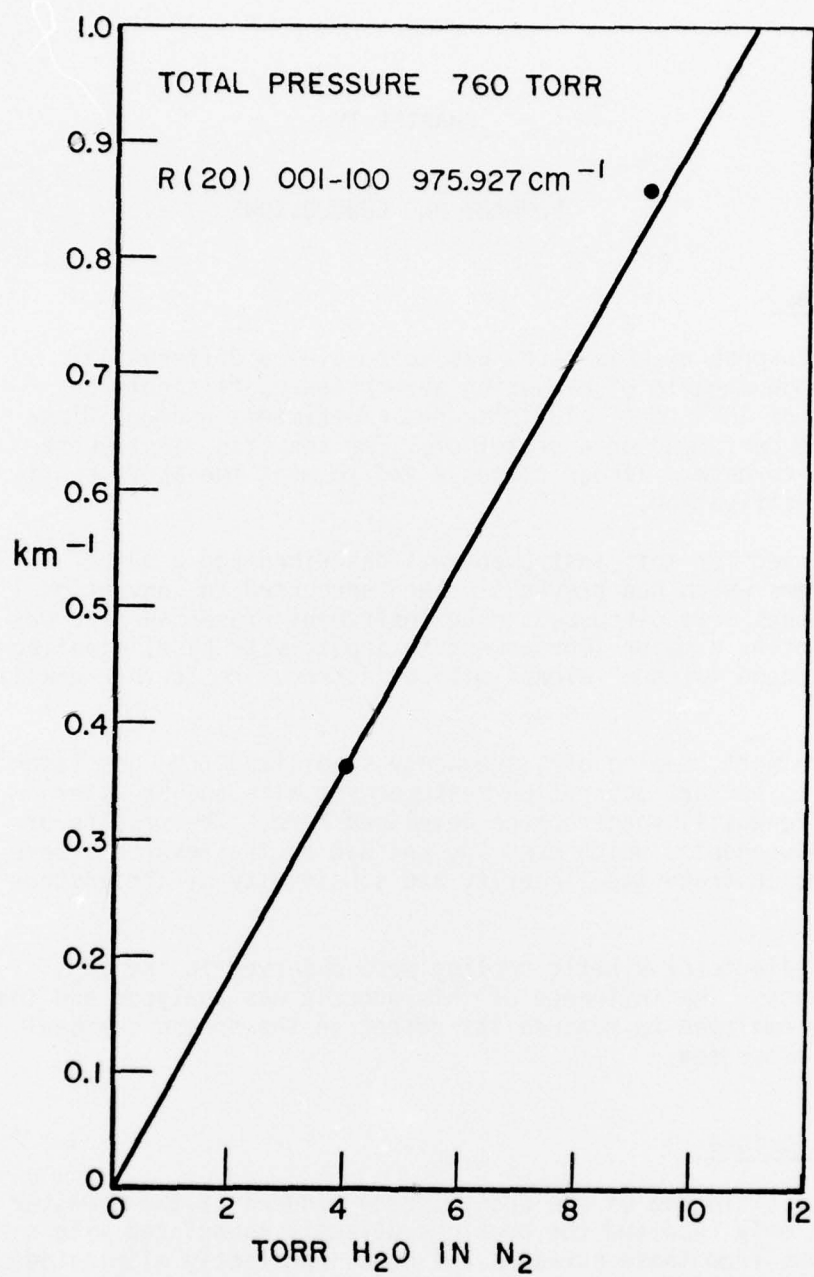


Figure 28.  $\text{H}_2\text{O}$  in  $\text{N}_2$  absorption.

## CHAPTER IV

### SUMMARY AND CONCLUSIONS

#### A. Summary

The purpose of this study was to develop a differential spectrophone capable of measuring absorption coefficients on the order of  $10^{-8} \text{ cm}^{-1}$ . To this end, experiments and modifications were performed on a prototype. The resulting instrument was shown to have a linear response and to meet the above sensitivity specification.

The need for this instrument was described and a number of the problems which had previously been encountered in conventional spectrophones were discussed. The instrument presented here was shown to offer a major improvement in sensitivity by eliminating the background "window" signal without introducing further complications.

A two watt, sealed off, frequency stabilized,  $\text{CO}_2$  gas laser was used to perform absorption measurements with the Brewster angle differential spectrophone developed here. The results of these measurements, which used  $\text{CO}_2$  and  $\text{H}_2\text{O}$  as the absorber, were used to demonstrate the linearity and sensitivity of the instrument.

The effects of kinetic cooling were observed in the  $\text{CO}_2$  measurements. The influence of this process was analyzed and the technique employed to measure its effect on the pressure signal was also presented.

#### B. Conclusions

The positioning of the spectrophone windows at the Brewster angle not only resolved the problems directly associated with reflections from these surfaces but more importantly eliminated the multiple reflections from the cell walls and therefore the pressure signal caused by the corresponding energy losses at the wall. This signal was observed to have a pronounced influence on measurements and to be critically dependent upon changes in

the optical alignment used to introduce the radiation source. Thus, the use of windows at the Brewster angle appears to be essential for obtaining repeatable results with the type of instrument described here.

The influence of system volumes on the pressure transducer response should be considered as an important factor in the instrument performance. It would seem that any efforts in the area of internal or direct calibration of a spectrophone will require a method for determining the actual magnitude of the pressure signal based on that measured with a system of finite volume. Certainly, it is important to leave the instrument volume parameters unchanged once a calibration has been obtained. The use of a leak valve across the two chambers of the differential spectrophone eliminates any need to adjust cell volume in order to equalize the static pressure across the differential capacitive manometer.

Water vapor absorption measurements were the most difficult to accurately perform. The internal contaminant problems in the present instrument appear to be sufficiently small to allow accurate measurements; however, this was initially difficult to achieve with  $H_2O$ . At the present time, efforts are continuing to determine the origin of contaminants. These efforts have recently begun to meet with success with the initial results indicating that a chemical reaction may be occurring between the  $H_2O$  and some component of the vacuum system, the product of this reaction being a contaminant gas which has the property of an absorber in the  $10 \mu$  region.

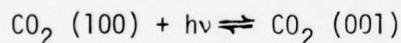


## APPENDIX A

### KINETIC COOLING

The use of a spectrophone for measuring absorption depends upon the condition that the absorbed energy is proportional to the temperature rise in the gas sample. A further consideration is the rate at which this energy transfer takes place. The case of CO<sub>2</sub> in air deserves special attention, since the absorbed energy can be initially stored in the form of internal vibration-rotation energy [12]. This process has the initial effect of cooling the gas sample and thereby inducing a time lag in the anticipated temperature rise. This phenomenon is especially important when the transient response of a spectrophone is being used to obtain absorption measurements since the pressure signal phase will be a function of the relaxation times of the involved vibration-rotation energy levels.

The processes involved in CO<sub>2</sub> absorption are the same as those occurring in the CO<sub>2</sub> laser - the only differences being direction and the proportionality constant of the transition matrix, hence



Also, the same vibration coupling of CO<sub>2</sub> (001) and N<sub>2</sub> employed in the CO<sub>2</sub> laser is active in absorption. Owing to the relative concentrations of N<sub>2</sub> versus CO<sub>2</sub> in air, nearly all the vibrational energy absorbed by the CO<sub>2</sub> (001) molecules is transferred to N<sub>2</sub>.

The depletion of the (100) state of CO<sub>2</sub> (see Figure 29) referred to above does not persist since there exists a rapid vibration-translation interaction between the ground state of CO<sub>2</sub> and CO<sub>2</sub> (100). This process is not direct but involves transitions between the degenerate bending modes of CO<sub>2</sub> and the (100) state. The net result of these transitions is a momentary depletion of the translational energy of the involved molecules, which corresponds to a cooling of the gas. This process continues for a period of time which will depend on relaxation rates of nitrogen and CO<sub>2</sub> (001) from their respective excited states to their ground



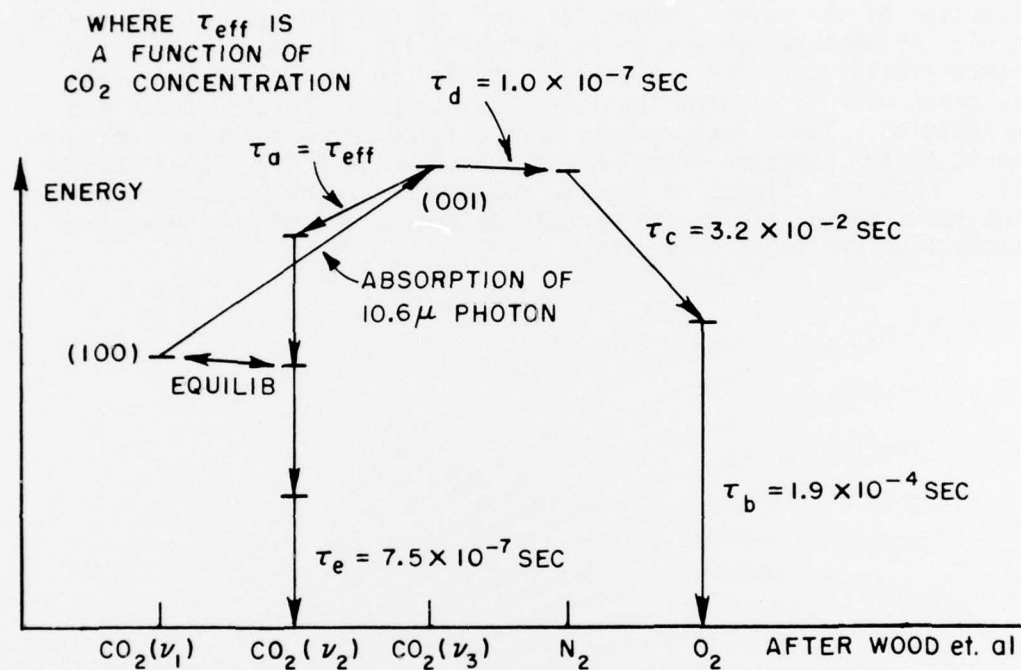


Figure 29. Relaxation rate in kinetic cooling.

states. When these transitions have occurred, the absorbed energy presents itself in the form of translational energies which then "heat" the gas.

From Figure 29 it is evident that the relaxation times  $\tau_b$ ,  $\tau_c$ , and  $\tau_a$  will be the determining rates in the transition of excited vibration states to their ground state. Wood, Camac and Gerry [12] have shown that the relaxation time  $\tau_a$  is a linear function of the relative concentrations of  $N_2$  and  $CO_2$ . Thus, the net effect of kinetic cooling is to cause an initial decrease in temperature and delay the impending temperature rise for a time duration that is a function of the relative concentrations of  $CO_2$  and air. In Figure 30 a plot of measured values of  $\tau_a$  (actually  $1/\tau_a$  is shown) versus  $CO_2$  concentration (the concentration of  $N_2$  can be considered constant) is given which indicates the linear relationship between these two quantities. These measurements were obtained from the phase measurements of the pressure signal which are shown in Figure 25 of Chapter IV. Thus, the effects of kinetic cooling are readily observed with the spectrophone and can be used to determine one of the relaxation times involved in this process.

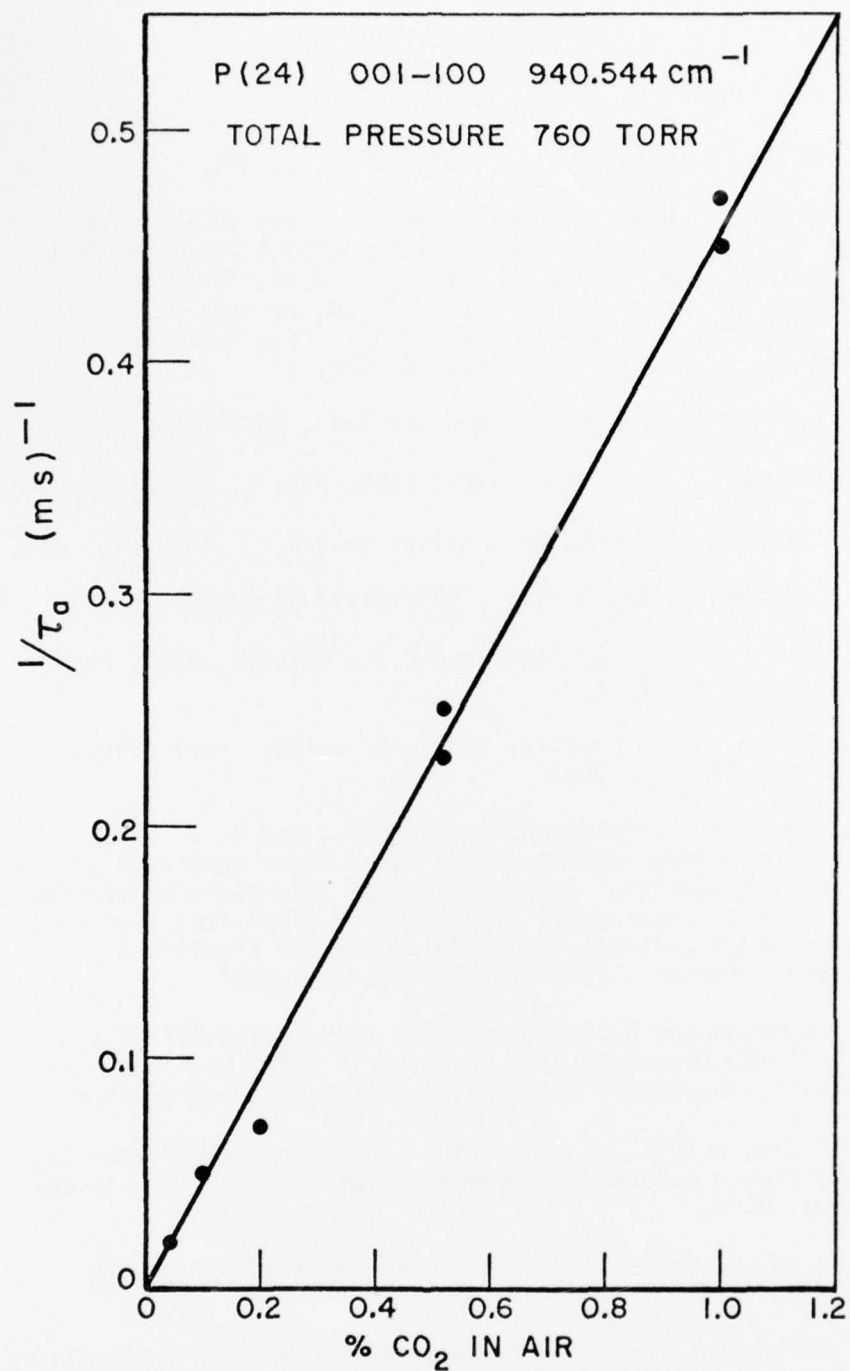


Figure 30. Effective relaxation time for CO<sub>2</sub> absorption.

# REFERENCES

- [1] J. U. White, J. Opt. Soc. Am., 32 (1942), p. 285.
- [2] G. L. Trusty, "Absorption Measurements of the 10.4 Micron Region Using a CO<sub>2</sub> Laser and a Spectrophone," Report 2819-4, January 1973, The Ohio State University ElectroScience Laboratory, Department of Electrical Engineering; prepared under Contract F33615-69-C-1807 for Air Force Avionics Laboratory. (AFAL-TR-72-413)(AD 907 549)
- [3] A. G. Bell, Proc. Am. Assoc. Advance Sci., 29 (1880), p. 115.
- [4] M. L. Viengerov, Izv. Akad. Nauk, USSR, Fiz. 4, (1940), p. 94.
- [5] E. L. Kerr and J. G. Atwood, Applied Optics, 7 (1968), p. 915.
- [6] L. B. Kreuzer, J. Appl. Phys., 42 (1971), p. 2934.
- [7] C. F. Dewey, Jr., R. D. Kamm, and C. E. Hackett, Appl. Phys. Lett., 23 (1973), p. 633.
- [8] T. F. Deaton, D. A. Depatie, and T. W. Walker, Appl. Phys. Lett., 26 (1975), p. 300.
- [9] E. K. Damon, J. C. Peterson, F. S. Mills, and R. K. Long, "Spectrophone Measurements of the Water Vapor Continuum at DF Laser Frequencies," August 1975, The Ohio State University ElectroScience Laboratory, Department of Electrical Engineering; prepared under Contract F30602-75-C-0029 for the Rome Air Development Center. (RADC-TR-75-203), (A016435).
- [10] W. H. Thomason and D. C. Elbers, "An Inexpensive Method to Stabilize the Frequency of a CO<sub>2</sub> Laser," 1974, Louisiana State University, Department of Chemistry, private communication.
- [11] F. S. Mills, private communication, The Ohio State University ElectroScience Laboratory, Department of Electrical Engineering, Columbus, Ohio.
- [12] A. D. Wood, M. Camac, and E. T. Gerry, Applied Optics, 10 (1971), p. 1877.
- [13] F. S. Mills, private communication, The Ohio State University ElectroScience Laboratory, Department of Electrical Engineering, Columbus, Ohio.
- [14] F. S. Mills, private communication, The Ohio State University ElectroScience Laboratory, Department of Electrical Engineering, Columbus, Ohio.



*MISSION  
of  
Rome Air Development Center*

*RADC plans and conducts research, exploratory and advanced development programs in command, control, and communications (C<sup>3</sup>) activities, and in the C<sup>3</sup> areas of information sciences and intelligence. The principal technical mission areas are communications, electromagnetic guidance and control, surveillance of ground and aerospace objects, intelligence data collection and handling, information system technology, ionospheric propagation, solid state sciences, microwave physics and electronic reliability, maintainability and compatibility.*

